The Dissertation Committee for Shida Shen certifies that this is the approved version of the following Dissertation:

Transport Studies of Transition-Metal-Oxide Antiferromagnets from a Perspective of Applications in Memory Technology

Committee:

Maxim Tsoi, Supervisor

Jianshi Zhou

Keji Lai

Xiaoqin Li

Gregory Fiete

Transport Studies on Transition-Metal-Oxide Antiferromagnets from a Perspective of Applications in Memory Technology

by

Shida Shen

Dissertation

Presented to the Faculty of the Graduate School of

The University of Texas at Austin

in Partial Fulfillment

of the Requirements

for the Degree of

Doctor of Philosophy

The University of Texas at Austin

May 2019

Dedication

To my family

Acknowledgements

First, I want to thank my supervisor, Prof. Maxim Tsoi, for all his guidance and help during my Ph.D. study. I constantly benefit from his rich knowledge in physics, strict attitude towards academia research, as well as his nice personality.

I want to thank our collaborators, Prof. Jianshi Zhou from Department of Engineering at University of Texas at Austin and Prof. Gang Cao from Department of Physics at University of Colorado Boulder. They provided many wonderful samples for our experiments as well as valuable comments and suggestions about our research. Prof. Zhou also serves on my dissertation committee. I also want to thank other members of my committee: Prof. Keji Lai, Prof. Xiaoqin Li, and Prof. Gregory Fiete.

I want to thank our Department of Physics at the University of Texas at Austin, including all the professors I have met here, for the academic training and physics knowledge I received during my five-year graduate study.

I want to thank my parents, and other family members, for their support. My parents set great life examples for me and encourage me to pursue my goals.

All my friends, here and back home, have made my life more interesting during these years. I want to thank all of them.

Abstract

Transport Studies of Transition-Metal-Oxide Antiferromagnets from a Perspective of Applications in Memory Technology

Shida Shen, Ph.D.

The University of Texas at Austin, 2019

Supervisor: Maxim Tsoi

Antiferromagnetic spintronics offers a promise of more robust, stray-field-free and ultra-high-speed applications, e.g. in memory technology. Transition metal oxides (TMOs) represent a big and natural pool of antiferromagnetic materials. This thesis presents a series of transport studies with TMO antiferromagnets, i.e., Sr_2IrO_4, Ca_2RuO_4, and La_2NiO_4. We are focused on both TMO single crystals and heterostructures. For instance, we examined magnetoresistance and microwave response of a Pt/Sr_2IrO_4 double-layer structure in order to explore the spin Hall effect (SHE) enabled by the heavy-metal Pt overlayer. We have shown that the SHE-mediated spin injection from Pt into Sr_2IrO_4 can affect the magnetoresistance of Sr_2IrO_4. In a series of experiments with Ca_2RuO_4 we demonstrated that single crystals of this TMO, when doped with Cr, exhibit a non-destructive reversible resistive switching at room temperature. An applied electrical bias was shown to reduce the dc resistance of Ca_2RuO_4 crystals by as much as 75%; the original resistance of the sample could be restored by applying an electrical bias of opposite polarity. Our results of transport measurements in 2-, 3-, and 4-probe geometries suggest that the resistive switching is mostly an interfacial effect. Temperature-dependent

resistivity measurements on Ca_2RuO_4 show that the activation energy of this material can be tuned by an applied dc electrical bias. A similar non-destructive, bipolar and room-temperature resistive switching is also observed in La_2NiO_4 single crystals. It is also identified by 2-, 3- and 4-porbe measurements that the switching in La_2NiO_4 happens essentially at the sample/contact probe interfaces. The wide range of observed resistance values from 10 to 80 kΩ confirmed the tunneling nature of the La_2NiO_4 contacts. We tentatively associate the resistive switching in our TMOs with electric-field induced distortions of TMO lattice and have made an attempt to probe such distortions directly in experiments with a capacitive displacement meter. The resistive switching in Ca_2RuO_4 and La_2NiO_4 may be useful for non-volatile memory devices in the future. Finally, we have performed a comparative study between recycled and virgin NdFeB magnets. The recycled magnets demonstrate an enhancement of resistivity compared to the virgin ones, but share a similar surface morphology, magnetic structure, and magnetotransport properties.

Table of Contents

List of Figures

INTRODUCTION

Transition Metal Oxides (TMOs) constitute an interesting class of condensed matter systems. Many intriguing phenomena can happen in TMOs, ranging from metal-insulator transition to high-temperature superconductivity and more [1, 2]. The complex electronic and magnetic properties of TMOs offer a fruitful source for finding new physics, since they ignite innovations in theories as well as advancements in experimental techniques. On the other hand, due to their complexity and versatility, TMOs provide great possibilities for future information processing and storage devices. For example, metal-insulator transition in TMOs may play a role in resistive-switching-based non-volatile memories. Recently, antiferromagnetic (AFM) spintronics [3, 4] emerged and attracted a considerable research attention, as AFM spintronics may add robustness and other advantages to spintronic applications as well as enable a higher computational speed. Many TMOs are antiferromagnets and AFM TMOs have shown their potential in spintronic applications.

Transport studies on TMOs offer experimental evidences that are fundamental to the understanding of physics behind the phenomena in TMOs and give guidance to the design of future applications based on these materials. This dissertation presents a series of transport studies on TMOs and its structure is based on a number of distinguished TMO materials. For instance, Chapter 1 presents study of transport and magnetic properties of Sr_2IrO_4 and is focused on the effects of spin injection into TMOs via the spin Hall effect in an adjacent Pt layer. Chapter 2 presents a study of single crystals of Cr doped Ca_2RuO_4 and demonstrates that its transport properties can be tuned by an applied electrical bias and

includes a resistive switching phenomenon at room temperature. Chapter 3 presents a study of tunneling-type contacts on La_2NiO_4, which reveal a reversible resistive switching with potential applications in memory technology.

Besides TMOs, Chapter 4 presents a comparative study of virgin and recycled NdFeB magnets. Transport properties of these materials were investigated on both macroscopic and microscopic scales. Such NdFeB alloys are widely used nowadays and the recycled materials have gained significant importance from both economic and environmental points of view.

Before moving forward, in what follows I will also introduce background information about two areas of emerging technologies: resistive memory technology and antiferromagnetic spintronics.

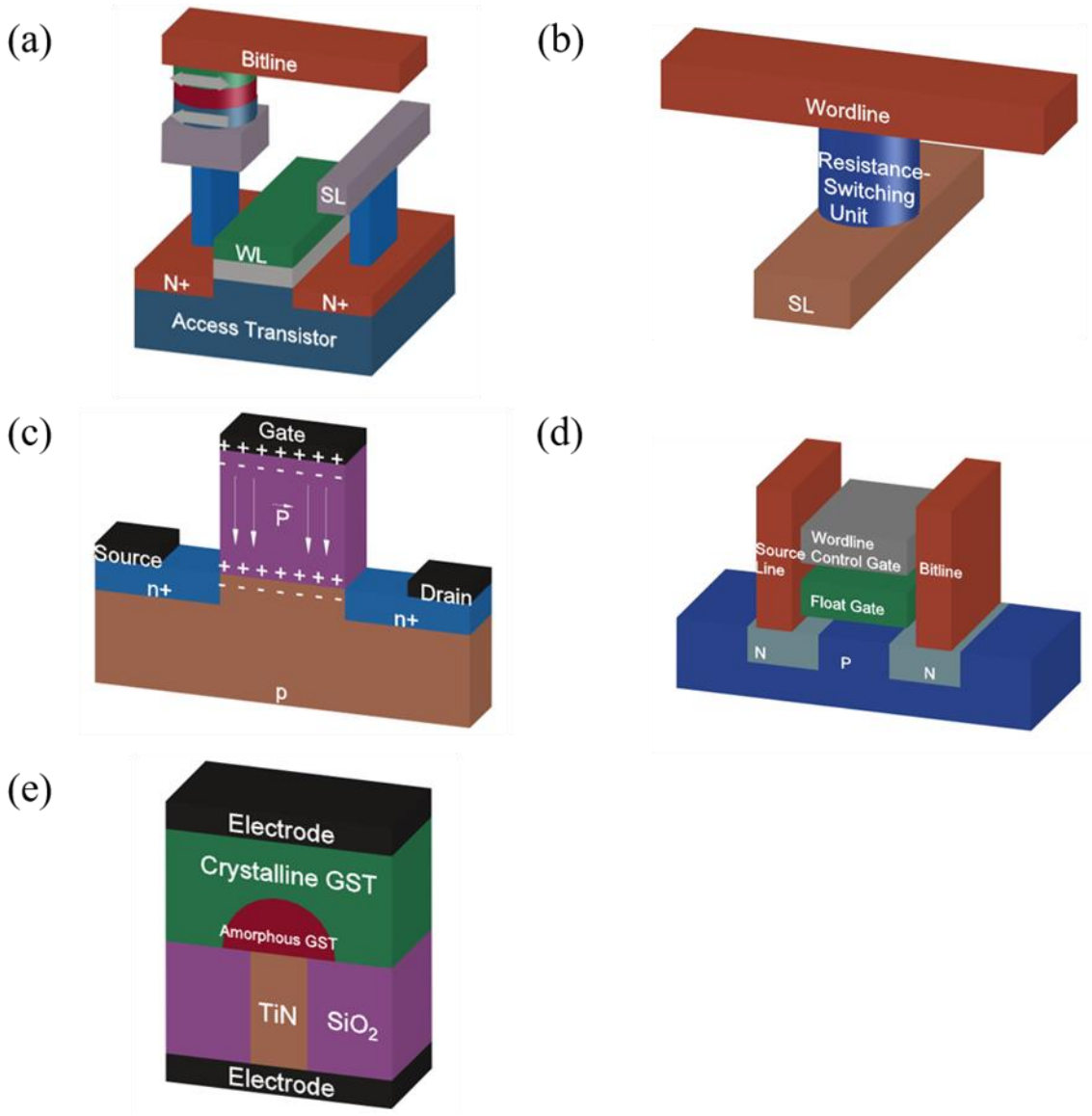

Fig. 1.1. Illustrations of different non-volatile memories: (a) STT-RAM (b) Resistive RAM (c) Ferroelectric RAM based on ferroelectric effects (d) NAND-flash RAM (e) Phase-change RAM, one type of Resistive RAM, often listed as a type alone

Memories are key components in modern computer architecture. Most of the memories used nowadays are volatile, which means data is eventually lost after power is turned off, whether they are static random-access-memory (SRAM) used in CPU cache or dynamic random-access-memory (DRAM) used as main memory. In comparison, non-volatile memories retain data after power is off. Non-volatile memories usually operate based on physical states rather than transistors and capacitors, e.g. they use different physical states to record information and switch between these states to write information. Different mechanisms have been proposed and experimented for non-volatile memories, as shown in Fig. 1.1. Here we focus on resistive RAM [1, 5], where resistive switching in TMOs may play a role and magnetic RAM, which is an example of spintronics applications. Most advanced magnetic RAM, STT-RAM, has already been commercially available.

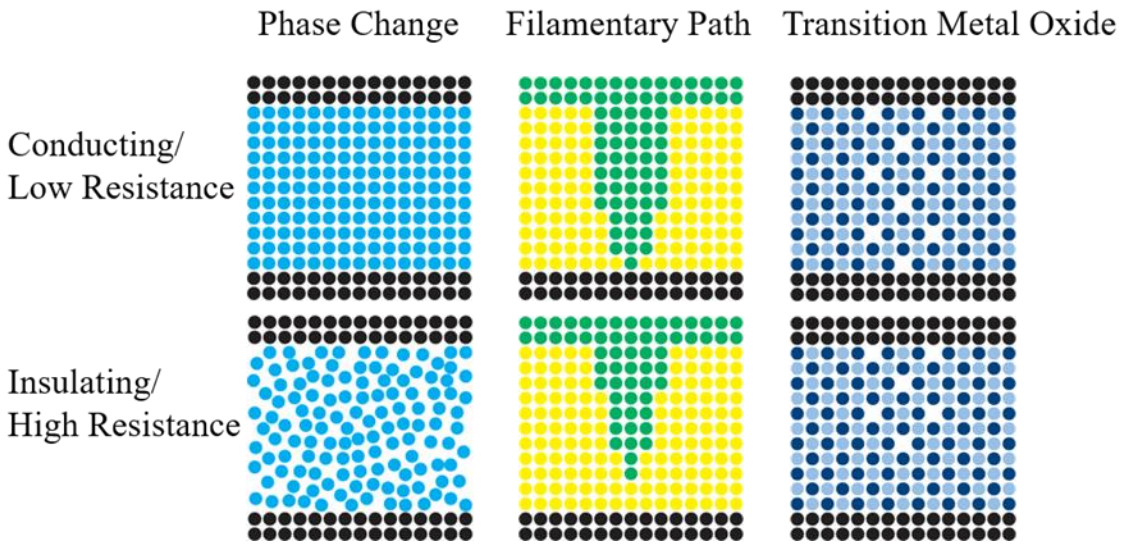

Fig. 1.2. Illustrations of different mechanisms for resistive RAM.

In resistive RAM (re-RAM), information is encoded into high and low resistance states. For example, high resistance state can be used as ‘1’ and low state as ‘0’. Under a strong bias, the memory cell switches from high state to low state or low to high. A small bias or current is used to read out the resistance state. These are the ‘writing’ and ‘reading’ operations of re-RAM. The idea sounds simple but is difficult in implementation. To build such resistive-switching units, people have come up with different mechanisms [1, 5]. Three major types of re-RAM mechanisms are (i) phase-change-material type (ii) filamentary-path type (iii) transition-metal-oxides type, as illustrated in Fig. 1.2. In phase-change re-RAM, chalcogenide material switches between ordered, low-resistance crystalline state and disordered, high-resistance amorphous state. In filamentary-path type re-RAM, resistive switching units are based on electrolyte glass where the movement of metal ions form and destroy conductive paths, resulting in low and high resistance states respectively. TMO-type re-RAM is more complicated and calls for more theoretical studies. The movements of oxygen vacancies may explain the switching between high and low resistance states; but it is also true that metal-insulator transition (MIT) is widely seen in TMOs and MIT can be triggered by different physical processes. Mott transition in TMOs, or structural changes may induce MIT which results in resistive switching, as would be discussed in Chapter 2 and Chapter 3.

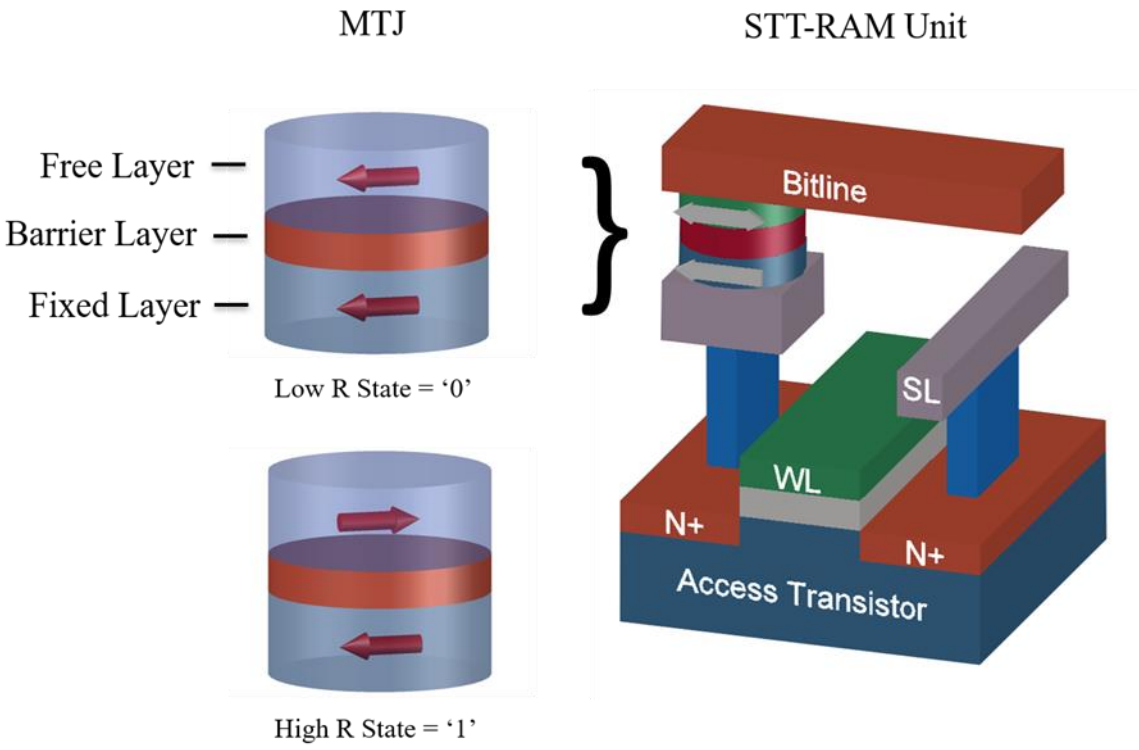

Fig. 1.3. Illustrations of magnetic tunnel junction and STT-RAM unit.

Magnetic RAMs (MRAMs) make use of magnetic states and are based on magnetic tunneling junctions (MTJs). MTJs are sandwich structures with three layers: one free layer which has magnetic moments switchable by external magnetic fields or spin torques, one barrier layer which acts as a tunneling barrier and one fixed layer with magnetic moments pinned in one direction. It turns out, quantum-mechanically, electrons in free layer would be more likely to tunnel through barrier if free layer's magnetic moments are aligned parallel to fixed layer, resulting in a low resistance state; conversely, if magnetically the free layer is aligned anti-parallel to the fixed layer, electrons would be less likely to tunnel

through barrier, resulting in a high resistance state. STT-RAM is the state-of-art MRAM (STT short for spin-transfer-torque). It utilizes spin-polarized currents instead of external magnetic fields to flip the free layer. In STT-RAM, spin-polarized currents are generated by passing currents through a thick ferromagnetic layer and they exert torques on the free layer to realize magnetic-moments-flipping.

MRAM demonstrates the feasibility and potential of spintronics based on ferromagnetic materials. The arise of antiferromagnetic spintronics comes with its great comparative advantages. Antiferromagnetic systems have magnetic moments alternating at neighboring sites. Sometimes these moments are also canted. This kind of arrangement results in a net moment almost or close to zero and it is difficult to influence internal moments with outside fields. Antiferromagnetic systems become 'invisible' to outside fields and the internal magnetic fields are also limited inside the systems. So antiferromagnetic spintronics devices are more robust to outside perturbations and are stray-field-free, i.e. there are no cross-talk between devices. Most importantly, antiferromagnetic systems have resonant frequencies in THz, much higher than ferromagnetic resonant frequencies in GHz. Antiferromagnetic spintronics applications may be capable of ultra-fast computation in the future.

Antiferromagnetic spintronics also aim at new information technologies beyond information storage. As an exciting picture, if in the future information flow is carried by spin flows in antiferromagnetic devices, e.g. via magnons or skirmions, there comes the need to detect spin flows or effective fields generated by them. Anisotropic magnetoresistance (AMR) of AFM materials is ideal for this task. For example, previous study has applied nano-scale point contacts and revealed AMR in perovskite Sr_2IrO_4 at liquid nitrogen temperature [6].

As semiconductors, AFM TMOs also have electronic properties that may be integrated to silicon-based circuits and connect spintronics with electronics. In Sr_2IrO_4 and its sister iridate $Sr_3Ir_2O_7$, studies have found electronic transport tunable by electric fields [7, 8]. Resistive switching was also found in $Sr_3Ir_2O_7$. This resistive switching was shown to be suppressed by microwave signals, which offer insights for future studies in high-frequency dynamics of AFM devices.

The series of TMOs studied in Chapter 1 (Sr_2IrO_4), Chapter 2 (Ca_2RuO_4) and Chapter 3 (La_2NiO_4) are antiferromagnets with different transport and magnetic properties. Hopefully the work presented in this dissertation would enrich our knowledge about these materials and provide references for future AFM spintronics studies.

Reference

[1] Sawa, A. Resistive switching in transisiton metal oxides. Mater. Today 11, 28–36 (2008).

[2] Lee, P. A., Nagaosa, N. & Wen, X.-G. Doping a Mott insulator: Physics of high-temperature superconductivity. Rev. Mod. Phys. 78, 17–85 (2006).

[3] Baltz, V. et al. Antiferromagnetic spintronics. Rev. Mod. Phys. 90, 15005 (2018).

[4] Jungwirth, T., Marti, X., Wadley, P. & Wunderlich, J. Antiferromagnetic spintronics. Nat. Nanotechnol. 11, 231 (2016).

[5] Meijer, G. I. Who Wins the Nonvolatile Memory Race? Science (80-.). 319, 1625 LP-1626 (2008).

[6] Wang, C. et al. Anisotropic magnetoresistance in antiferromagnetic Sr2IrO4. Phys. Rev. X 4, (2014).

[7] Wang, C. et al. Electrically tunable transport in the antiferromagnetic Mott insulator Sr2IrO4. Phys. Rev. B 92, 115136 (2015).

[8] Seinige, H. et al. Electrically tunable transport and high-frequency dynamics in antiferromagnetic Sr3Ir2O7. Phys. Rev. B 94, 214434 (2016).

CHAPTER 1

SPIN HALL EFFECT AND MAGNETORESISTANCE OF PT/Sr_2IrO_4 DOUBLE LAYER HETEROSTRUCTURE

This chapter presents a transport study of Pt/Sr_2IrO_4 double-layer heterostructure. We examined the effects of spin injection on the anisotropic magnetoresistance of Sr_2IrO_4 and its response to microwaves in a search for ferromagnetic/antiferromagnetic resonance. The spin injection was enabled by the spin Hall effect in the adjacent Pt layer. We have studied the magnetoresistance as a function of temperature, magnitude of the applied dc bias, microwave frequency and power. There was no evidence of ferromagnetic or antiferromagnetic resonance found in these experiments, however, the sample magnetoresistance was found to be different with and without the spin injection from Pt; a larger variation in resistance vs magnetic field was observed when the dc current was applied on the Pt side. At liquid nitrogen temperature, the sample exhibited a unipolar resistive switching. The critical current for the switching was found to vary as a function of the applied microwaves and/or low-frequency ac current.

1.1 INTRODUCTION

1.1.1 Antiferromagnetic Iridate: Sr_2IrO_4

5d transition metal oxide Sr_2IrO_4 has been extensively studied [1]. Sr_2IrO_4 lattice forms a canted antiferromagnet [2], with Néel temperature ~ 240K [3]. Due to a combination of strong spin-orbit coupling and on-site Coulomb repulsion, the $5d^5$ (t_{2g}) band is split, resulting in a Mott-type insulator gap [4].

As illustrated in Fig. 2.1, the IrO_6 octahedra rotate about c-axis by ~11 degree [5, 6]. This rotation distorts Ir-O-Ir bond and gives rise to many novel electronic and magnetic properties in Sr_2IrO_4. Lattice distortions induced by high pressure [7], epitaxial strain [8] and magnetic fields [9] was found to change the effective energy gap at liquid nitrogen temperature. More recently, with nanoscale point contact spectroscopy, electrically tunable transport was found in Sr_2IrO_4 [10]. This tunable transport may be associated with a field-driven displacement of oxygen anions in Ir-O-Ir bonds and the bias-dependent resistance can be fitted by a field effect model:

$$R(X) = A * e^{\frac{\Delta(I)}{2k_BT}}, \quad \Delta(I) = \Delta_0 - B * |I|$$

This tunable transport in Sr_2IrO_4 crystals may fit into a broader picture of pursuing more flexible electronic devices in the future, as conventional semiconductors have band structures fixed by crystal structure and chemical composition.

Point-contact measurements have also found (in Sr_2IrO_4) a large magnetoresistance (MR) of ~28% under modest magnetic field of 250 mT at liquid nitrogen temperature [11]. Angular-dependent measurements revealed anisotropic MR with transition from 4-fold symmetry at low magnetic fields to 2-fold symmetry at high fields. It was proposed that such an anisotropic MR may be suitable for monitoring the magnetic state in future AFM spintronic devices.

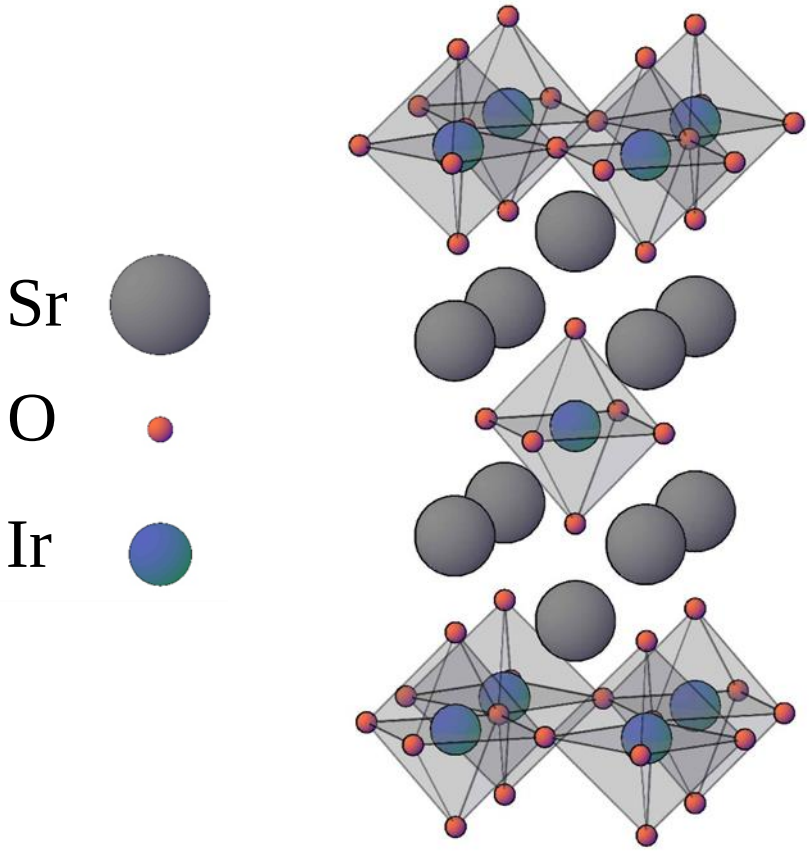

Fig. 2.1 (a) Lattice model of Sr_2IrO_4. Ruddlesden–Popper iridates (layered perovskites) $Sr_{n+1}Ir_nO_{3n+1}$ with n = 1. IrO_6 octahedra are rotated ~11 degree.

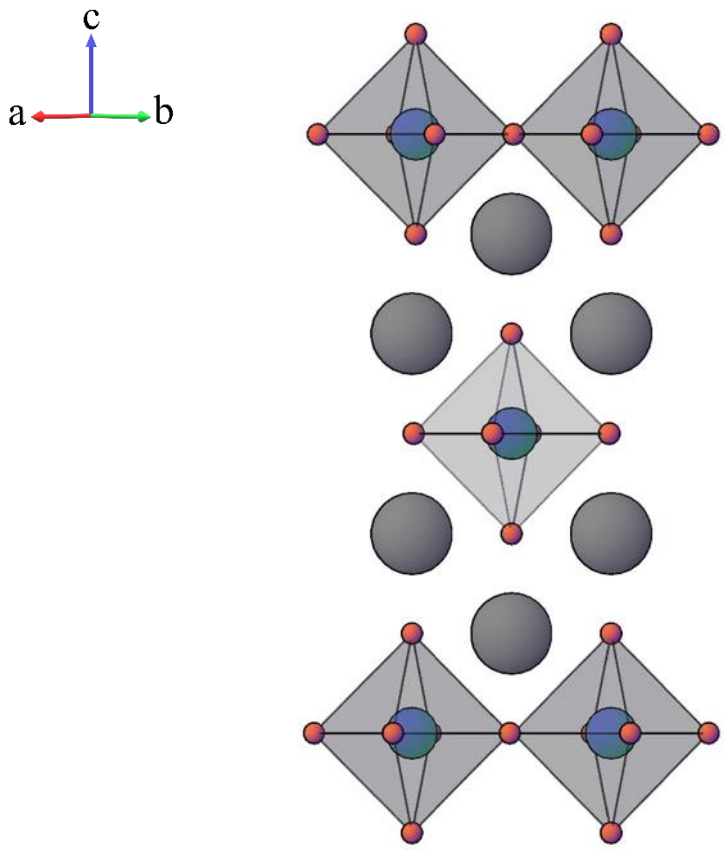

Fig. 2.1 (b) Front view of Sr_2IrO_4 lattice

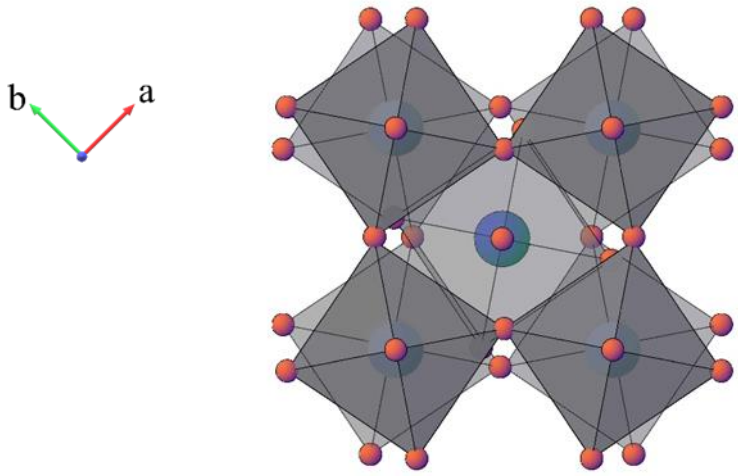

Fig. 2.1 (c) Top-view (a-b plane) of Sr_2IrO_4 lattice.

1.1.2 Current-Driven Magnetization Switching and Excitation by Spin Hall Effect

Spin Hall effect has been used to induce magnetic resonance [12] and realize magnetic switching [13] in solid state devices. A successful application of Spin Hall effect in nanoscale magnetic devices can be more energy-efficient than directly applying magnetic fields, and easier to scale than generating spin-polarized current by thick ferromagnetic layers, like in magnetic tunnel junctions (MTJs). These make spin Hall effect attractive for future spintronics applications.

Spin Hall effect was introduced in 1999 [14]; previously people have already predicted such phenomenon but did not use the term [15]. In Hall effect, Lorentz force will deflect carriers and result in imbalanced charge accumulation across the direction of currents; while in spin Hall effect, it is the net spin rather than charge that gets imbalanced across the direction of currents. Spin Hall effect can occur through two mechanisms. First is through Mott scattering where electrons with different spins are scattered into opposite directions by impurities [14]. The scattering process involves spin-orbit coupling of electrons. Second spin Hall mechanism involves a spin-orbit-coupled band structure [18], where electrons trajectories depend on spins. This mechanism is called intrinsic spin Hall effect. Spin Hall angle, defined as spin current divided by normal current ($\boldsymbol{J_{spin}}$ / $\boldsymbol{J_e}$), measures the efficiency of converting normal current into spin current for heavy metals. Common heavy metals with large spin Hall angles include platinum [17] and β-tungsten [18].

Here our interest lies in potential ferro/antiferromagnetic excitations in iridate Sr_2IrO_4. In [19], both ferromagnetic and antiferromagnetic resonances signals are found by electron spin resonance spectroscopy. This chapter tries to investigate magnetic resonance in a transport perspective and tries to see if spin Hall effect can be used to generate ferromagnetic/antiferromagnetic resonance in antiferromagnetic Sr_2IrO_4.

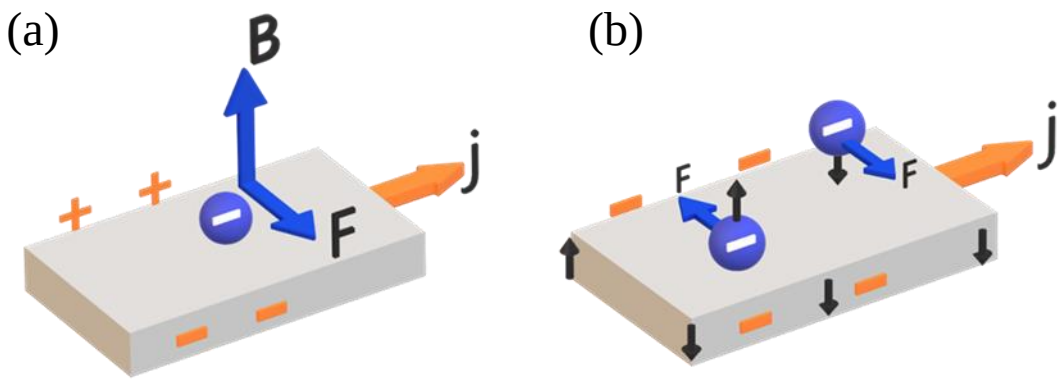

Fig. 2.2 (a) Hall effect (b) spin Hall effect. In normal Hall effect, carriers sense Lorentz force and their trajectories get deflected, resulting in a charge imbalance across the direction of current. While in spin Hall effect, electrons with opposite spins are deflected in opposite directions, result in a spin imbalance across the direction of current with charge still being balanced.

1.1.3 Experimental

In our experiment, we used a single crystal of Sr_2IrO_4 synthesized via a self-flux technique [20]. Then a 15-nm-thick layer of platinum (Pt) was deposited on the top surface of Sr_2IrO_4 crystal by electron beam evaporation. The Pt/Sr_2IrO_4 double layer structure was put on top of a microwave connector, with the Pt layer bridging the gap between the inner and outer electrodes of the connector, as shown in Fig. 2.3 (b). The microwave-connector electrodes on Pt side of the double-layer sample are used to drive dc and microwave currents through the sample. Two extra (silver-epoxy) contacts were made on the other side (on Sr_2IrO_4 side) to drive dc currents into the Sr_2IrO_4 crystal directly.

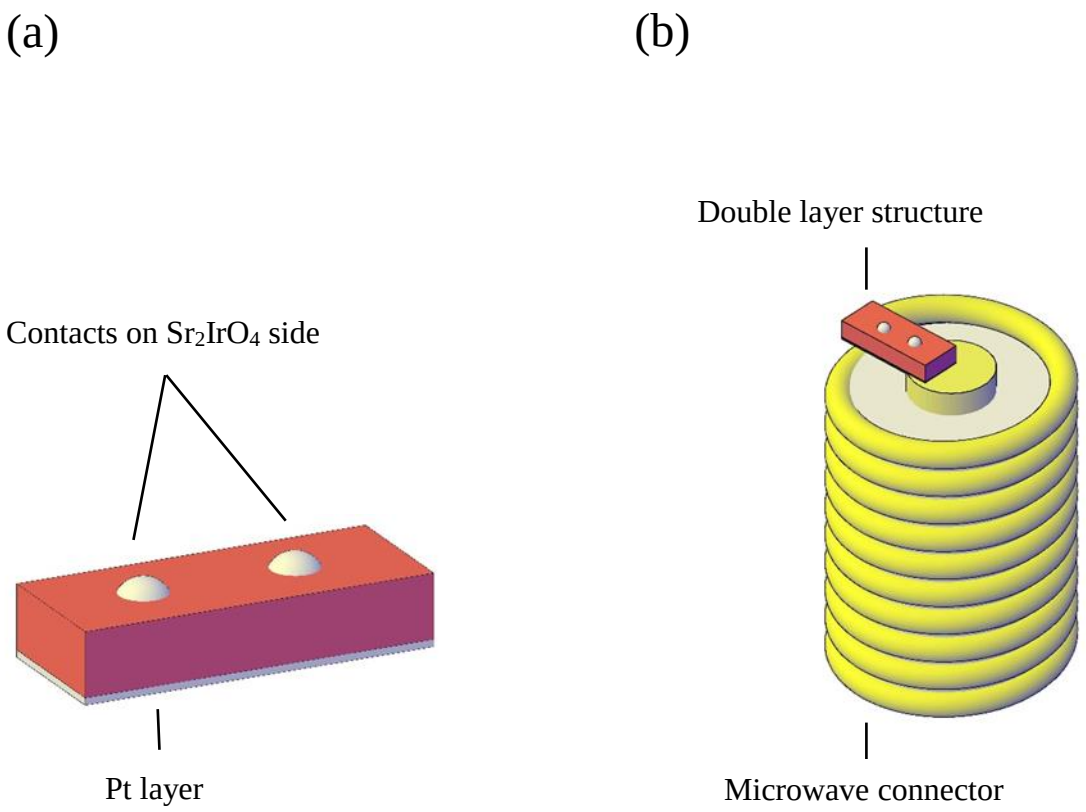

Fig. 2.3 (a) Sample preparation: Pt layer was deposited on top of single crystal of Sr_2IrO_4, 2 more conductive contacts (silver pastes) were built on the other side for driving current on Sr_2IrO_4 side. (b) Connection: double layer structure was put on top of microwave connector bridging the inner and outer side of connector.

1.2 STUDYING EFFECTS OF MICROWAVES

The next two subsections present data and results from the transport study conducted on the Pt/Sr_2IrO_4 double-layer structure. This subsection investigates the influence of microwaves on the Pt/Sr_2IrO_4 double-layer structure. Here both dc and microwave currents are driven using only the contacts on the Pt side of the structure. The next subsection focuses on comparison between transport measurements on Pt and on Sr_2IrO_4 sides. In the next subsection, dc currents, microwaves and low frequency ac currents are driven through the structure using contacts on both sides.

1.2.1 Magnetoresistance at Liquid Nitrogen Temperature

Fig. 2.4 displays the sample resistance versus external magnetic field at liquid nitrogen temperature ~77K. Magnetoresistance (MR) in the Pt/Sr_2IrO_4 double-layer structure is similar to that observed in Sr_2IrO_4 single crystals [11], e.g. the shape of R vs. B curves are similar; however, the MR ratio ($\Delta R/R$) in Pt/Sr_2IrO_4 is only about 0.5%, which is much smaller than ~28% MR in Sr_2IrO_4 crystals without Pt [11]. This may be because the Pt layer, which has a higher conductivity, short circuit a good portion of the applied current through Pt. Since Pt layer has no MR contribution, the MR ratio of the whole double-layer sample goes down. This phenomenon can also be used to estimate how much current is driven through Pt and Sr_2IrO_4 layers.

(a)

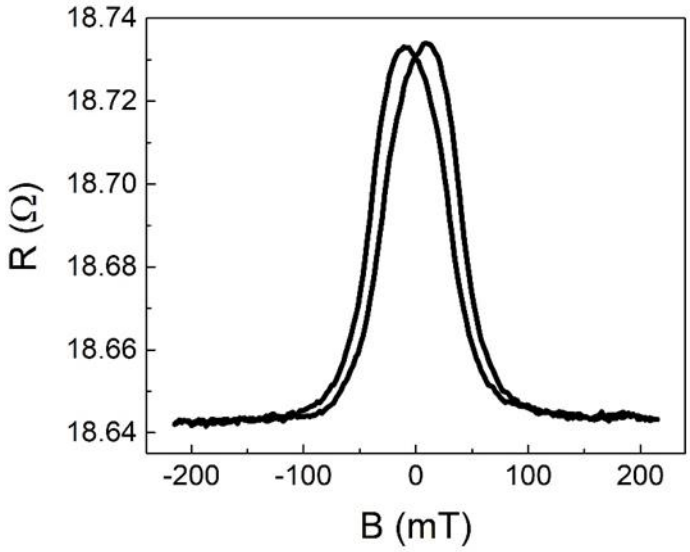

Fig. 2.4 (a) Magnetoresistance of Pt/Sr_2IrO_4 structure at liquid nitrogen temperature ~77K. Dc current is driven on Pt side.

(b)

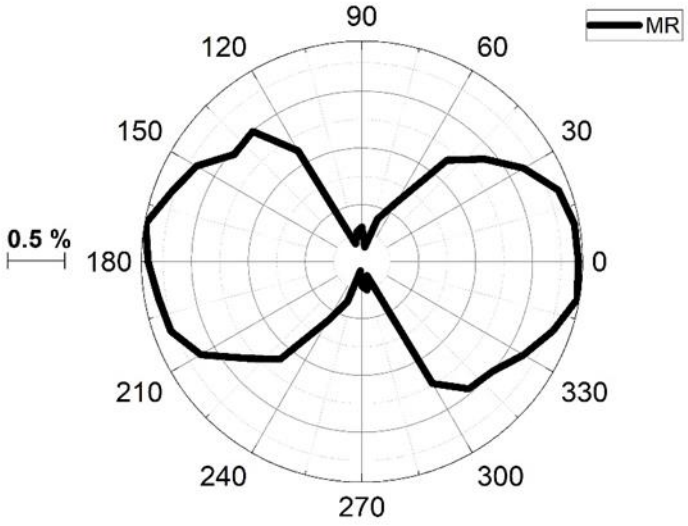

Fig. 2.4 (b) Anisotropic magnetoresistance of Pt/Sr_2IrO_4 structure

The same resistance vs. magnetic fields measurements were repeated with fields applied in different directions. Fig. 2.4 (b) shows anisotropic magnetoresistance of the structure. Previous study has already shown there is anisotropic magnetoresistance in single crystals of Sr_2IrO_4 [11]. However, our results are slightly different in the case of the Pt/Sr_2IrO_4 double-layer structure; only 2-fold symmetry was observed. No strong evidence of 4-fold symmetry was found at low magnetic fields. This may come from the fact that the previous study [11] used nanoscale point contacts and was focused on local transport effects; if the 4-fold symmetry is a local effect, it may not be reproducible on the macroscopic scale in our bulk transport measurements.

1.2.2 Magnetoresistance under Microwave Irradiation at Different Frequencies

In Fig. 2.5, microwaves are applied to the Pt/Sr_2IrO_4 sample on top of a 10mA dc current. The sample is cooled down to liquid nitrogen temperature ~77K. Microwaves have a fixed power of 10 dBm (at the output of microwave source) and their frequencies was varied from 2-8 GHz. Figures 2.5(a) and 2.5(c) show that the magnetoresistance doesn't change with microwave frequency; in panels (b) and (d), the signal from lock-in amplifier decreases with increasing frequency, but no sign of any resonance signal (e.g. ferromagnetic resonance) was found. The decrease of the lock-in signal with increasing frequency is because microwaves with different frequencies have a different efficiency of delivering power to the sample; in the case of our circuit configuration, lower frequencies are more efficient and deliver more microwave power into the sample. The fixed microwave power of 10 dBm at the output of microwave source doesn't necessarily mean that the sample receives the same amount of microwave power. MR is calculated after

white noise and drift are removed. The measurements were also repeated at different B field directions (not shown).

At first, the idea of this experiment was to use spin Hall effect enabled by Pt layer to exert a spin torque onto magnetic moments in Sr_2IrO_4. We were hoping to observe a resonance peak in the data from lock-in amplifier when magnetic field and microwaves are set to appropriate values. Antiferromagnetic resonance frequencies are generally beyond the upper limit of microwave frequencies available in our experiments. In [19], it has been shown that, in single crystals of Sr_2IrO_4, antiferromagnetic resonance modes are in the THz range. However, a weak ferromagnetism still exists in Sr_2IrO_4 and may result in a ferromagnetic resonance with frequencies in the GHz range. But after searching through all the available parameter space, our experiments didn't find any evidence of resonances in the Pt/Sr_2IrO_4 double-layer structure. It is possible that the Pt layer cannot generate a strong enough spin torque for such an observation.

(a)

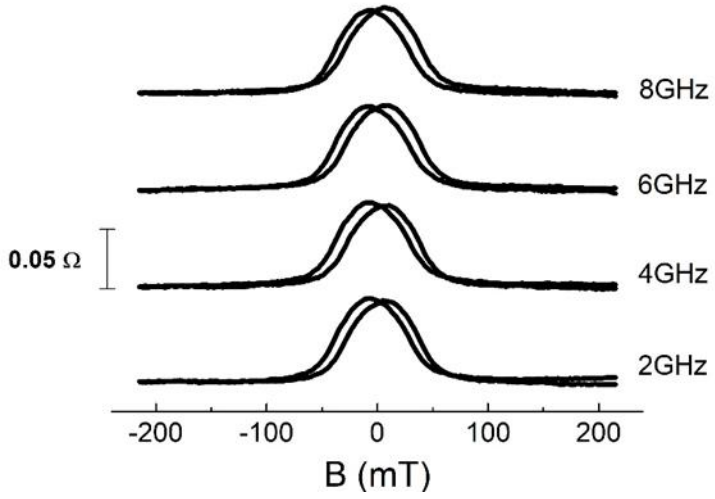

Fig. 2.5 (a) Resistance versus B fields with microwaves from 2GHz to 8GHz at fixed 10dBm input power and 77K. The resistance curves are offset for display. Notice that MR doesn't change with increasing microwave frequency.

(b)

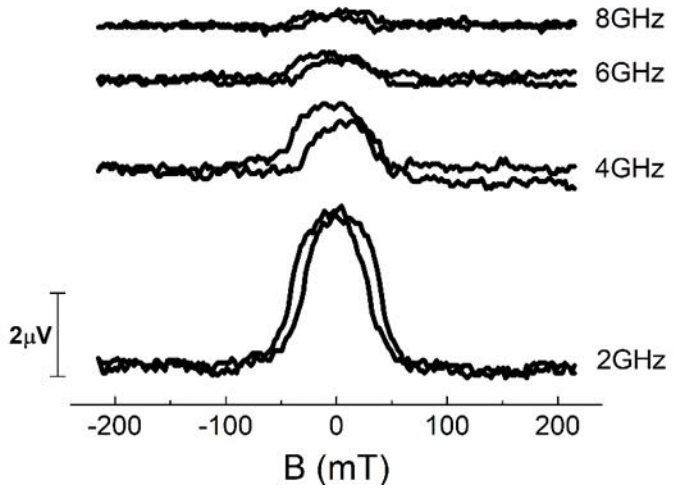

Fig. 2.5 (b) Readings from lock-in amplifier versus B fields with microwaves from 2GHz to 8GHz at fixed 10dBm input power and 77K. The curves are offset for display. Notice signals of MR become less obvious with increasing microwave frequency.

(c)

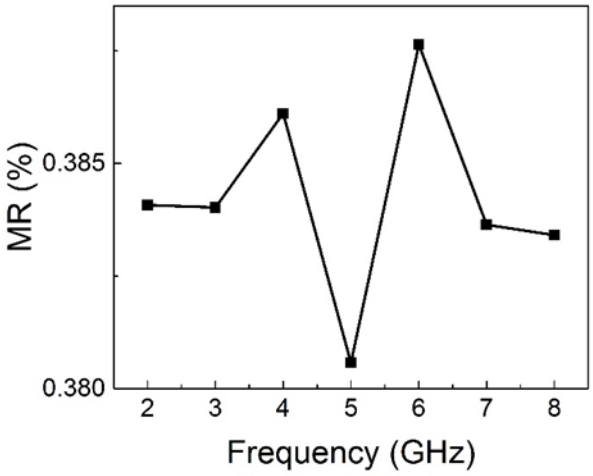

Fig. 2.5 (c) Normalized MR ratio with data subtracted from (a) versus microwave frequency at 77K. There is no obvious frequency dependence of MR, given fixed input power of 10 dBm.

(d)

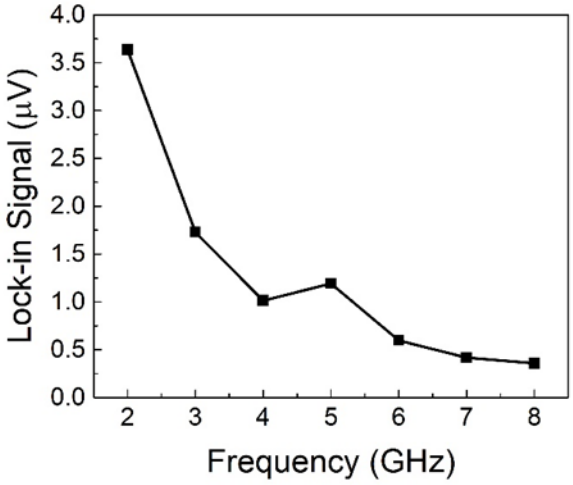

Fig. 2.5 (d) Readings (at low B fields) of lock-in amplifier versus microwave frequency with data subtracted from (b). The readings have a down trend because low frequency microwaves reach the sample more efficiently in the experiments.

1.2.3 Magnetoresistance under Microwave Irradiation at Different Power

Fig. 2.6 shows a normalized MR and the lock-in signal for 2 GHz microwaves applied to the sample at different levels of power (from 0-18 dBm) at the source output. The measurements were done with the applied dc current of 10 mA and at temperature 77 K. As indicated in Fig. 2.6(a), MR remains almost constant up to about 11 dBm and then decreases. In the data from lock-in amplifier [see Fig. 2.6(b)] the signal keeps going up with the microwave power. There are no resonance-like peaks in the lock-in signal at any power of the applied microwaves (not shown).

At a fixed microwave frequency (2 GHz), a higher output power of microwaves increases the effective power received by the sample, so the lock-in signal keeps increasing. The decrease in MR at higher powers may come from the heating effect of microwaves. As will be discussed later in this chapter, MR is suppressed at high temperatures while the heating by microwaves and dc currents may become significant and increase the sample temperature.

(a)

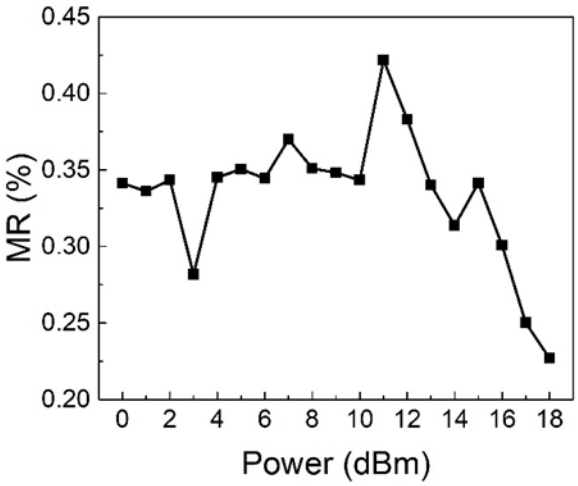

Fig. 2.6 (a) Normalized magnetoresistance ratio versus microwaves power with frequency fixed at 2GHz at 77K.

(b)

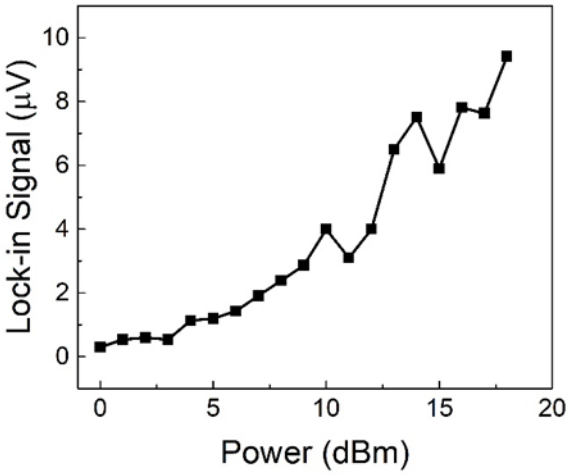

Fig. 2.6 (b) Readings (at low B fields) of lock-in amplifier versus microwave power with frequency fixed at 2GHz at 77K.

1.2.4 Effects of Microwaves and DC Current on MR Anisotropy

The anisotropic magnetoresistance is present in single crystals Sr_2IrO_4 [11]. Here we would like to see, with the Pt layer on top, if it is possible to change or affect this anisotropy with dc currents or microwaves.

In Figs. 2.7(a-d), microwaves are applied at fixed frequency (2 GHz) and fixed power (10 dBm), but dc currents through the sample change from 10 mA to 20 mA. Similar experiments have been done at higher currents (up to 30mA) and stronger microwave power (up to 15 dBm) (data not shown). We define the hard and soft angles of MR as angles between magnetic field directions and current direction (along the sample in ab-plane), where MR curve saturate at highest/lowest B values. The results show that hard and soft angles of MR are not changed by such combined variances in DC currents and microwave power.

(a)

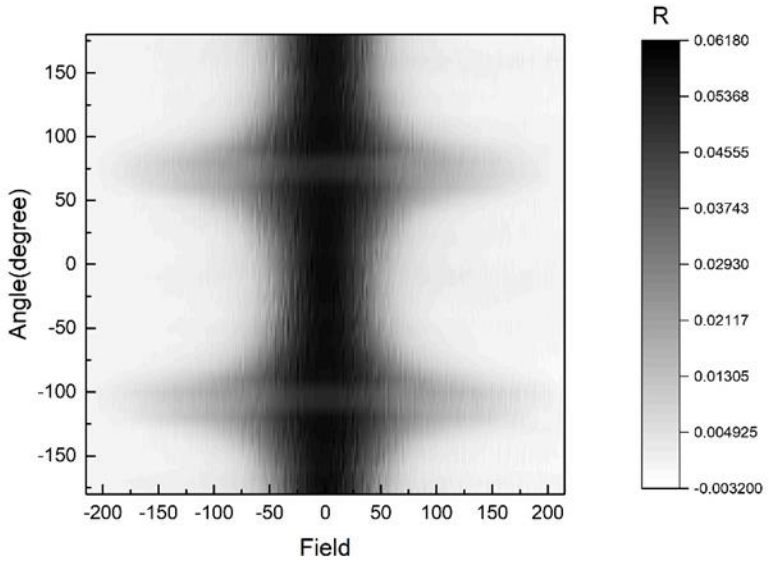

Fig. 2.7 (a) Anisotropic magnetoresistance with dc current set to 10mA, microwaves at 2GHz and 10 dBm

(b)

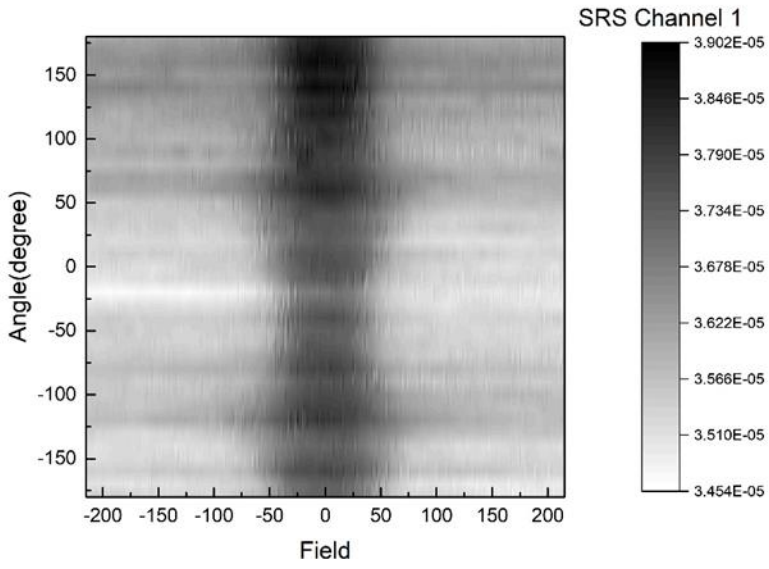

Fig. 2.7 (b) lock-in amplifier reading in the same setting as (a)

(c)

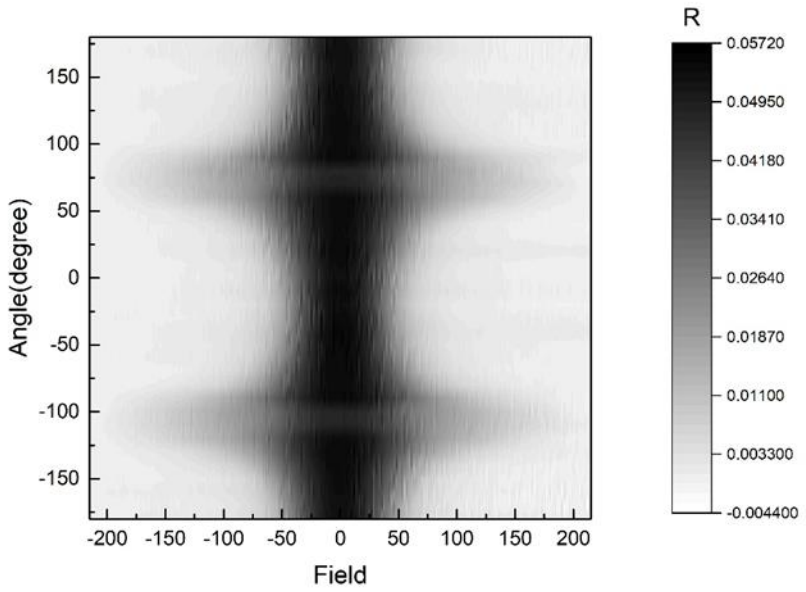

Fig. 2.7 (c) Anisotropic magnetoresistance with dc current set to 20mA, microwaves at 2GHz and 10 dBm.

(d)

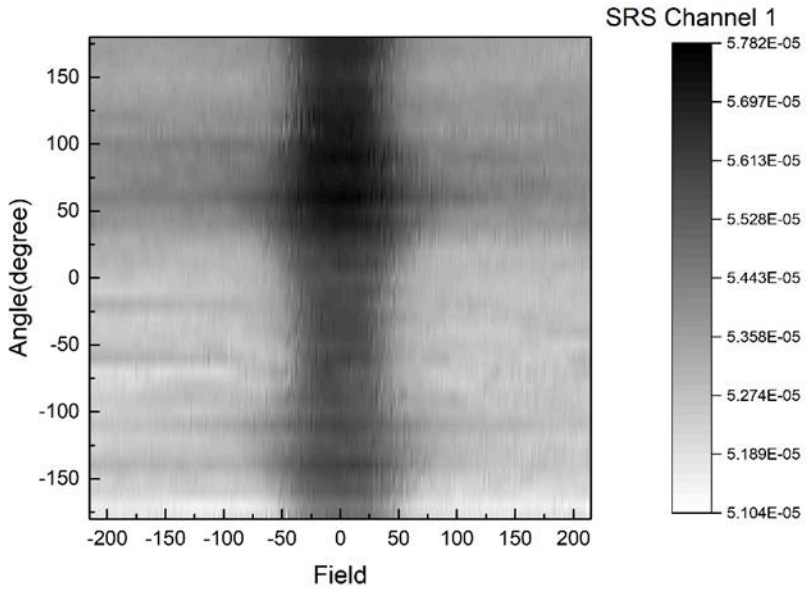

Fig. 2.7 (d) lock-in amplifier reading in the setting as (c)

1.2.5 Magnetoresistance at Higher Temperatures

Néel temperature of single crystal Sr_2IrO_4 is about 240K. Below 240K, single crystal Sr_2IrO_4 doesn't shown magnetoresistance. Here we can heat the Pt/Sr_2IrO_4 sample to temperatures above liquid nitrogen temperature but below Néel temperature to see any temperature influence on magnetoresistance.

Notice that (1) The deposited Pt layer may introduce extra impurities to the system and influence the Néel temperature (2) Resistance of Pt layer has different temperature dependence from Sr_2IrO_4: Pt tends to go down in resistance with lowering temperature while Sr_2IrO_4 resistance tends to go up. Combined effects will result in more and more current through Pt layer as temperature goes down, so MR of the double layer is smaller than single crystal at same temperatures.

Data in Fig. 2.8 was taken at temperatures higher than 77K where the double layer is going to lose MR. As indicated in the figures, the resistance becomes more linear to B fields and signals in lock-in amplifier becomes more like random drift., compared to Fig. 2.5 (b).

(a)

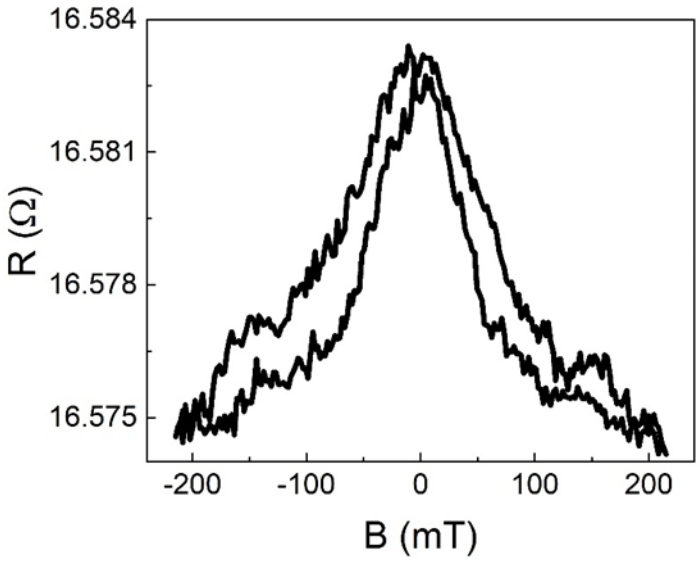

Fig. 2.8 (a) magnetoresistance when the sample is near transition temperature and about to lose magnetoresistance

(b)

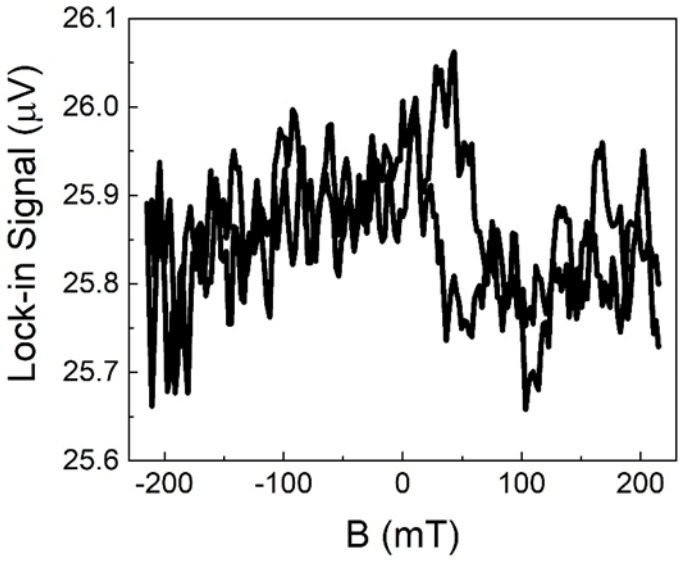

Fig. 2.8. (b) readings from lock-in amplifier at the same temperature

1.2.6 Suppression of Magnetoresistance by Joule Heating

In Fig. 2.9, MR was measured with varying dc currents. It is shown that high dc current was observed to suppress magnetoresistance. In our set-up, significant Joule heating can bring the sample near or even above Néel temperature so this effect may simply come from Joule heating rather than being related to spin Hall effect. More detailed research is needed here to separate effects from Joule heating and possible spin Hall effect.

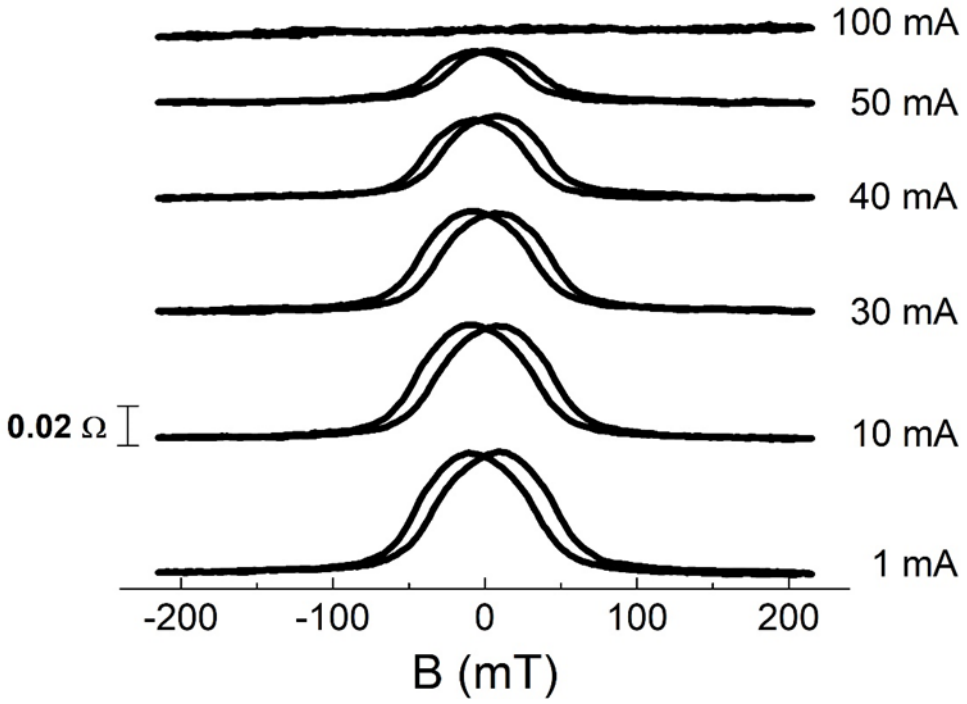

Fig. 2.9 Magnetoresistance of sample when different currents are sourced.

In this case, the sample was not sitting in liquid nitrogen bath but in a vacuum insulated chamber with original temperature of 77K. In this chamber it is highly possible that Joule heating can increase the sample temperature significantly.

1.2.7 Cooling Down Options

Fig. 2.10 shows anisotropic MR when sample was cooled down under different conditions. The idea was to apply B fields to tentatively pin magnetic moments in the sample when above Néel temperature, then cool down the system to see if magnetic moments are frozen differently. The cooling process has been experimented with combinations of (1) external B fields on, off and in different amplitudes (2) external B fields rotated to different angles regards to the sample (3) dc currents on, off and in different amplitudes. Fig. 1.10 shows part of the dataset. It turned out that such variance in cooling down conditions doesn't change magnetoresistance anisotropy.

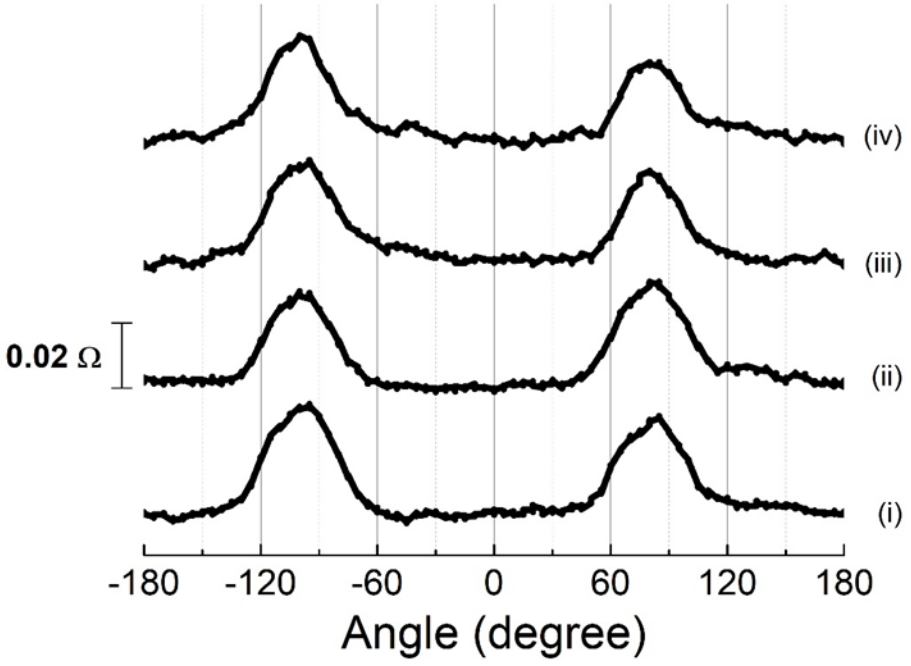

Fig. 2.10 Anisotropic magnetoresistance of sample at 77K under different cooling down conditions: (i) sample is cooled with 10mA DC current through in ab-plane and 220mT field applied at hard angle (ii) cooled down with 220mT field applied at hard angle (iii) cooled down with -220mT field applied at hard angle (iv) cooled down with 220mT field applied at soft angle. Here soft and hard means angles in which the sample is easy/difficult to magnetize, as indicated by anisotropic MR measurement

1.4 Comparison Between Transport Measurements On Different Sides Of The Double-Layer Structure

In this subsection, dc currents, microwaves and low frequency ac currents are driven through contacts on both Pt side and Sr_2IrO_4 side.

1.4.1 Magnetoresistance of Pt/Sr_2IrO_4 with DC Current Applied to Different Sides of the Structure

When dc currents are driven through Pt layer and Sr_2IrO_4 layer, magnetoresistance is not the same. Fig. 2.11 (a) and (b) show that in both cases MR ratio increases with DC current; on the Pt side, MR ratio increases relatively faster than Sr_2IrO_4 side, though MR ratio is also smaller on Pt side than Sr_2IrO_4 side. However, MR ratio is calculated as maximum resistance change under B fields divided by resistance at low or zero field. Since the resistance of Sr_2IrO_4 decreases with bias, as indicated in (e) and (f), a relatively stable ΔR can also lead to increase in MR ratio. Fig. 2.11 (c) shows that resistance changes are relatively at the same level with increasing currents on Sr_2IrO_4 side. While Fig. 2.11 (d) tells when DC currents are driven on Pt side, ΔR itself also increases. This is the most important result in this chapter because it (1) identifies certain current effect on Pt side which is not present on Sr_2IrO_4 side. (2) at the same time rules out Joule heating as increased current should tend to decrease magnetoresistance as already discussed.

Notice that on both Pt and Sr_2IrO_4 side, data becomes noisier when current goes above certain level (around 22-25mA, not shown). This is because of the resistive switching in the sample as indicated in Fig. 2.11 (e) and (f). Similar resistive switching has been studied previously in sister iridate $Sr_3Ir_2O_7$ [21]. When current goes beyond critical current, resistance is switched to higher state, and more noises are present in resistance

versus B fields curves. The unstableness of resistance at high state maybe come from internal lattice dynamics, as similar mechanism proposed for $Sr_3Ir_2O_7$ [21].

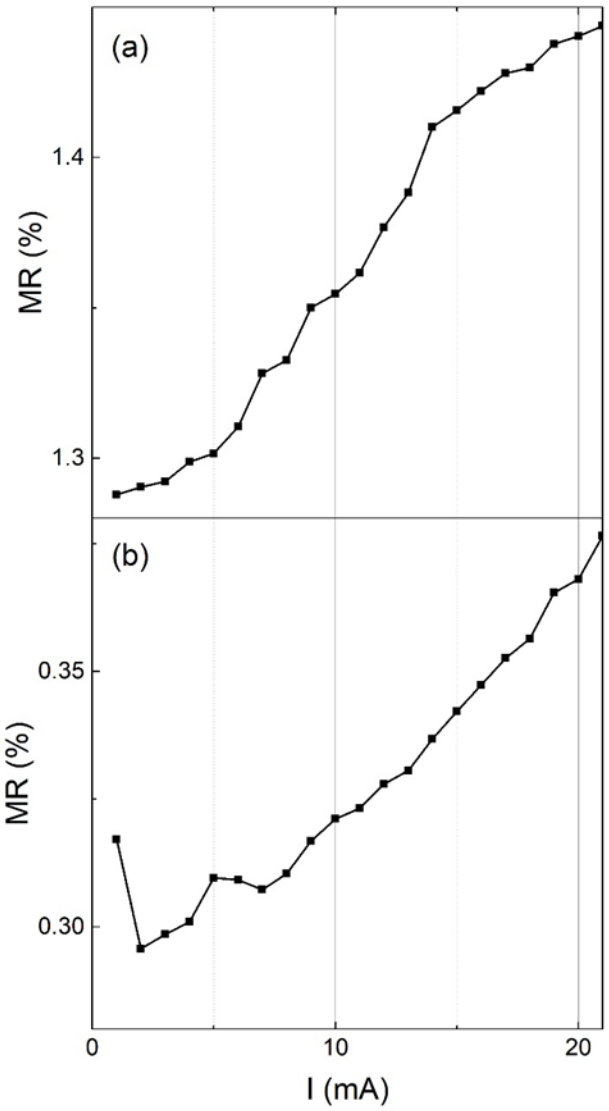

Fig. 2.11 (a) MR ratio at 77K under currents driven on Sr_2IrO_4 side (b) MR ratio at 77K under currents driven on Pt side.

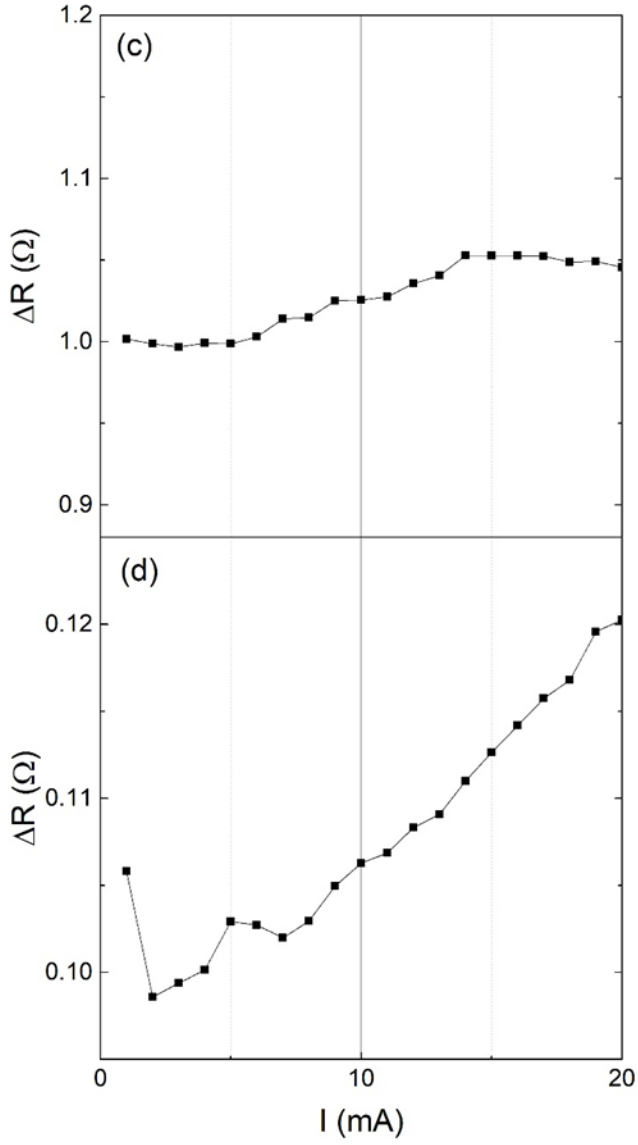

Fig. 2.11 (c) Maximum resistance changes under B fields and currents driven on Sr_2IrO_4 side (d) Maximum resistance changes under B fields and currents driven on Pt side

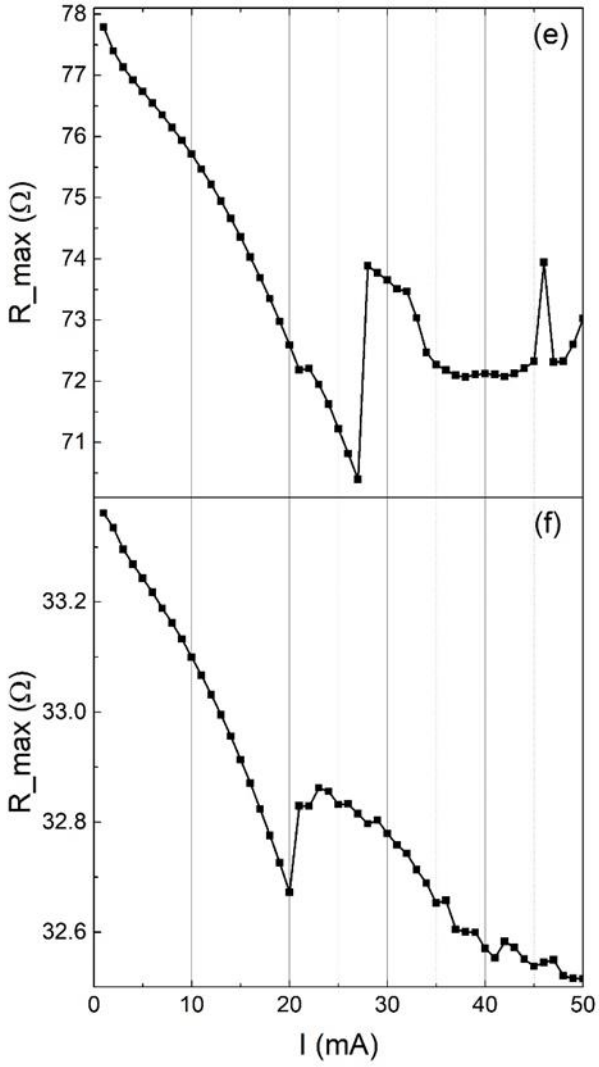

Fig. 2.11 (e) Maximum resistance under currents driven on Sr_2IrO_4 side (f) Maximum resistance under currents driven on Pt side

More detailed MR ratio versus dc currents on Pt side is given in Fig. 2.12. It is shown that dc current effects on Pt side are symmetric regards to current direction.

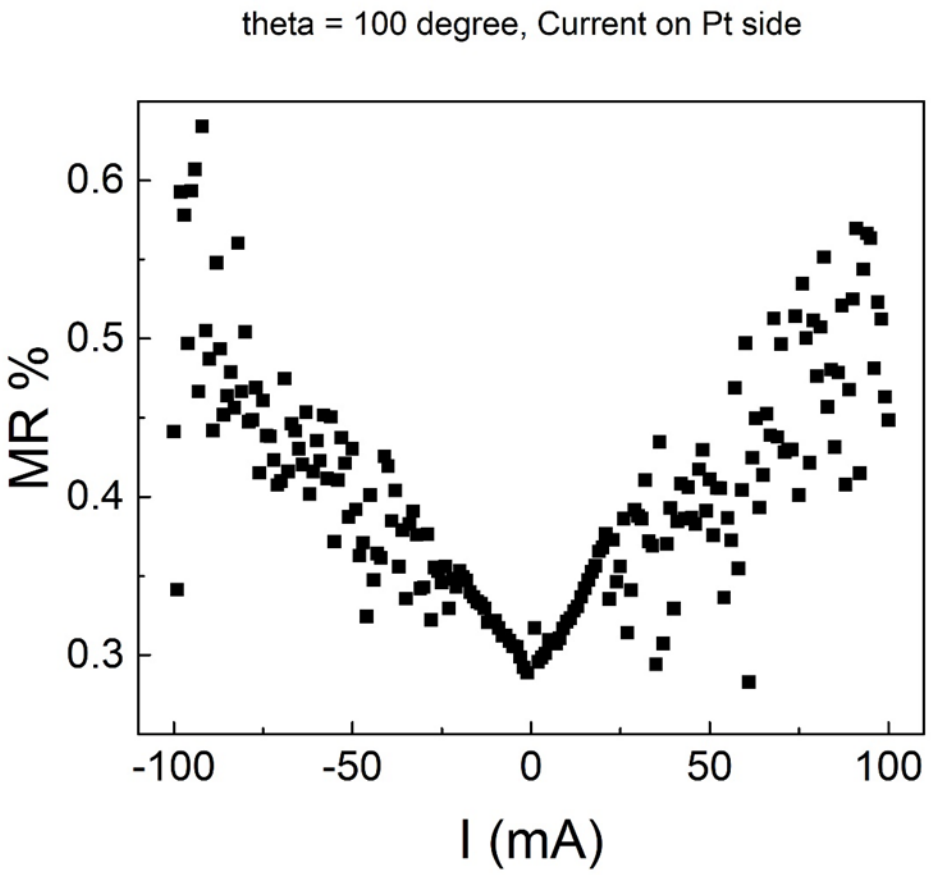

Fig. 2.12 Detailed MR ratio statistics under current driven on Pt side

1.4.2 Effects of Microwaves and AC Current on Resistive Switching

Fig. 2.13 (a) shows I-V characteristics of Pt/Sr_2IrO_4 sample at liquid nitrogen temperature of 77K. Dc current is driven on Pt side. The resistance switches to higher state when current goes beyond certain critical level; as current goes back below a second critical current, resistance switches back to low state. The two critical currents in up and down sweeps are different. This resistive switching is unipolar, which means it only requires bias of the same polarity; it is also symmetric and happens at both positive and negative current.

Fig. 2.13 (b) shows that critical currents during up sweeps can be tuned and pushed towards lower current level by applying higher and higher microwaves power at fixed frequency (2GHz). Low frequency ac currents have similar effects (Fig. 2.15). The microwaves frequencies are below antiferromagnetic resonant frequencies of THz, though in the ferromagnetic resonant frequencies of GHz. Ac currents have frequencies too low to excite any resonance. However, both microwaves and ac currents have contributions that act like an added-on dc bias and this equivalent 'added-on' of dc bias may explain why microwaves and ac currents bring down critical switching current.

Fig. 2.14 shows critical current Ic versus microwave power for 2GHz and 3GHz microwaves. The decrease of critical current with increasing microwaves power may be explained by that the 'added-on' dc bias by microwaves should increase with microwave power.

Fig. 2.15 shows critical current Ic versus low-frequency AC bias. There is a linear dependence of Ic on V.

(a)

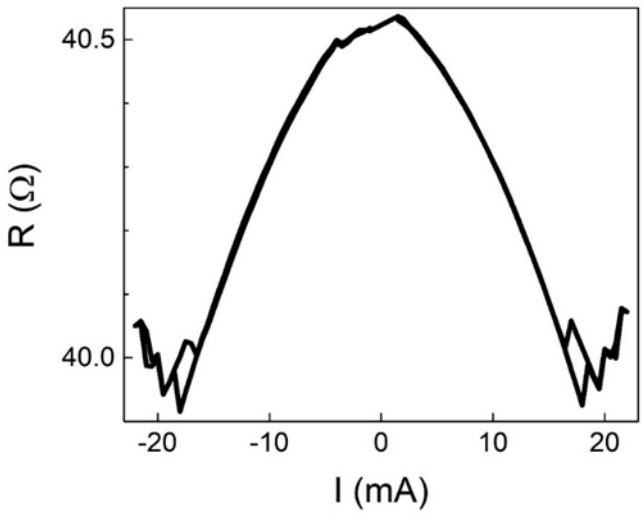

Fig. 2.13 (a) I-V characteristics of Pt/Sr_2IrO_4 sample at liquid nitrogen temperature 77K

(b)

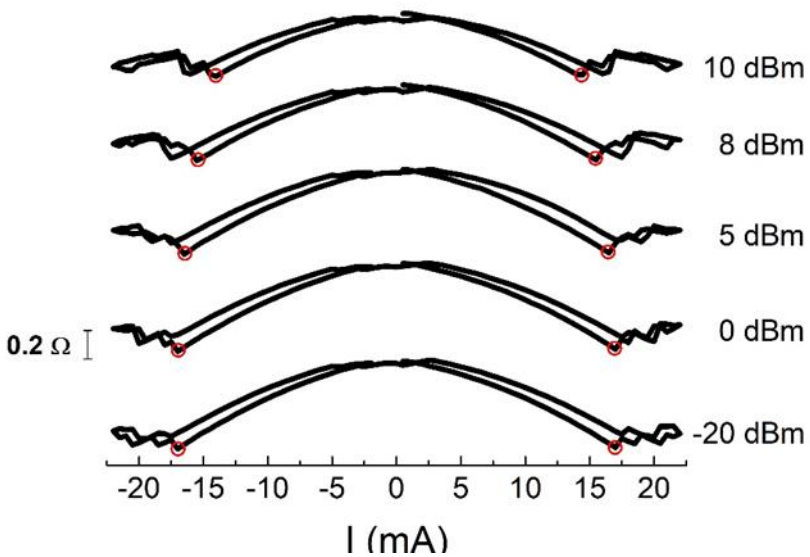

Fig. 2.13 (b) Microwave power affects critical currents during up sweeps at 77K.

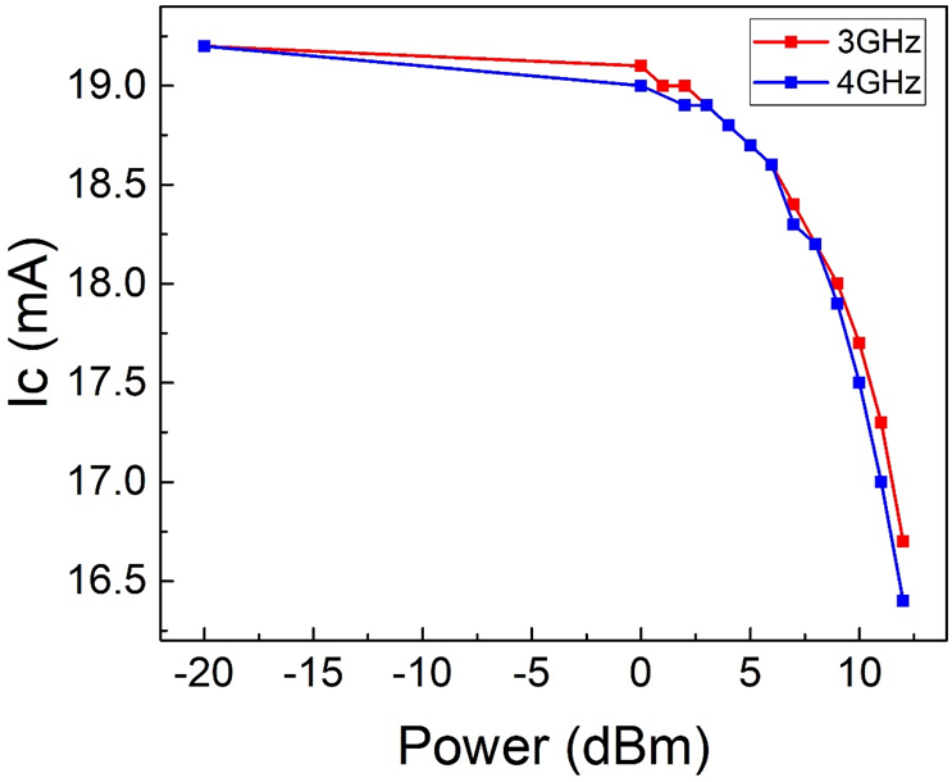

Fig. 2.14 Critical switching currents versus input microwave power under microwaves of 2GHz and 3GHz

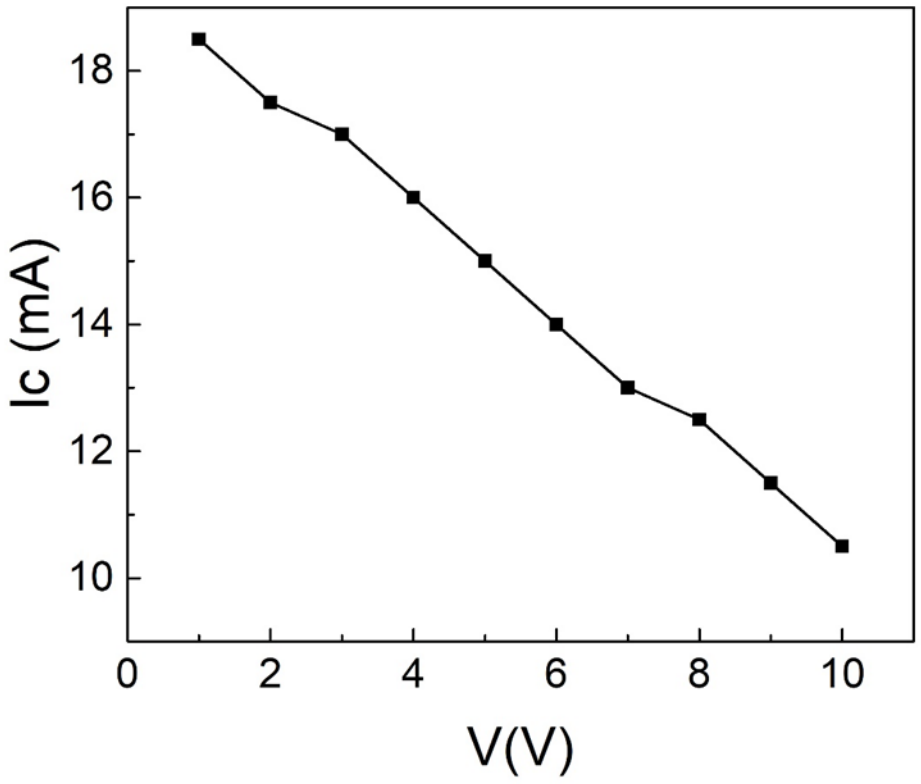

Fig. 2.15 Critical switching currents under low frequency ac currents, x-axis is the amplitude of ac biases

1.4.3 Comparison of Effective Power Generated by Microwaves and AC Current and Their Effects on Critical Current

When microwaves and ac currents are sent to the sample on top of dc current, an oscillating bias is added on top of dc bias. If there is only dc bias, a critical current or bias is needed for triggering switching; however, with the added oscillating bias, total effective bias can hit critical voltage with lower dc bias value. This picture can explain why microwaves and low frequency ac currents can bring down critical switching currents; but to confirm it, we need to quantify the 'added-on' bias brought by microwaves and ac currents. Microwave power is measured in dBm, which is power in logarithmic scale. The input power of microwaves is not the power essentially received by the sample; some of the input power is lost in the circuit. Ac currents are measured in volts, which describe the amplitudes of ac bias sent. Some of the ac bias is also distributed on other parts of the circuit with the sample receiving only a portion of it. To quantify the effects of microwaves and ac currents, the circuit needs to be re-used; sample responses to microwaves and ac currents, including signals in lock-in amplifier and sample resistance, can be used as indicators, so that we are able to bring microwaves (at different frequencies) and ac currents into a unified dimension which makes the comparison possible.

If we only compare microwaves at different frequencies and want to know how much effective bias the sample receives, we can use the readings from lock-in amplifier. In general, the level of readings of lock-in amplifier describes the strength of microwaves received by the sample. To calibrate the strength, we sent a small dc current to the sample and applied microwaves at different frequencies and power (dBm) to record the level in lock-in amplifier. For example, 5 dBm at 3GHz may result in the same lock-in amplifier reading as higher dBm at 5GHz. With a detailed test, a table (not shown) of lock-in amplifier readings, frequencies and power can be generated; later when microwaves are

sent to the sample, the table can be referenced to know how much microwave power the sample actually receives. We can use this conversion technique to reproduce Fig. 2.14 in the dimension of lock-in amplifier reading, as shown in Fig. 2.16. In this dimension, the dependence of critical currents becomes more linear. It is expected that this conversion should bring the logarithmic scale of dBm into a linear scale.

Fig. 2.17 gives critical currents versus input power for microwaves at 3-6GHz and Fig. 2.18 gives critical current versus effective power for these frequencies after the conversion is applied. In Fig. 2.16 and Fig. 2.18, curves of 3GHz and 4GHz overlap with each other but not with curves of higher frequencies. But curves of higher frequencies also look like straight lines in Fig. 2.18, though with different offsets. This variance in offsets may come from the inaccuracy in calibration. With curves of 3GHz and 4GHz, it is shown that switching currents are linearly dependent on the effective power received by the sample, regardless of microwave frequency.

But when it comes to ac currents, we need a new measure, rather than lock-in amplifier lever, to calibrate the effects. Here we use sample resistance as such measure. A small dc current is sent to the sample for reading out dc resistance. Microwaves at different frequencies and power and ac currents with different amplitudes are sent on top of dc current respectively. I-V characteristics of the sample tells us that the added bias (which is oscillating) brings the sample resistance down. We can use the amount of decrease in dc resistance to quantify microwaves' effects and ac currents' effects to apply a new dimension, which can be called effective or equivalent dc bias.

Fig. 2.19 puts ac current and microwaves together and displays their effects on critical current in the dimension of equivalent dc bias. As indicated in Fig. 2.19, for both ac current and microwaves at 2GHz and 3GHz, critical current is related to equivalent dc bias in a linear way, which in some degree supports the idea that the change in critical

currents is caused by the extra dc bias brought by microwaves and ac currents. Ac currents enable much more effective dc bias given the parameters allowed in the experiment than microwaves, so there is a large region in the data where microwaves are absent. This weakens the argument to some degree and encourages more related research in the future.

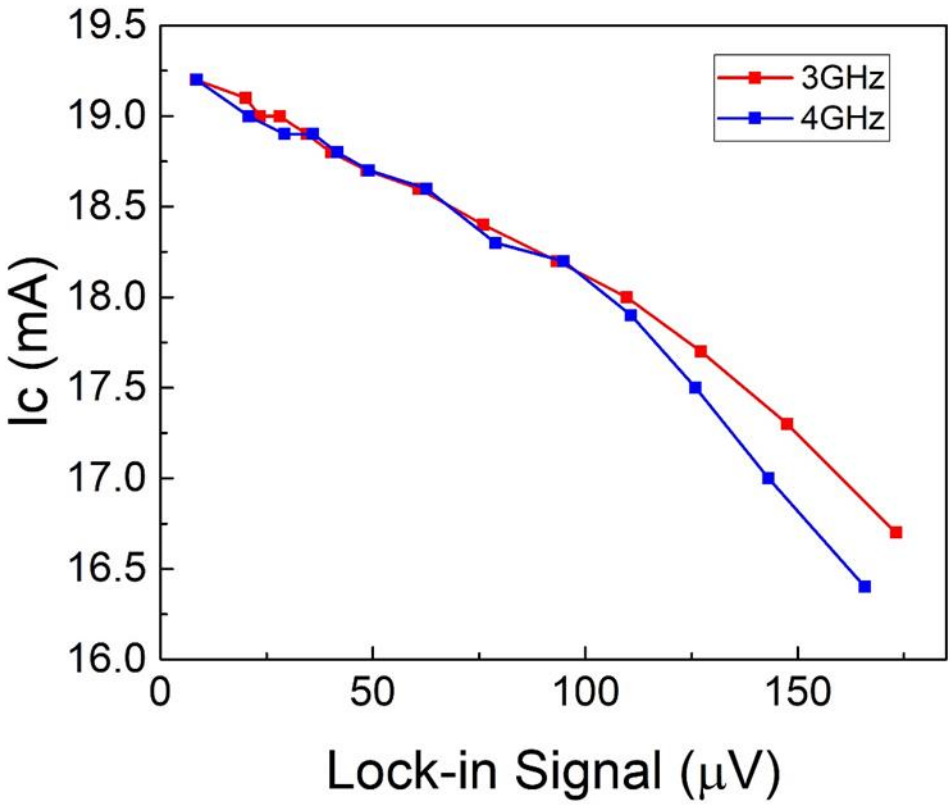

Fig. 2.16 Critical switching currents under microwaves power at 3GHz and 4GHz in the dimension of lock-in amplifier reading

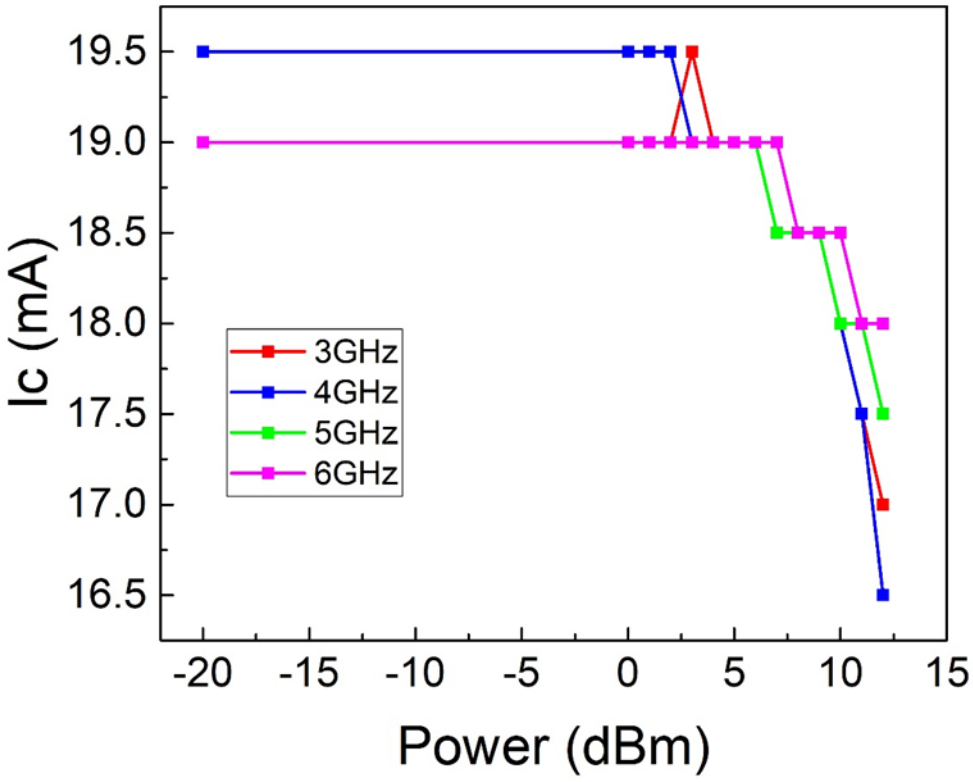

Fig. 2.17 Critical switching currents versus input power for microwaves 3GHz – 6GHz

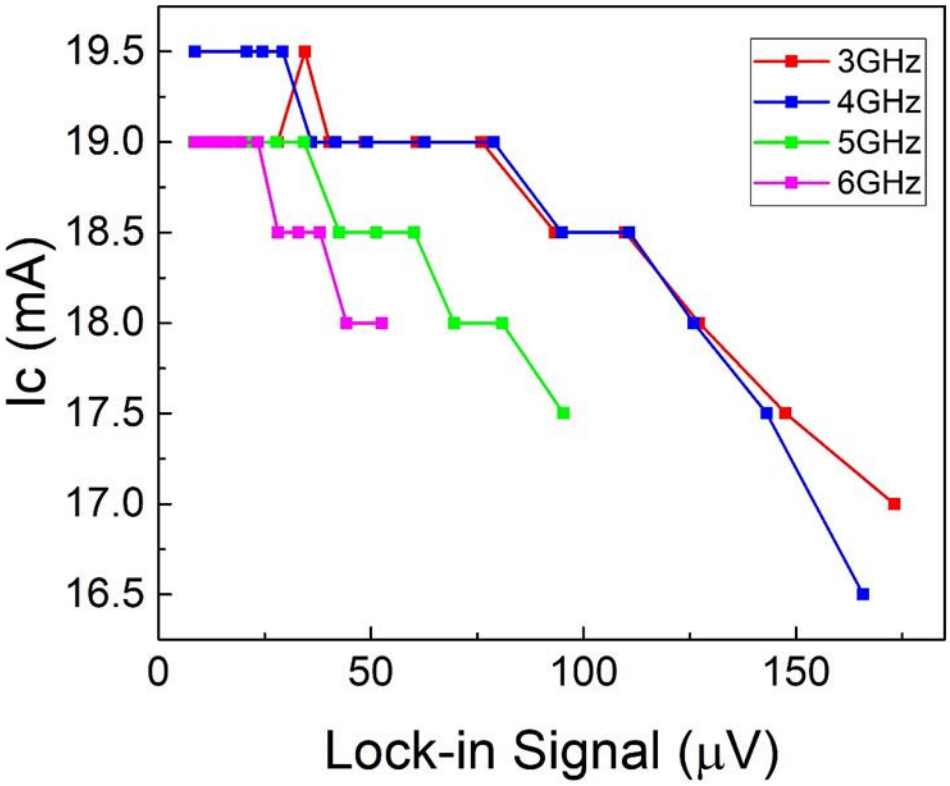

Fig. 2.18 Critical currents versus equivalent power for microwaves 3GHz – 6GHz

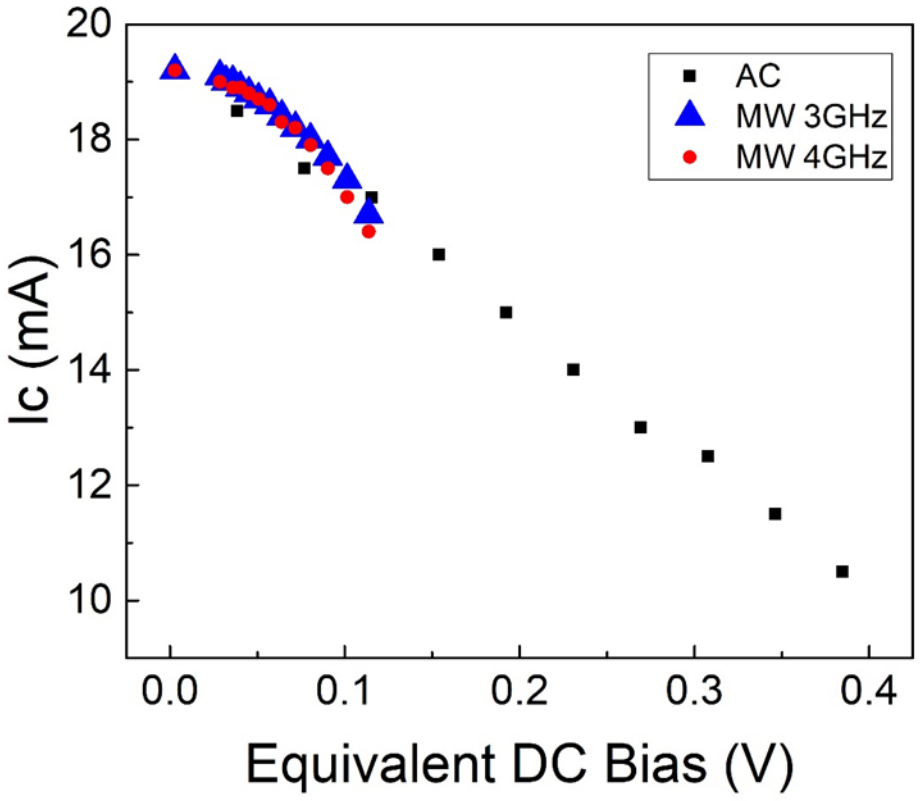

Fig. 2.19 Critical switching currents versus equivalent power for low frequency ac currents (black square), microwaves at 3GHz (blue triangle), and microwaves at 4GHz (red dot).

1.5 DISCUSSION AND CONCLUSIONS

The Pt/Sr_2IrO_4 structure studied in the experiments have ~0.5% magnetoresistance at liquid nitrogen temperature of 77K, which can be suppressed by Joule heating effect from dc current. The magnetoresistance is anisotropic and has 2-fold symmetry. The anisotropy of magnetoresistance is not affected by dc currents, microwave power or microwave frequencies.

When currents are driven on Pt side, magnetoresistance of Sr_2IrO_4 increases compared to the case when currents are driven on Sr_2IrO_4 side. This observation may be related to the spin injection from Pt layer mediated by spin Hall effect in Pt.

References

[1] Gang Cao and Pedro Schlottmann, The challenge of spin–orbit-tuned ground states in iridates: a key issues review, Rep. Prog. Phys. 81 042502 (2018)

[2] Zhao L, Torchinsky D H, Chu H, Ivanov V, Lifshitz R, Flint R, Qi T, Cao G and Hsieh D, Evidence of an odd-parity hidden order in a spin–orbit coupled correlated iridate Nat. Phys. 12 32 (2016)

[3] C. Wang, H. Seinige, G. Cao, J.-S. Zhou, J. B. Goodenough, and M. Tsoi, Temperature dependence of anisotropic magnetoresistance in antiferromagnetic Sr2IrO4, J. Appl. Phys. 117, 17A310 (2015).

[4] Kim B J et al, Novel Jeff = 1/2 Mott state induced by relativistic spin–orbit coupling in Sr2IrO4 Phys. Rev. Lett. 101 076402 (2008)

[5] Boseggia S, Walker H C, Vale J, Springell R, Feng Z, Perry R S, Moretti Sala M, Rønnow H M, Collins S P and McMorrow D F, Locking of iridium magnetic moments to the correlated rotation of oxygen octahedra in Sr2IrO4 revealed by x-ray resonant scattering, J. Phys.: Condens. Matter 25 422202 IOPscience (2013)

[6] Torchinsky D H, Chu H, Zhao L, Perkins N B, Sizyuk Y, Qi T, Cao G and Hsieh D, Structural distortion-induced magnetoelastic locking in Sr2IrO4 revealed through nonlinear optical harmonic generation Phys. Rev. Lett. 114 096404 (2015)

[7] Haskel D, Fabbris G, Zhernenkov M, Kong P P, Jin C Q, Cao G and van Veenendaal M, Pressure tuning of the spin–orbit coupled ground state in Sr2IrO4 Phys. Rev. Lett. 109 027204 (2012)

[8] Serrao C R et al, Epitaxy-distorted spin–orbit Mott insulator in Sr2IrO4 thin films Phys. Rev. B 87 085121 (2013)

[9] Ge M, Qi T F, Korneta O B, De Long D E, Schlottmann P, Crummett W P and Cao G, Lattice-driven magnetoresistivity and metal-insulator transition in single-layered iridates Phys. Rev. B 84 100402 (2011)

[10] C. Wang, H. Seinige, G. Cao, J.-S. Zhou, J. B. Goodenough, and M. Tsoi, Electrically Tunable Band Gap in Antiferromagnetic Mott Insulator Sr2IrO4, Phys. Rev. B 92, 115136 (2015).

[11] C. Wang, H. Seinige, G. Cao, J.-S. Zhou, J. B. Goodenough, and M. Tsoi, Anisotropic magnetoresistance in antiferromagnetic Sr2IrO4, Phys. Rev. X 4, 041034 (2014).

[12] Liu, L., Moriyama, T., Ralph, D. C. & Buhrman, R. A. Spin-torque ferromagnetic resonance induced by the spin Hall effect. Phys. Rev. Lett. 106, (2011).

[13] Liu, L. et al. Spin-torque switching with the giant spin hall effect of tantalum. Science (80-.). 336, 555–558 (2012).

[14] Hirsch, J. E. Spin Hall Effect. Phys. Rev. Lett. 83, 1834–1837 (1999).

[15] D'Yakonov, M. I. & Perel, V. I. Possibility of Orienting Electron Spins with Current. J. Exp. Theor. Phys. Lett. 13, 467 (1971).

[16] Sinova, J. et al. Universal intrinsic spin Hall effect. Phys. Rev. Lett. 92, (2004).

[17] Liu, L., Buhrman, R. A., Ralph, D. C., Review and Analysis of Measurements of the Spin Hall Effect in Platinum, arXiv:1111.3702 (2011)

[18] Hao, Q., Chen, W. & Xiao, G. Beta (β) tungsten thin films: Structure, electron transport, and giant spin Hall effect. Appl. Phys. Lett. 106, (2015).

[19] Bahr, S. et al. Low-energy magnetic excitations in the spin-orbital Mott insulator Sr2IrO4. Phys. Rev. B - Condens. Matter Mater. Phys. 89, (2014).

[20] G. Cao, S. McCall, J. E. Crow, and R. P. Guertin, Observation of a Metallic Antiferromagnetic Phase and Metal to Nonmetal Transition in Ca3Ru2O7, Phys. Rev. Lett. 78, 1751 (1997).

[21] H. Seinige, M. Williamson, S. Shen, C. Wang, G. Cao, J. Zhou, J. B. Goodenough, and M. Tsoi, Electrically tunable transport and high-frequency dynamics in antiferromagnetic Sr3Ir2O7, Phys. Rev. B 94, 214434 (2016).

CHAPTER 2

NON-DESTRUCTIVE REVERSIBLE RESISTIVE SWITCHING IN Cr DOPED MOTT INSULATOR Ca_2RuO_4: INTERFACE VS BULK EFFECTS[1]

This chapter presents a study of the transport properties of Cr-doped Mott insulator Ca_2RuO_4. The study revealed a decrease in the resistance of Ca_2RuO_4 single crystals as a function of the applied dc bias followed by a non-destructive reversible resistive switching at higher biases. It was shown that an applied electrical bias can reduce the dc resistance of Ca_2RuO_4 by as much as 75%; the original resistance of the sample could be restored by applying an electrical bias of opposite polarity. The resistive switching was studied as a function of the dc bias strength, applied magnetic field, and temperature. A combination of 2-, 3-, and 4-probe resistance measurements provided a means to distinguish between bulk and interfacial contributions to the switching and demonstrated that the switching is mostly an interfacial effect. The switching was tentatively attributed to electric-field driven lattice distortions which accompany the impurity-induced Mott transition. This field effect was confirmed by temperature-dependent resistivity measurements which show that the activation energy of this material can be tuned by an applied electrical bias. The observed resistive switching can potentially be used for building non-volatile memory devices like resistive random-access-memory.

[1] Based on *Non-destructive reversible resistive switching in Cr doped Mott insulator Ca2RuO4: Interface vs bulk effects, J. Appl. Phys. 122, 245108 (2017)*. As first author and the major contributor, Shida Shen conducted the experiments, collected and analyzed the data, and wrote the original draft.

2.1 INTRODUCTION

Tuning materials' properties by electrical means, e.g., by applying voltage, remains at the forefront of scientific and applied research because it can generate novel scientific phenomena and has an immense potential for future electronic devices. For instance, in conventional semiconductors like Si, the electronic band structure is fixed by the crystal structure and chemical composition and so defines the materials' transport and optical properties, which ultimately determine the performance of semiconductor devices such as diodes, transistors, and lasers. With an electrical control over the band structure, it would be possible to create a new generation of electronic and optical devices with enhanced functionality and flexibility. Such an electrical control has been previously demonstrated in 2D systems such as electrically gated bilayer graphene [1–3] and bulk 3D systems such as Sr_2IrO_4 [4] and $Sr_3Ir_2O_7$ [5]. Electrically driven metal-insulator transitions in transition-metal oxides [6,7] are of particular interest for practical use in electronic devices like resistive random-access-memory (Re-RAM) [8–10]. Here, metallic (low-) and insulating (high-resistance) states are used to encode information, while its reading and writing involve resistance sensing and electrically stimulated change of the states. It is essential for a functional device that the switching between the high- and low-resistance states could be driven at room temperature by low bias voltages. Recently, such a switching has been demonstrated in the multiband Mott insulator Ca_2RuO_4 [11]. However, Ca_2RuO_4 single crystals were found to disintegrate in the process of metal-to-insulator transition [11], which makes them impractical for applications. Here, we report a study of electronic transport properties of Cr-doped (2.5%) Ca_2RuO_4 single crystals under high electrical biases. Our temperature-dependent resistivity measurements unambiguously demonstrate that the activation energy in this material depends on the applied dc electrical bias. This bias dependence allows one to drive continuous variations in the sample resistivity by more

than 75% followed by a reversible resistive switching at higher biases. The switching between high- and low-resistance states is reversible, i.e., biases of different polarity can be used to “write” the system into different states and is also non-destructive, i.e., a repetitive switching between the different states can be realized. Our results suggest that Cr doping of Ca_2RuO_4 can be an effective route toward finding a material with desired switching characteristics for Re-RAM devices based on Ca_2RuO_4. We also found that switching is not affected by applied magnetic fields, which makes it robust to magnetic perturbations, but depends on the strength of the applied bias, which may potentially be used in devices with multilevel switching capabilities.

2.2 SAMPLES AND EXPERIMENTAL SETUP

Single crystals of Ca_2RuO_4 doped by Cr (2.5%) were grown by both the flux and the floating zone techniques [12]. The Cr-doped Ca_2RuO_4 crystallizes in the K_2NiF_4 structure (*Pbca* space group) with an intergrowth of the perovskite layer and the rock salt layer [13] and becomes antiferromagnetically ordered below the Néel temperature $T_N \approx$ 110 K [14,15]; the crystal structure was determined by single-crystal x-ray diffraction. Two Ag-paste contacts (area ~ 0.1 mm^2) were made on the opposite edges of a single-crystalline Ca_2RuO_4 flake with a thickness of about 0.2 mm and the c axis is normal to the flake's surface (area ~ 0.5 mm^2). The two Ag contacts were used to measure the sample resistance in a two-probe geometry; three- and four-probe measurements were performed (with two extra Ag contacts) to distinguish between bulk and interfacial contributions to the measured resistance. In magnetic fields (up to 250mT) applied parallel and perpendicular to the c axis and at temperatures from 150 to 300 K, we have characterized the dc transport properties of Cr-doped Ca_2RuO_4 by performing: (i) temperature-dependent resistivity measurements and (ii) current-voltage (I-V) characteristics.

2.3 RESULTS

2.3.1 Bias-dependent Activation Energy

Figure 3.1 (a) shows the temperature dependence of Ca_2RuO_4 2-probe resistance R(T) at a small bias (I = 0.1 mA). The inset to Fig. 3.1(a) shows the corresponding Arrhenius plot – ln(R) vs 1/T. From the plot's slope, we extracted [Fig. 3.1(b)] the activation energy at low bias ($\Delta \approx 100 - 240$meV for T = 150 – 240 K). By performing a similar analysis at different applied biases, we were able to reconstruct the bias dependence of the activation energy Δ at a fixed temperature. Figure 3.1(c) shows an example of such a reconstruction (Δ vs V) at T = 200 K. The activation energy in Ca_2RuO_4 decreases with increasing bias similar to the behavior observed previously in Sr_2IrO_4 [4] and $Sr_3Ir_2O_7$ [5]. In the case of iridates, the decrease of the gap has been attributed to the electric-field induced lattice distortions and their effect on electronic states and transport properties [4, 5]. Therefore, it is tempting to suggest that in experiments with Ca_2RuO_4, high local electric fields can also alter the equilibrium positions of oxygen ions with respect to ruthenium and stimulate distortions of the corner-shared RuO_6 octahedra, thus provoking modifications of the localized states and electronic structure. Such an electric-field effect can be taken into account with the field-effect model successfully used to fit similar temperature-dependent data in iridates [4, 5]:

$$\boldsymbol{R = R_0 e^{\frac{\Delta}{2k_B T}}, \Delta = \Delta_0 - A * |I|}$$

where Δ_0 is the activation energy at zero bias as extracted from Fig. 3.1(b), k_B is Boltzmann constant, and R_0 and A are fitting parameters.

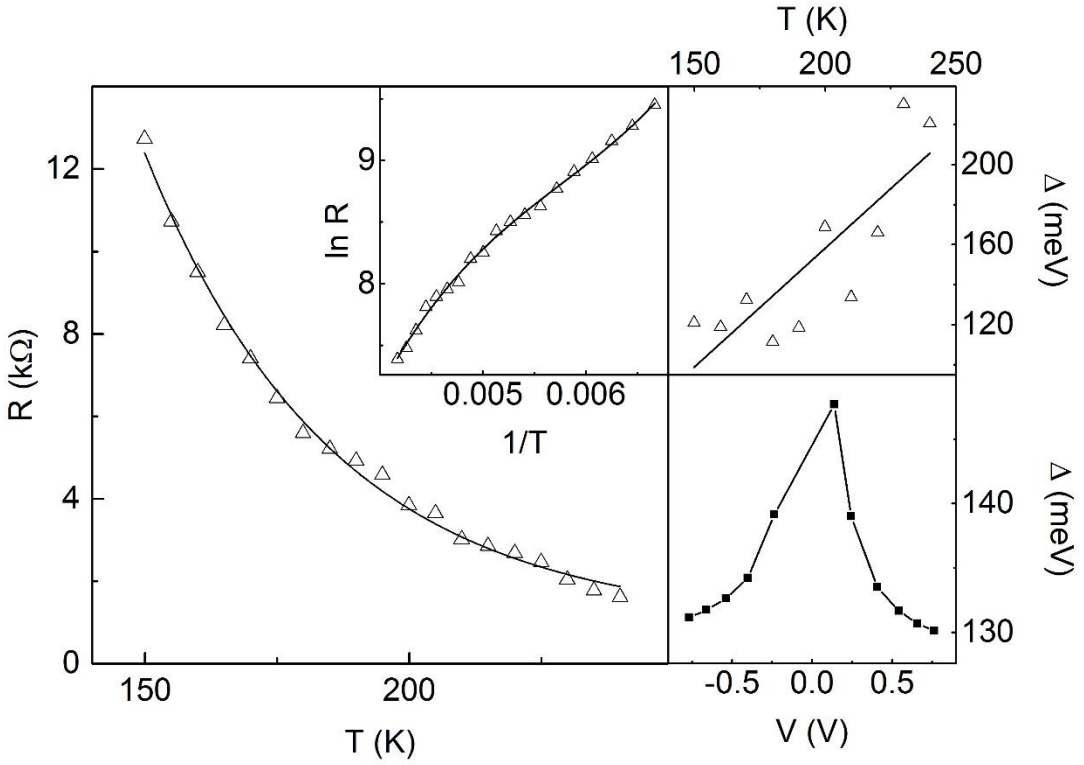

Fig. 3.1 Characterization of the bias-dependent activation energy from temperature-dependent resistivity measurements.

(a) Experimental data of R vs T (open triangles) at low bias; black curve – exponential fit. Inset: Arrhenius plot shows the same data as ln(R) vs 1/T.

(b) Temperature dependence of Δ as extracted from the slope of Arrhenius plot in (a); straight line is a guide for eye.

(c) The bias dependence of Δ at T = 200 K extracted from the ln(R) vs 1/T dependencies like in (a) measured at different biases (not shown).

2.3.2 Non-destructive Resistive Switching at Room Temperature

Figure 3.2 (a) shows the variation of Ca_2RuO_4 resistance R = V/I as a function of the applied bias voltage V at room temperature; the inset shows the corresponding I vs V characteristic. Arrows indicate the V-sweep directions: starting from zero bias (high-resistance state; solid red circle), the sample resistance decreases from about 2 k down to ~200 Ω as the positive bias increases up to 1.5 V. When the bias is then decreased back to zero, the sample remains in the low- resistance state (solid blue square). Only after the bias is reversed, increased to -1.5V, and then decreased to zero, the resistance goes back into the original high-resistance state ($R \approx 2$ kΩ; solid red circle). The R(V) curve thus exhibits a large clock-wise hysteresis. Such a hysteresis is consistent with a first-order Mott transition [16,17] during a V sweep observed previously in undoped Ca_2RuO_4 [11]. We should note, however, that there is a significant difference between the switching effects observed in Ref. 11 and in Fig. 3.2(a). In Ref. 11, the switching between high- and low-resistance states occurs at the same polarity of the applied voltage bias, i.e., the "flowing current" at a nonzero (e.g., positive) bias voltage plays a key role in maintaining the induced metallic state that disappears at zero bias. In contrast, opposite bias polarities are required to switch from high-to-low and low- to-high resistance states in Fig. 3.2(a); i.e., both high- and low- resistance states can be stabilized at zero bias without the "flowing current."

Three R vs V curves [Fig. 3.2(a)] measured in magnetic field (applied in the ab plane) of 0mT (open squares), 67.5 mT (triangles), and 135 mT (circles) illustrate the reproducibility of our measurements and the absence of any significant magnetic-field effects on the transition. The opening of the R(V) hysteresis depends on the maximum applied bias V. Four R vs V curves in Fig. 3.2(b) (open down-triangles, up- triangles, circles, and squares) show R(V) loops for four different values of the maxim positive bias

applied to the sample (0.8 V, 1 V, 1.2 V, and 1.5 V) while the maximum negative bias remains the same (-1.5V). The larger the applied bias, the larger the hysteresis and the corresponding change in resistance. Here, the low-resistance state has four different values (0.45, 0.8, 1.2, and 1.5 kΩ) as indicated by solid blue squares in Fig. 3.2(b). This finding may be potentially used for multilevel switching, e.g., in multistate Re- RAM.

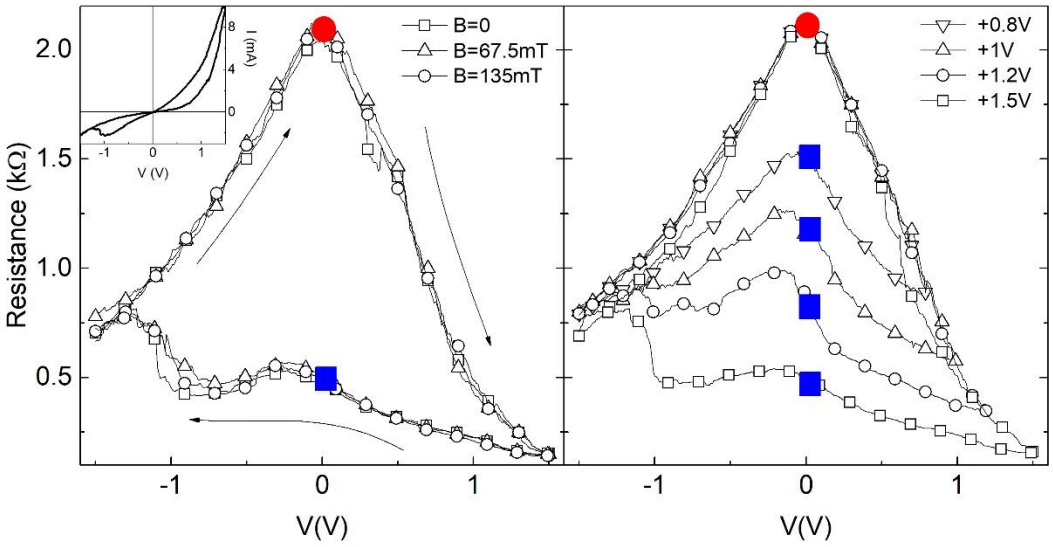

Fig. 3.2. I-V characteristics of Ca_2RuO_4 at room temperature.

(a) Resistance vs bias V. Inset: I(V) current vs voltage. The bias voltage changes from -1.5V to +1.5V and back. Arrows indicate the V-sweep directions. Open squares, triangles and circles show three R(V) curves measured in magnetic fields of 0mT, 67.5mT, and 135mT. Solid red (blue) circle (square) indicate the high- (low-) resistance states.

(b) Open down-triangles, up-triangles, circles, and squares show four R(V) curves with four different values of the maxim positive bias (0.8 V, 1 V, 1.2 V, and 1.5 V) while the maximum negative bias remains the same (-1.5 V).

2.3.3 Reproducibility Test for Switching

To test the reliability and reproducibility of switching between high- and low-resistance states, we have set a repetitive switching experiment between different states. From a R(V) curve (like in Fig. 3.2), we choose two states (solid red circle and blue square) that can be clearly distinguished at a low bias of 0.1 V; here, high- and low-resistances represent '0' and '1' states, respectively, of our Ca_2RuO_4 memory cell. A positive bias (1.5 V) is then used to switch the system from '0' to '1', while a negative high bias (-1.5V) is used to switch it back from '1' to '0'. Both '0' and '1' states can be read out by probing its resistance at a low bias of 0.1 V. In Fig. 3.3(a), an alternating voltage profile is applied to the sample to simulate the writing on a memory device. The applied voltage goes continuously through the sequence: +1.5 V, 0.1 V, -1.5 V, and 0.1 V. High biases are used to switch (write) the system between high- and low- resistance states, while low biases are used to read out the states. We routinely perform > 200 write-read cycles in our experiments as illustrated in Fig. 3.3(a). Here, open circles and left scale show the applied voltage sequence, while solid symbols and right scale show the measured resistance of the device. Figure 3.3(b) shows the resulting distributions of the measured resistance values of the two states, which indicate a larger uncertainty in the high-resistance state. High- and low-resistance states are clearly separated with the high/low resistance ratio of about 400%. These results show that switching in our Cr-doped Ca_2RuO_4 crystals is robust and makes this material a promising candidate for Re-RAM applications.

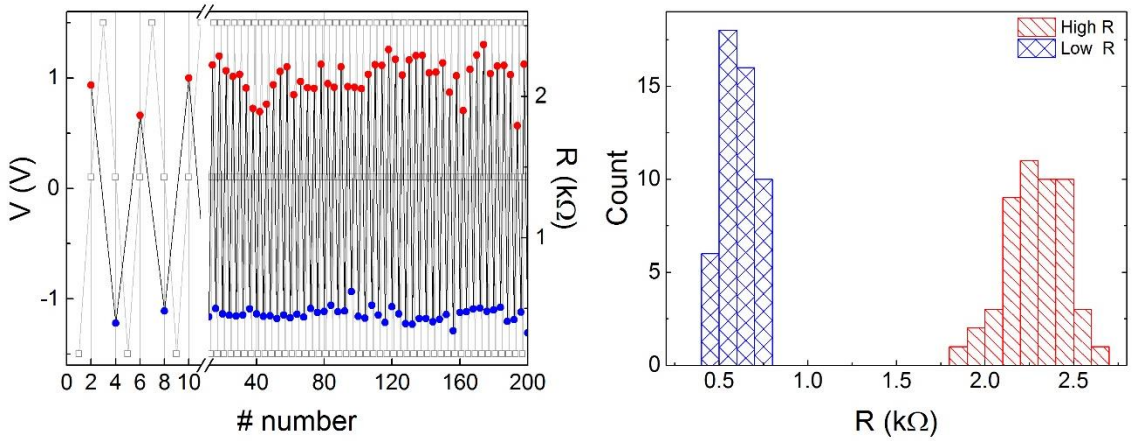

Fig. 3.3. Resistance switching under alternating biases.

(a) Grey trace and open squares (left scale) show an alternating voltage profile applied to the sample. High biases of ±1.5V are applied to switch between the high- and low-resistance states; low bias of +0.1V is used to probe the states.Red circles and blue squares (right scale) show resistance values measured at +0.1V. Resistance alternates between high and low resistances of the two states.

(b) Distributions of resistance values R_{high} and R_{low} of the two states.

2.3.3 Interfacial versus Bulk Crystal's Contribution to Switching

In pure Ca_2RuO_4, the insulator-to-metal transition (IMT) was previously associated with an electric-field induced structural transition [11] that results in a pronounced change in its transport properties. Here, the structural transition refers to a change in the material structure of Ca_2RuO_4 was probed in Ref. 11 by X-ray diffraction. A valid alternative to this picture is the impurity-driven IMT where the Mott insulator becomes a metal via excitation of carriers from an impurity bound state (indirect band) to its conduction band [18,19]. In $Ca_2Ru_{1-x}Cr_xO_4$, the Cr doping is expected to induce holes in the lower Hubbard band. It is

possible that the local hole concentration is altered by the electric field (applied bias) that triggers IMT. This impurity-driven mechanism suggests an enhanced effect near interfaces because they have more impurities compared to the bulk. Next, we examine whether the transition is associated with the bulk or interfacial resistance switching, i.e., whether the switching occurs in the bulk of a sample or near the interfaces between the sample and electrodes (Ag-paste contacts in our experiments). In order to distinguish between the bulk and interfacial contributions, we carried out 2-, 3-, and 4-probe resistance measurements using four Ag-paste contacts to another piece of Ca_2RuO_4 single crystal.

Figures 3.4 (a) – 3.4 (d) show R(V) curves recorded in 2-, 3-, and 4-probe measurements at room temperature; insets show the corresponding wiring schemes. In a two-probe configuration of Fig. 3.4 (a), the resistance is measured across the same two contacts used to supply current and is expected to include resistance contributions from the sample bulk and two interfaces between the sample and Ag contacts #1 and #4. The three-probe configurations of Figs. 3.4 (b) and 3.4 (c) involve a bulk contribution and only one Ag contact: #1 for (b) and #4 for (c). Finally, the four-probe configuration in Fig. 3.4 (d) is expected to provide only the bulk resistance without any contributions from interfaces. Note that the different configurations have different resistances that defines different V-scales for Figs. 3.4 (a) – 3.4 (d). This difference is particularly noticeable in the four-probe configuration of Fig. 3.4 (d), where the resistance is about two orders of magnitude smaller than in the other three configurations. Here the measured small variations in resistance [grey data points in Fig. 3.4 (d)] have a relatively high noise level. To increase the signal-to-noise ratio in this configuration, we have averaged 100 R(V) curves [solid black curve in Fig. 3.4 (d)].

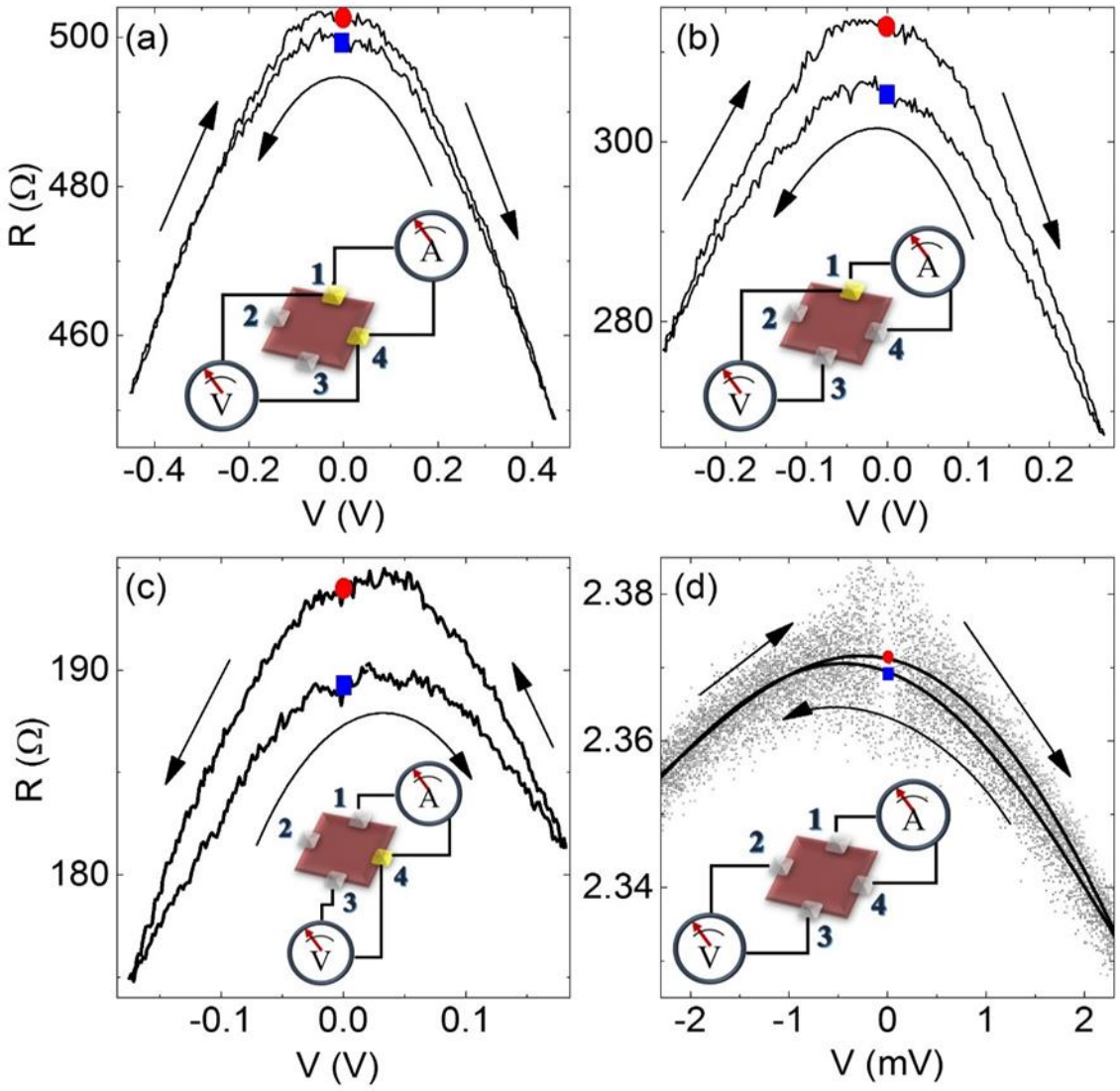

Fig. 3.4. R(V) curves recorded in (a) 2-, (b-c) 3-, and (d) 4-probe measurements. Insets show the corresponding wiring schemes.

To summarize the outcome of these measurements, (i) a hysteresis in R(V) is observed in all four configurations, although the hysteresis opening and the corresponding difference between the high- and low- resistance states (R_{high} and R_{low}) probed at 0.1 V (see solid red circles and blue squares in Fig. 3.4) vary significantly in different configurations. To quantify the difference, we use the ratio $(R_{high} – R_{low})/R_{low}$, which is the largest (2%–2.5%) in three-probe measurements and lowest (0.16%) in four-probe measurements. The two- probe geometry shows an intermediate effect (0.7%). We thus conclude that interfaces contribute more to the resistance change, which may be partially associated with higher electric fields inevitably present at interfaces due to band bending. Another observation that can be made from data in Figs. 3.4 (a) – 3.4 (d) is (ii) a different sense of circulation of the hysteresis loops: clockwise in (a), (b), and (d), and anti- clockwise in (c). In all three-probe measurements we have performed on our Ca_2RuO_4 crystals [like those in Figs. 3.4 (b) and 3.4 (c)], the direction of the loop circulation is different for the two interfaces that supply electrical bias to the sample. This is consistent with the opposite polarity of electric fields near the two interfaces and supports our previous conclusion of the predominant interfacial contribution to the resistance change. The exact magnitude of the resistance change from any given interface/contact is ultimately defined by local properties of the contact of interest and, unfortunately, is not readily controlled in our experiments with Ag-paste contacts. This problem calls for further investigations with other contact types to maximize the switching effect. In our experiments, we found that the resistance change measured in two- probe geometry, like the one in Fig. 3.4 (a), is a simple algebraic sum of individual contributions from the two involved contacts/interfaces [Figs. 3.4 (b) and 3.4 (c)] and the bulk [Fig. 3.4 (d)]. Since the two interfaces produce resistance changes of opposite polarities, they partially compensate each other and result in a smaller (intermediate) effect in the two-probe geometry.

2.3.4 Effects of Temperature on Switching

Finally, we studied the effects of temperature on the resistive switching effect. Red and blue traces in Fig. 3.5 show the temperature dependencies of R_{high} and R_{low} states, respectively. The resistance states were extracted from R(V) measurements like those in Fig. 3.2. Inset to Fig. 3.5 shows the temperature dependence of the ($R_{high} - R_{low}$) difference. It is shown that low temperature suppresses the switching; the switching effect is present only above 260 K. At low temperatures, there is no switching, and the sample resistance increases exponentially with decreasing temperature in agreement with a simple picture of thermally activated transport [see Eq. (2.1) and Fig. 3.1(a)].

However, the temperature dependent measurements were done at fixed bias range, i.e. the maximum applied biases remained the same in the whole temperature range. Resistance of Ca_2RuO_4 increases very fast at low temperatures, which may have a scaling effect on critical bias for switching; at low temperatures, much higher bias needs to be applied to trigger resistive switching. This may explain what Fig. 3.5 presents to us.

Another interpretation/explanation comes from the suppression of the switching at low temperatures to suppressed lattice distortions/structural transition; the latter could be associated with the *L-Pbca* to *S-Pbca* phase transition which in a pure Ca_2RuO_4 occurs at about 360 K but may be lowered to 260 K by Cr doping. A change in the slope of R(T) around 260 K in Fig. 3.5 is consistent with this hypothesis. However, further studies are needed to verify whether the anomaly at 260 K is indeed associated with the structural transition.

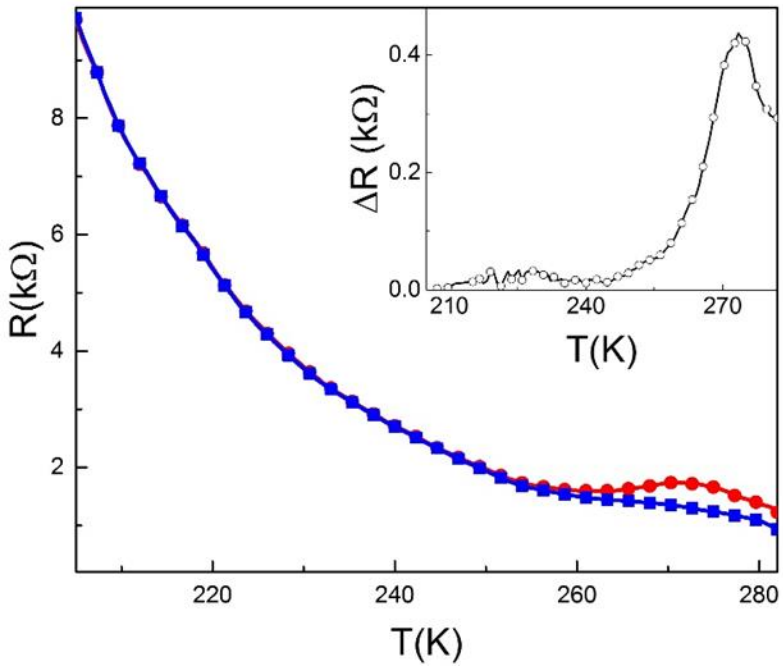

Fig. 3.5. Switching vs temperature.

Inset: the difference $\Delta R = R_{high} - R_{low}$ as a function of temperature.

Blue squares and red circles show temperature dependencies of R_{high} and R_{low} states.

2.4 DISCUSSION AND CONCLUSIONS

To conclude, electrically tunable band-gap and non- destructive resistive switching were all found in the Cr- doped (2.5%) Mott insulator Ca_2RuO_4. We observed a continuous reduction in the resistivity of Ca_2RuO_4 crystals as a function of increasing bias followed by an abrupt switching at higher biases. These results follow a chain of observations in other oxide systems such as Sr_2IrO_4 [4] and $Sr_3Ir_2O_7$ [5] and corroborate the idea of an electric-field effect on electronic states in these materials. This field effect was confirmed in Ca_2RuO_4 by temperature-dependent resistivity measurements that show that the activation energy of this material can be tuned by an applied DC electrical bias. Our two-, three-, and four-probe resistance measurements suggest that the resistive switching observed in Ca_2RuO_4 is primarily associated with the interfacial regions between the sample and contact (Ag-paste) electrodes. The switching was tentatively attributed to electric field-driven lattice distortions that accompany the impurity-induced Mott transition [18, 19]. The reversible resistive switching can potentially be used as a switching mechanism in industrial applications, e.g., in non- volatile memory devices like a resistive random-access-memory (Re-RAM). Our observation of the non-destructive switching in Cr-doped Ca_2RuO_4 opens a viable pathway to solve the disintegration problem in resistive switching oxides and, with further optimization of dopant material and doping level, can provide optimal performance (including resistance ratio and repetition characteristics) for such applications.

References

[1] J. B. Oostinga, H. B. Heersche, X. Liu, A. F. Morpurgo, and L. M. K. Vandersypen, Gate-induced insulating state in bilayer graphene devices, Nat. Mater. 7, 151 (2008).

[2] Y. Zhang, T.-T. Tang, C. Girit, Z. Hao, M. C. Martin, A. Zettl, M. F. Crommie, Y. R. Shen, and F. Wang, Direct observation of a widely tunable bandgap in bilayer graphene, Nature 459, 820 (2009).

[3] E. V. Castro, K. S. Novoselov, S. V. Morozov, N. M. R. Peres, J. M. B. L. Dos Santos, J. Nilsson, F. Guinea, A. K. Geim, and A. H. C. Neto, Biased Bilayer Graphene: Semiconductor with a Gap Tunable by the Electric Field Effect, Phys. Rev. Lett. 99, 216802 (2007).

[4] C. Wang, H. Seinige, G. Cao, J.-S. Zhou, J. B. Goodenough, and M. Tsoi, Electrically tunable transport in the antiferromagnetic Mott insulator Sr2IrO4, Phys. Rev. B 92, 115136 (2015).

[5] H. Seinige, M. Williamson, S. Shen, C. Wang, G. Cao, J. Zhou, J. B. Goodenough, and M. Tsoi, Electrically tunable transport and high-frequency dynamics in antiferromagnetic Sr3Ir2O7, Phys. Rev. B 94, 214434 (2016).

[6] G. I. Meijer, Who wins the nonvolatile memory race? Science, 319, 1625 (2008).

[7] R. Waser, M. Aono, Nanoionics-based resistive switching memories, Nat. Mater 6, 833 (2007).

[8] H. Akinaga and H. Shima, Resistive Random Access Memory (ReRAM) Based on Metal Oxides, Proc. IEEE 98, 2237 (2010).

[9] G. Bersuker, D. C. Gilmer, D. Veksler, P. Kirsch, L. Vandelli, A. Padovani, L. Larcher, K. McKenna, A. Shluger, V. Iglesias, M. Porti, and M. Nafria, Metal oxide resistive memory switching mechanism based on conductive filament properties, J. Appl. Phys. 110, 124518 (2011).

[10] H. S. P. Wong, H. Y. Lee, S. Yu, Y. S. Chen, Y. Wu, P. S. Chen, B. Lee, F. T. Chen, and M. J. Tsai, Metal–Oxide RRAM, Proc. IEEE 100, 1951 (2012).

[11] F. Nakamura, M. Sakaki, Y. Yamanaka, S. Tamaru, T Suzuki and Y. Maeno, Electric-field-induced metal maintained by current of the Mott insulator Ca2RuO4, Sci. Rep 3, 2536 (2013).

[12] T. F. Qi, O. B. Korneta, S. Parkin, L. E. DeLong, P. Schlottmann and G. Cao, Single-Crystal Ca2Ru1-xCrxO4, Phys. Rev. Lett. 105, 177203 (2010).

[13] M. Braden, G. André, S. Nakatsuji, and Y. Maeno, Crystal and magnetic structure of Ca2RuO4: Magnetoelastic coupling and the metal-insulator transition, Phys. Rev. B 58, 847 (1998).

[14] G. Cao, S. McCall, M. Shepard, J.E. Crow and R.P. Guertin, Magnetic and Transport Properties of Single Crystal Ca2RuO4: Relationship to Superconducting Sr2RuO4, Phys. Rev. B 56, R2916 (1997).

[15] C. S. Alexander, G. Cao, V. Dobrosavljevic, E. Lochner, S. McCall, J. E. Crow and P. R. Guertin, Destruction of the Mott Insulating Ground State of Ca2RuO4 by a Structural Transition, Phys. Rev. B 60, R8422 (1999).

[16] O. Friedt, M. Braden, G. André, P. Adelmann, S. Nakatsuji, and Y. Maeno, Structural and magnetic aspects of themetal-insulator transition in Ca2-xSrxRuO4. Phys. Rev. B 63, 174432 (2001).

[17] P. Steffens, O. Friedt, P. Alireza, W. G. Marshall, W. Schmidt, F. Nakamura, S. Nakatsuji, Y. Maeno, R. Lengsdorf, M. M. Abd-Elmeguid, and M. Braden, High-pressure diffraction studies on Ca2RuO4. Phys. Rev. B 72, 094104 (2005).

[18] H.-T. Kim, B.-G. Chae, D.-H. Youn, S.-L. Maeng, G. Kim, K.-Y. Kang, and Y.-S. Lim, Mechanism and observation of Mott transition in VO2-based two- and three-terminal devices. New J. Phys. 6, 52 (2004).

[19] H.-T. Kim, M. Kim, A. Sohn, T. Slusar, G. Seo, H. Cheong, and D.-W. Kim, Photoheat-induced Schottky nanojunction and indirect Mott transition in VO2: photocurrent analysis. J. Phys.:Condens. Matter 28, 085602 (2016).

CHAPTER 3

RESISTIVE SWITCHING, LATTICE DISTORTIONS, AND JOULE HEATING IN La_2NiO_4 SINGLE CRYSTALS

This chapter presents a study of the transport properties of La_2NiO_4 single crystals. Sharing a similar lattice structure with Ca_2RuO_4, La_2NiO_4 also demonstrates a non-destructive reversible resistive switching at room temperature. A combination of 2- and 3-probe resistivity measurements unambiguously demonstrated that the resistive switching is associated with the interfaces between the La_2NiO_4 crystal and silver-paste contact electrodes, with negligible contribution from the bulk of the crystal's material. The wide range of observed resistance values of such contacts – from 10 to 80 kΩ – elucidates the tunneling nature of such contacts. Our experiments with an ultra-sensitive capacitive displacement meter attempted for the first time to monitor directly the field-induced lattice distortions previously proposed to be at the origin of the resistive switching. We have observed that the crystal lattice contraction/expansion accompanies the resistive switching. We also noted that the general shape of the observed displacement curves is qualitatively similar to the Joule heating generated in the sample by the dc current. This similarity provides a new insight into the origin of lattice distortions/resistive switching in La_2NiO_4 and other transition metal oxides.

3.1 INTRODUCTION

Transition metal oxides (TMO) offer rich transport phenomena and have continuously been the research focuses in condensed matter physics. Recently as antiferromagnetic spintronics emerges, antiferromagnetic TMOs have been brought up and researched in a new background. For example, canted layered perovskite iridates Sr_2IrO_4 and $Sr_3Ir_2O_7$ demonstrate their potential application in antiferromagnetic applications. One of the previous chapters has also covered spin-hall related research on Sr_2IrO_4. As also being antiferromagnetic layered perovskites, research efforts have been put into Ca_2RuO_4 and La_2NiO_4 following the same direction.

On the other hand, resistive switching emerges as an important phenomenon due to its potential in non-volatile memory applications. Many TMOs show resistive switching [1], including $Sr_3Ir_2O_7$ [2], Ca_2RuO_4 [3] and La_2NiO_4. But details of their switching are different: in $Sr_3Ir_2O_7$, resistive switching is at liquid nitrogen temperature and unipolar, which means resistance can be switched with single-polarity bias. It has also been shown that $Sr_3Ir_2O_7$ switching gets suppressed by microwave fields. While in Cr doped Ca_2RuO_4, previous chapter has shown that resistive switching happens at room temperature and is bi-polar, which requires both positive and negative biases to switch/restore resistance. This switching is not suppressed by microwaves. Resistive switching in La_2NiO_4 system is similar to what have been found in Cr doped Ca_2RuO_4 system.

In previous chapter, resistive switching in Cr doped Ca_2RuO_4 is tentatively attributed to electric-field induced lattice distortion which accompany impurity induced Mott insulator metal transition. With high precision displacement measurement tool, it is possible to monitor lattice distortion along crystal c-axis. Luckily such displacement was observed during this experiment and the displacement data can be associated with resistance data. However, it also brings questions whether this distortion is solely driven

by electric fields, since correlations between Joule heating and displacement data are also present. Since Joule heating is also induced by currents/electric-fields, so more precisely, the question becomes in what manner electric fields influence impurity induced Mott transition in La_2NiO_4 and Cr doped Ca_2RuO_4.

3.2 SAMPLES AND EXPERIMENTAL SETUP

Experiment set-up involves La_2NiO_4 sample preparation, conducting contacts preparation and measuring circuits (transport and displacement measurement) set-up.

3.2.1 La_2NiO_4 Sample and Preparation

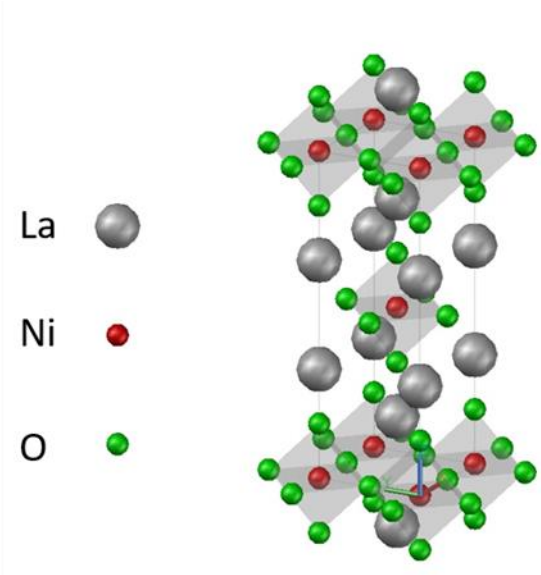

Fig. 4.1 Simplified Lattice Structure of La_2NiO_4

La_2NiO_4 belongs to 3d transition metal oxides. Fig. 4.1 shows lattice structure of La_2NiO_4: oxygen atoms form an octahedra centered at nickel atoms and these octahedron form layers with lanthanum atoms and extra octahedra in between; in real crystal, the lattice would get rotated and tilted, thus Fig 4.1 is a simplified illustration. At room temperature, La_2NiO_4 is antiferromagnetically ordered; its Néel temperature is around 330K [4, 5]. La_2NiO_4 undergoes two structural transitions at about 80K and 770K [4].

Single crystals of La_2NiO_4 in this experiment are grew by both flux and floating zone techniques. Ag-paste contacts (~ 0.1 mm2) are built on sample surfaces to enable 2-, and 3-probe measurements.

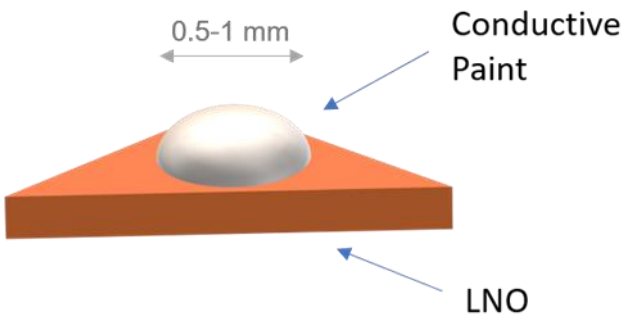

Fig. 4.2 Contacts made on La_2NiO_4 flake

3.2.2 Transport and Displacement Measurement Setup

3-probe contact geometry enables separation of interfaces and bulk material in resistance measurement. Fig. 4.3 shows one 3-probe configuration in the experiment. Here top and bottom contacts are used to drive voltage across the sample; reference contact on the side are used to read out voltage across top and bottom interface separately. Since there is no current through the reference contact, the interface at reference contact is not activated and only serves as a voltage reference point. This configuration enables observations of any interfacial phenomenon between top/bottom contact and the bulk material.

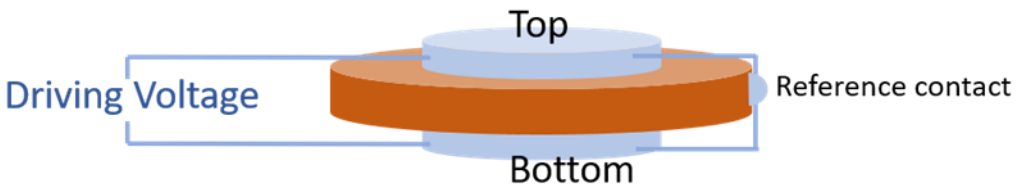

Fig. 4.3 3-probe configuration of resistance measurements

Displacement measurement set-up is shown in Fig. 4.4. Two Ag-paste contacts were built on top and bottom of the La_2NiO_4 flake and used to drive voltage along crystal c-axis. A glass plate coated with Au is fixed onto top contact. Detector head is placed above the Au-coated plate. The capacitance between the detector head and plate is measured at high precision thus enabled deduction of the distance between them. In this set-up, as voltage being driven through sample, any distortion along c-axis gets monitored

by this high precision displacement measurement set-up. The capacitance data is presented in a voltage signal to computer.

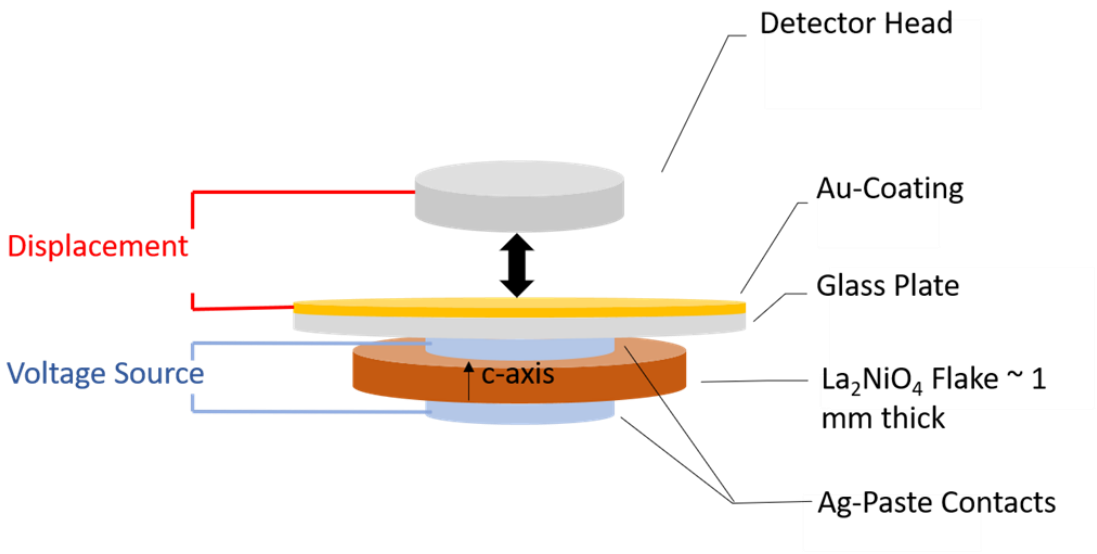

Fig. 4.4 Displacement measurement set-up

In order to provide good quality displacement data, the Au-coated plate and detector header needs to be set up carefully. First, the Au coated area of the plate should be big enough and the detector should be placed above the center of this Au coated area. This is to prevent edge effect in capacitance measurement. Second, the surface plane of detector head should be put in good parallel with the plate plane; otherwise the displacement data loses accuracy. Third, direct contact between the plate and detector head should always be avoided. Such direct contact would leave data underflow (capacitance of contacted case is always 0) and damage Au coating. Once the Au coating is damaged, it needs to be re-deposited again. While if the detector is far away from the plate, the data is always

saturated, and no change would be captured. It requires care to set up this displacement measurement tool.

In the lab, the sample is placed on an adjustable stage, which can move in horizontal plane as well as vertical direction. The detector head is installed on a tripod; by adjusting legs of the tripod, the surface plane of detector head can be tilted and vertically shifted. When the detector head is in a good parallel with and a good distance from the Au-coated plate, detector gets engaged and by adjusting sample stage, voltage reading of displacement measurement changes accordingly. It is a good practice to put the distance where displacement reading settles around half the full range.

3.3 RESULTS

3.3.1 2-probe and 3-probe I-V Characteristics

Fig 4.5 shows resistance vs. voltage curve of La_2NiO_4 at room temperature. There is hysteresis loop on this curve. Starting at around 44 Ω at low bias, resistance keeps decreasing as bias increases. With two abrupt switching (indicated by arrows), resistance enters a low resistance state. When the bias hits its maximum at positive 2.2V, resistance stays at this low resistance state around 15 Ω; until bias reduces to zero, reverses direction and hits negative 2.2V, resistance starts switching back to high resistance state. As bias hits negative maximum, resistance stays in this high state and goes back to original point. The I-V characteristics curve has a basic trend, which upon applied bias, whether positive or negative, resistance decreases; but there are clearly two resistance states that separate from each other and in Fig 4.5 (a), traces of switching can be found (indicated by turning arrows). This process is reversible and has been repeated throughout the whole experiment period. Like what have been suggested in Ca_2RuO_4 study, this resistive switching has a potential in non-volatile memory applications: if the two resistance states are used to encode information, e.g. high state for '1', low state for '0', high positive/negative voltage can be applied to switch the unit between these two states, while a low positive voltage can be used to read out current resistance value/state. The former operation can be viewed as a simplified writing mechanism; the latter reading. For a real memory device, a lot more conditions (speed, industry-level endurability, robustness) are required; La_2NiO_4 adds to the material candidate pool and offers new possibilities.

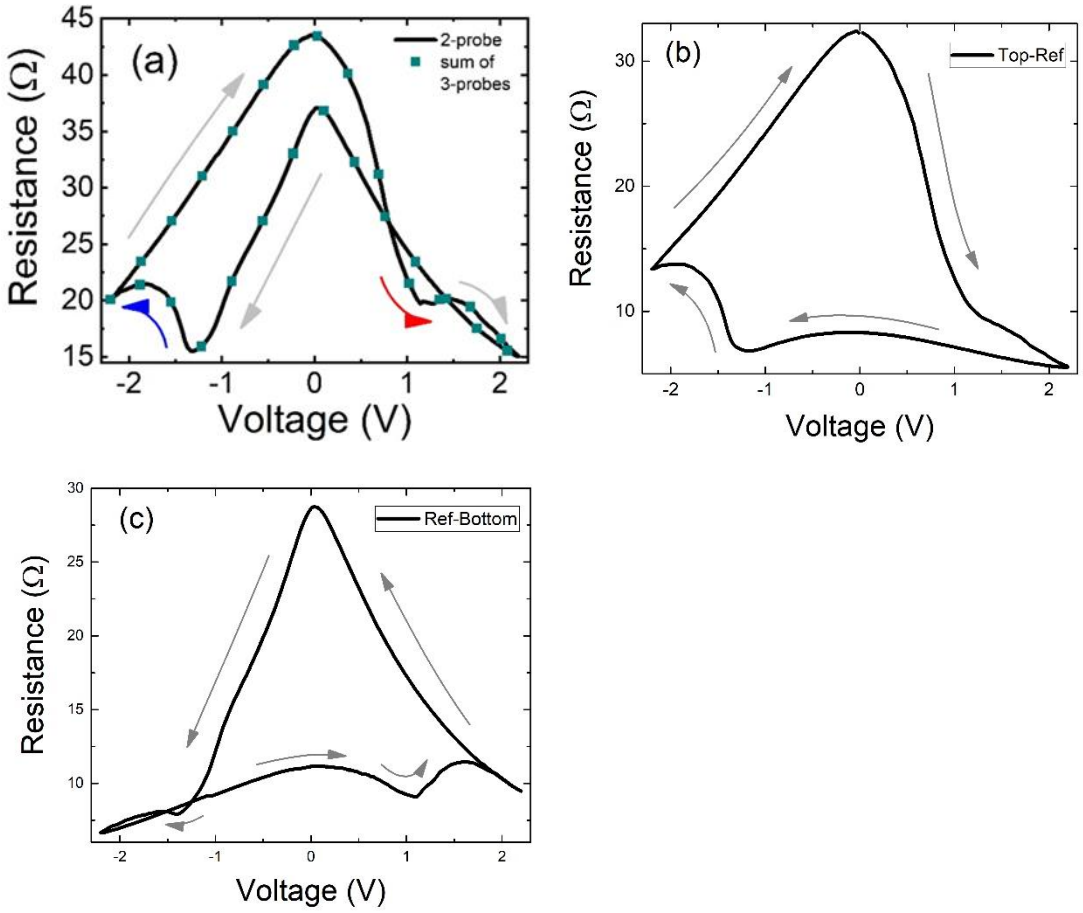

Fig. 4.5 2-probe and 3-probe I-V characteristics on sample #1.

(a) 2-probe I-V between top and bottom contacts.

(b) 3-probe I-V between top and reference contacts.

(c) 3-probe I-V between reference and bottom contacts.

In Ca_2RuO_4 switching, another issue addressed was whether the resistive switching is a bulk or interfacial effect. Here 3-probe measurements show that in La_2NiO_4, it is also true that interfaces between metal contacts and material contribute more to the resistive switching than bulk material. Fig 4.5 (b) (c) shows 3-probe I-V characteristics which

accompany 2-probe measurement in Fig 4.5 (a). In (b) and (c), resistances of the two interfaces add up to 2-probe resistance in (a) which are indicated by green dots. This is no wonder since no current goes through reference contact. Switching in these 3-probe I-V characteristics show opposite polarities: in (b) the hysteresis loop is clockwise and resistance starts from high state, switches to low state at positive bias and switches back to high state after negative bias is applied; while in (c) the hysteresis loop is anti-clockwise and resistance starts from low state, switches to high state at positive bias and switches back to low state after negative bias is applied. Those abrupt changes on 2-probe curve can also be divided and attributed to two interfaces: in (a), the first abrupt change on the positive side (arrow marked red) should come from the bottom interface while the change on the negative side (arrow marked blue) should come from the top interface.

It is understandable that interfaces would have opposite polarities/directions of the hysteresis loops if the interfaces are dominant in the switching than bulk material. When voltage is driven through top and bottom contacts, the interfaces always have opposite electric-field directions. For example, if top contact is at positive voltage, then the electric-field at top contact should be into the sample; at the same time, the bottom contact should be at negative voltage and electric-field there should be out of the sample. Thus, when voltage sweeps, two interfaces always follow opposite electric-fields. They essentially have the same type of resistance hysteresis loop. But due to opposite driving voltage, their polarities are opposite. 2-probe resistance are these 3-probe resistances added up, plus some contribution from the bulk material; but voltage is mainly kept at interfaces due to the fact the interfaces have much higher resistance than bulk material. The 2-probe polarity is decided by the interface which has ‘stronger’ switching. As one interface is going from high to low, the other low to high, the resistance summed together would follow the interface which has larger change.

3.3.2 Tunnel Junctions with La_2NiO_4 Electrodes

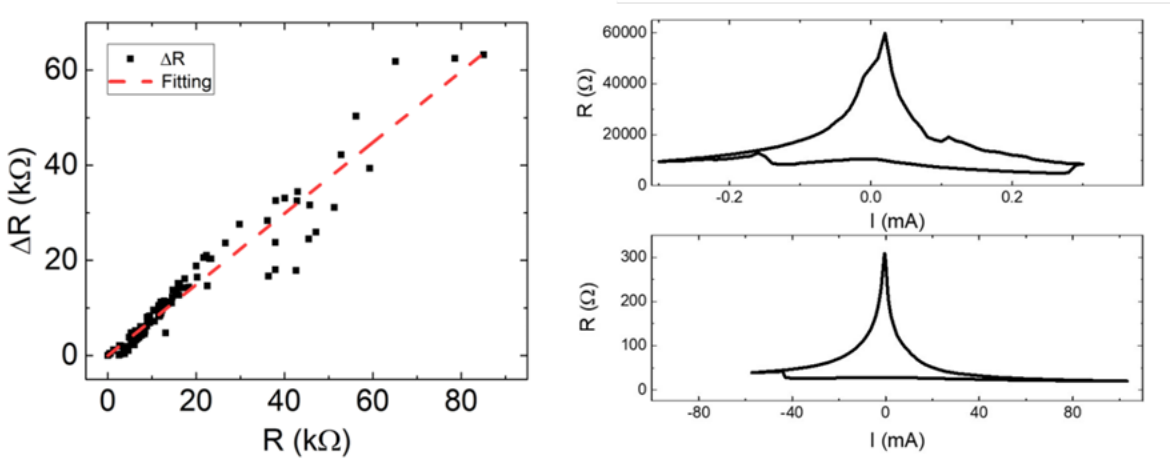

Fig. 4.6 (a) (left) Statistics of ΔR vs. R for different contacts at room temperature (b) (right) Examples of R vs. I curves for two junctions with 60,000 Ω and 300 Ω resistances in high-R state

A wide range of 2-probe resistance values are observed with different contacts on the same sample and resistive switching has been observed at different resistance levels. Fig. 4.6 (a) shows the statistics of resistance change vs. resistance values in these measurements and Fig. 4.6 (b) shows two extreme cases where resistances are very high (60000 Ω) and very low (300 Ω). This wide range of 2-probe resistance values indicate the contacts built by La_2NiO_4 electrodes are tunnel-junction-type contacts. The interface between the conductive paint and La_2NiO_4 counter electrode may serve as a natural barrier forming a planar tunnel junction. Previously such contacts have been used to study superconducting oxides [6]. We can also see that ΔR seems to be linearly dependent on R.

3.3.3 Correspondence between I-V Measurements, Displacement Measurements, and Joule Heating

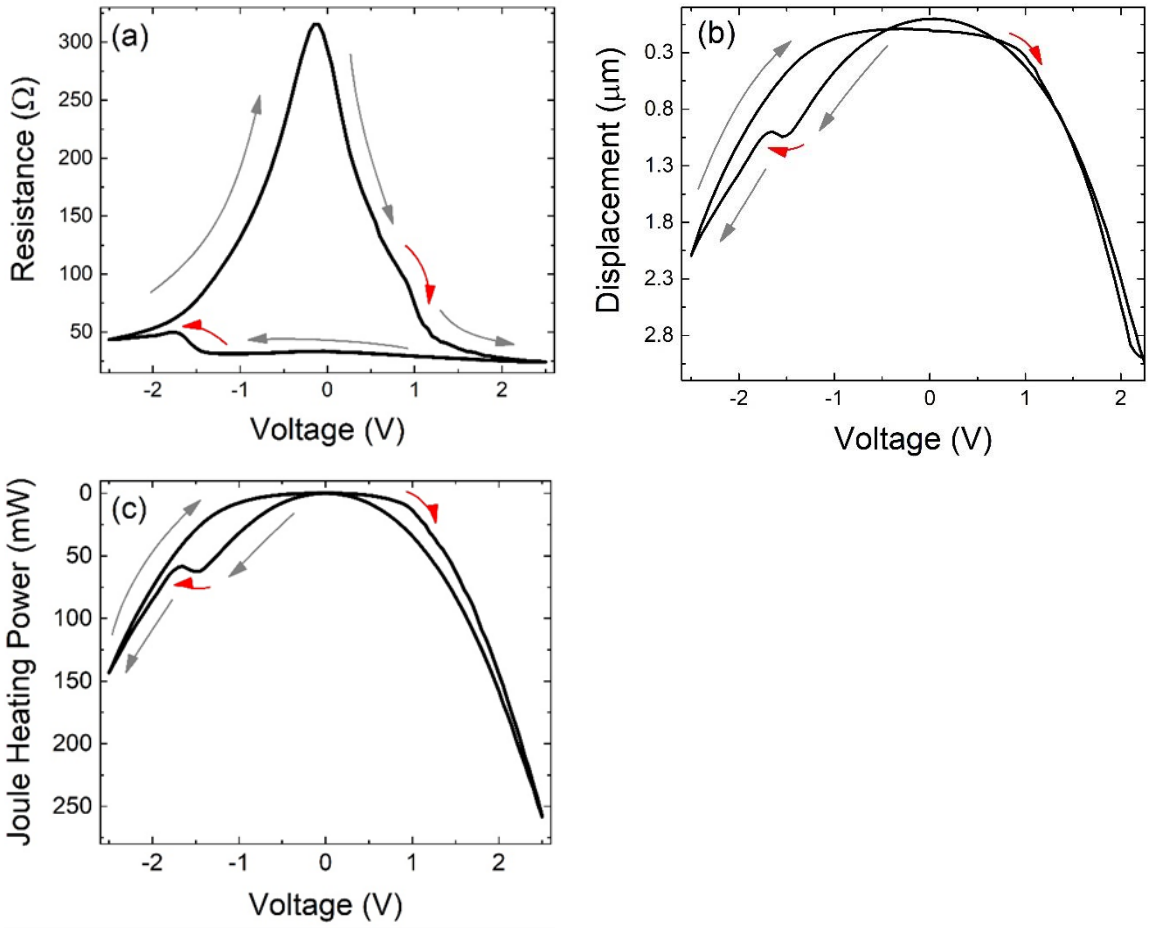

Fig. 4.7 2-probe I-V characteristics and displacement measurements on sample #2.

(a) 2-probe resistance.

(b) Displacement during the same voltage sweep in (a).

(c) Joule heat power during the same voltage sweep in (a).

Fig. 4.7 shows both I-V and displacement measurements done on sample #2. In Fig. 4.7 (a), the 2-probe I-V of sample #2 has bigger hysteresis loop and sharper ratio of high state resistance (about 300 Ω) to low state resistance (about 25 Ω). Two arrows marked red indicate abrupt resistance switching in positive bias (around 1V) and negative bias (around -1.5V). Fig. 4.7 (b) gives the associated displacement along c-axis during the same voltage sweep as (a). The displacement data tells how crystal is distorted along c-axis. There is crystal distortion under applied bias and correspondences can be established between resistance in (a) and displacement in (b): i) resistance and displacement share the same general trend, that is, upon applied biases (positive or negative), resistance tends to go down and the crystal tends to expand. This general trend can be viewed as a background of switching process. ii) detailed features can also be shared between resistance and displacement. As marked by red arrows in (a), two abrupt resistance switching at positive and negative side appear in I-V, one at +1V and the other -1.5V. There are also abrupt changes in displacement curve at same biases (marked by red in (b)). This shows that crystal expands along c-axis correspondingly during the resistive switching process.

More interestingly, Fig. 4.7 (c) shows the Joule heating power generated by current during the same sweep as in (a). Qualitatively this Joule heating power is very similar to displacement curve, including both general trends and detailed features like abrupt changes.

This poses a question that whether Joule heating is driving the crystal expansion, rather than electric-fields. Since the experiment is done in a way stable enough that thermal equilibrium believed to be established at every bias point, the Joule heating power can be viewed as a measure of heat generated at every bias point ($Q = P\Delta t$). In relatively small temperature window, both specific heat and coefficient of thermal expansion can be viewed as constant. So, in theory, a model can be built where sample expansion has a linear relation

with Joule power. But more questions arise regards to the internal mechanism driving the switching. As stated in previous chapter, in Ca_2RuO_4, resistive switching was tentatively attributed to electric-field induced lattice distortions accompany the impurity driven insulator-metal transition. There is a chance that the lattice distortion can be reflected in bulk volume change. But here is a good qualitative agreement between Joule heating and crystal expansion along c-axis. Change in Joule power should be a result of change in resistance thus crystal expansion observed maybe come after (logically, not temporally) resistance switching, which dims the chance that we are able to infer internal lattice movement from bulk volume observation.

Another possibility exists that both electric-fields and Joule heating induces crystal distortion while the former one is the driving force in resistive switching and change in the latter one is a result of resistive switching. Lattice distortion triggered by electric-fields is usually directional while thermal expansion caused by Joule heating non-directional/homogeneous. So, change in current direction doesn't cause change in Joule heating but does influence how the electric-fields interact with lattice.

Notice in Ref. 7, thermal expansion in Sr_2IrO_4 single crystals across a range of 100K is about 0.1% and the lattice distortion caused by electrical currents is ~0.8%. In our experiments of La_2NiO_4, we generally observe 1nm-2nm distortion along c-axis for 1mm-2mm flakes, which take up 0.1% to 0.5%.

3.3.4 Displacement and Joule Heating in Different Contact Geometries

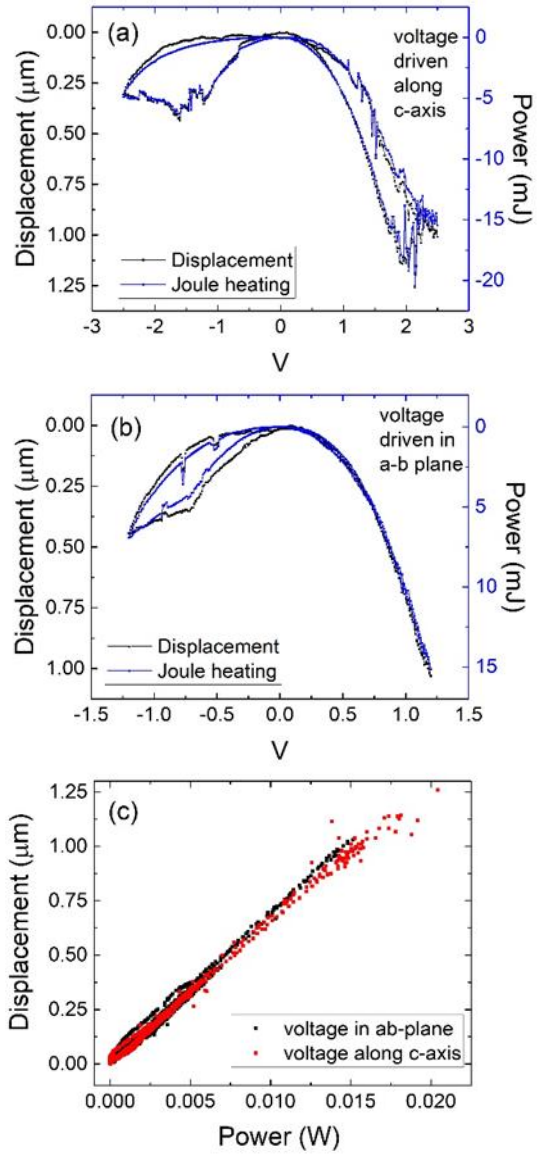

Fig. 4.8 Joule heating and displacement measurements on Sample # 3

(a) Displacement and Joule power vs. voltage when sourcing voltage along c-axis.

(b) Displacement and Joule heating power vs. voltage when sourcing voltage in ab-plane.

(c) Displacement vs Joule heating power in both geometries

Fig. 4.8 shows displacement vs. bias and Joule heating power vs. bias in two geometries: bias applied bias applied along c-axis (a) and in ab-plane (b). This is done on sample #3. The displacement is measured along c-axis all the time. This was trying to answer whether bias causes lattice distortion through electromagnetic effects. In these two geometries, electric-fields are in different directions (in ab-plane vs. perpendicular to ab-plane, e.g. along c-axis). From (a) and (b), it is shown that, in both geometries, there are small discrepancies between Joule heating power curve and displacement curve; to some extent these discrepancies can be decreased with some coefficients, but not eliminated. The residual discrepancies can be viewed as electric-fields' effects beyond Joule heating. While under the precision available in this experiment, it cannot be answered definitely that whether the beyond-Joule-heating part of effects are different in the bias geometries configured. In Fig. 4.8 (c), the scatter plot shows relation between displacement and power. The general relation is linear which indicates that Joule heating plays a significant role in displacement data; while there are also points deviated from linear relation. Those deviations may arise from experimental uncertainty, or from the mechanisms beyond Joule heating.

3.3.5 Sourcing Voltage versus Sourcing Current

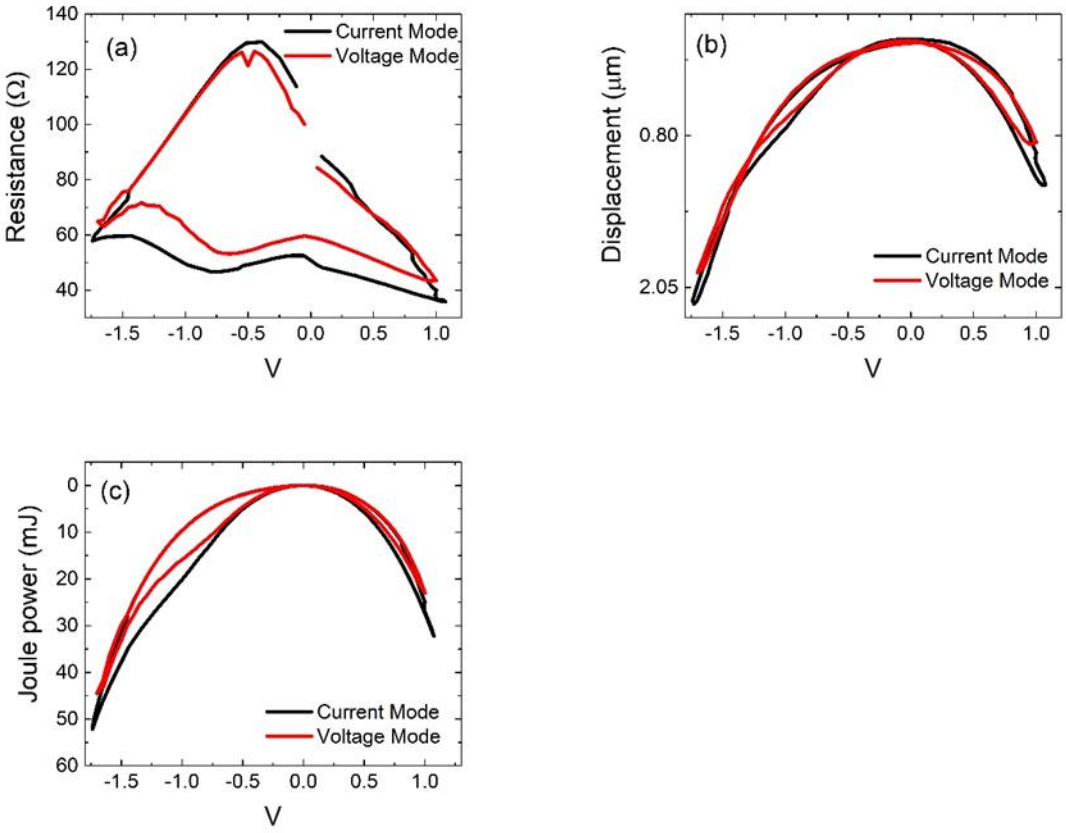

Fig. 4.9 Sourcing biases in current mode vs. in voltage mode.
(a) comparison of I-V characteristics
(b) comparison of displacement along c-axis
(c) Joule power generated during the sweep

Another question worth asking is whether it is voltage, or current that drives the resistive switching. Fig. 4.9 shows that in the resistive switching, there is no significant difference between sourcing voltage and sourcing current.

3.3.6 Statistics of ΔR vs R

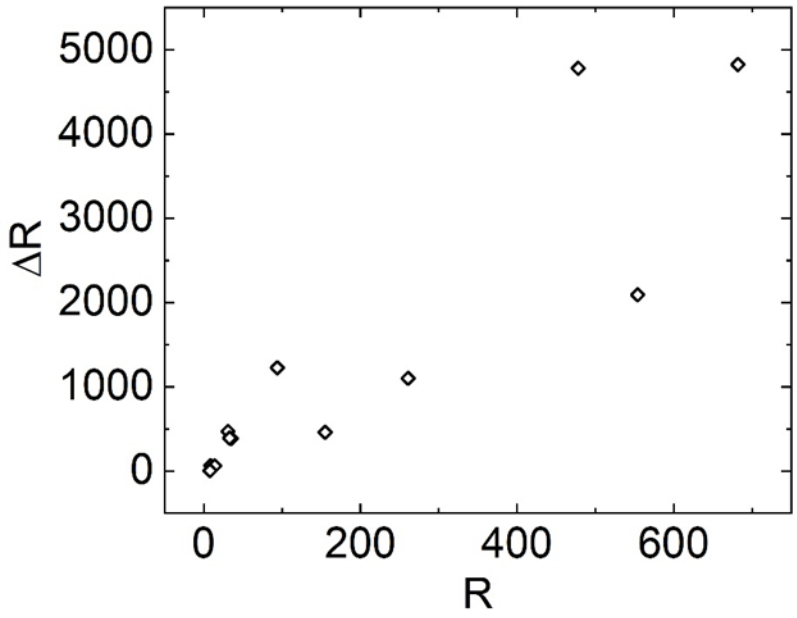

Fig. 4.10 Statistics of ΔR vs. R from 2-probe and 3-probe measurements.

Fig. 4.10 shows statistics of resistance change ΔR. Here ΔR is calculated as difference between high resistance and low resistance. High and low resistance are resistances from high and low states at low positive bias (+0.1V). This figure includes 2- and 3-probe data together. Resistive switching has been identified to be mostly from interfaces, this figure shows high resistive interfaces (3-probe) or combined (2-probe) have bigger resistance change between high and low states, or simply putting, stronger resistance switching.

3.3.7 Calibration of Displacement Measurements with a Copper Sample

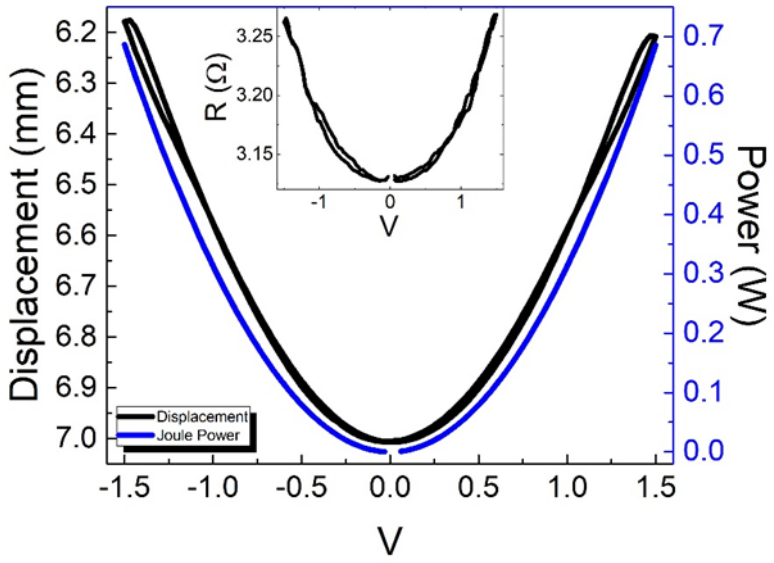

Fig. 4.11 Displacement, Joule heating, and resistance (inset) measurement on copper

We did a same measurement of a copper piece: drive bias through the copper piece and monitor the displacement of top surface of the piece. For copper, only thermal expansion induced volume change is present; thermal expansion coefficient, specific heat, resistivity and all necessary physical properties are well established. Fig. 4.11 shows the data. We can estimate the temperature change in the copper piece with two different methods for cross-validation: first is through the change of copper resistivity due to temperature. Empirical formula applies a linear approximation in relatively small temperature window around room temperature:

$$R = R_{Ref}\left[1 + \alpha\left(T - T_{Ref}\right)\right]$$

where α is a constant. Take resistance values at the highest and lowest bias, we infer the temperature change to be 11.3K. Second method uses thermal expansion. Empirical formula also applies linear approximation:

$$\frac{\Delta L}{L} = \alpha_L \Delta T$$

with α_L being coefficient of thermal expansion. This method gives us temperature change of 13.5K.

The two methods show ~16% difference with numbers in the same order of magnitude. This demonstrates that our set-up is capable of measuring volume expansion caused by Joule heating with certain accuracy.

3.4 DISCUSSION AND CONCLUSIONS

A reversible, non-destructive resistive switching is found and investigated in La_2NiO_4 single crystals at room temperature. With 3-probe I-V characteristics, the resistive switching is identified to be mostly from with interfaces between metal contacts and bulk material.

A crystal distortion along lattice c-axis is observed together with resistance change. This distortion can be connected to Joule heating generated by current. Attempts have been made to answer the question whether the displacement observed is and is purely from Joule heat generated by currents. Though no definitive answer can be extracted from the experiment, it offers data and details that may help future research.

In transition metal oxides, there are different types of resistive switching mechanism. Filament path formation and electrochemical oxygen ion migration are two major types. In Ca_2RuO_4, resistive switching has been attributed to structural transition or (tentatively) to lattice distortion accompany by impurity induced Mott transition. For La_2NiO_4, the resistive switching is less likely to be filament path type, since filament path type switching is very aggressive with sharp transitions and is usually unipolar. Both impurity driven Mott transition and oxygen ion migration can result in interfacial switching: for the former, usually there are more impurities at the interfaces; for the latter, thermal redox and anodization are also strengthened at interfaces. While in Ref. 8, structural change in Ca_2RuO_4 has been addressed and emphasized; since La_2NiO_4 shares a similar lattice structure, it seems to add weight to that La_2NiO_4 share same switching mechanism with Ca_2RuO_4. Nevertheless, it remains open to investigate the mechanism as well as other phenomena of resistive switching in La_2NiO_4.

References

[1] A. Sawa, Resistive switching in transition metal oxides, Mater. Today, 11 (2008), pp. 28-36

[2] H. Seinige, M. Williamson, S. Shen, C. Wang, G. Cao, J. Zhou, J. B. Goodenough, and M. Tsoi, Electrically tunable transport and high-frequency dynamics in antiferromagnetic Sr3Ir2O7, Phys. Rev. B 94, 214434 (2016).

[3] S. Shen, M. Williamson, G. Cao, J. Zhou, J. Goodenough, M. Tsoi, Non-destructive reversible resistive switching in Cr doped Mott insulator Ca2RuO4: Interface vs bulk effects, J. Appl. Phys. 122, 245108 (2017).

[4] Rodriguez-Carvajal, J., Fernandez-Diaz, M. T. & Martinez, J. L. Neutron diffraction study on structural and magnetic properties of La 2NiO4. J. Phys. Condens. Matter 3, 3215–3234 (1991).

[5] Nakajima, K. et al. Spin dynamics and spin correlations in the spin S=1 two-dimensional square-lattice Heisenberg antiferromagnet La2NiO4. Zeitschrift für Phys. B Condens. Matter 96, 479–489 (1995).

[6] Szabó, P., Samuely, P., Jansen, A., Marcus, J. & Wyder, P. Magnetic pair breaking in superconducting investigated by magnetotunneling. Phys. Rev. B - Condens. Matter Mater. Phys. 62, 3502–3507 (2000).

[7] Cao, G. et al. Electrical Control of Structural and Physical Properties via Strong Spin-Orbit Interactions in Sr2IrO4. Phys. Rev. Lett. 120, (2018).

[8] F. Nakamura, M. Sakaki, Y. Yamanaka, S. Tamaru, T Suzuki and Y. Maeno, Electric-field-induced metal maintained by current of the Mott insulator Ca2RuO4, Sci. Rep 3, 2536 (2013).

CHAPTER 4

A COMPARATIVE STUDY OF MAGNETORESISTANCE AND MAGNETIC STRUCTURE IN RECYCLED VS. VIRGIN NdFeB-TYPE SINTERED MAGNETS[2]

This chapter presents a comparative study on two types of NdFeB magnets: virgin and recycled. With recent development of magnet-to-magnet (m2m^{TM}) recycling technology, recycled NdFeB sintered magnets have emerged as an alternative to virgin NdFeB magnets. Recycled magnets are economically viable and environmentally friendly; moreover, they demonstrate an enhancement of magnetic and physical properties. This unanticipated enhancement in recycled NdFeB magnets may come from their unique microstructure. In our experiments we applied: (1) atomic force microscopy and magnetic force microscopy to reveal and compare the surface morphology and magnetic structure of recycled and virgin NdFeB samples; (2) bulk- and point-contact-based resistivity measurements to probe the electrical transport properties of the magnets on both macroscopic and microscopic scales.

[2] Based on *A comparative study of magnetoresistance and magnetic structure in recycled vs. virgin NdFeB-type sintered magnets, J. Magn. Magn. Mat. 442, 158-162 (2017).* As first author, Shida Shen conducted the major part of the experiments (transport measurements and AFM/MFM measurements), collected and analyzed the data, and participated in the writing and revision of the original draft.

4.1 INTRODUCTION

Neodymium magnet, or NdFeB has been the most powerful commercial magnet since its invention in 1982 [1, 2]. They are widely used in consumer electronics, electric motors, AC systems, medical devices, wind turbines and so on. Though NdFeB has been dominating the market of commercial magnets, two factors constrain wider adoption of NdFeB magnets: (i) the high price of raw materials required for their manufacture, and (ii) performance limitations. The former concern has been addressed recently with the industrial scale production of high-energy (BH_{max} ~ 396 kJ/m^3) recycled NdFeB sintered magnets via the magnet-to-magnet^{TM} process (m2m^{TM}) [3]. For the latter concern, subsequent studies have demonstrated that the m2m^{TM} processing route can produce materials whose magnetic properties and thermal stability greatly exceed those of the starting material [3–5]. This is possible because of subtle changes in composition and microstructure of recycled magnets produced by the m2m^{TM} process [5] using Grain Boundary Engineering (GBE^{TM}).

Magnetic fields have long been known to influence the electrical resistance of materials through which current is flowing, e.g. magnetoresistance (MR) effect. Applications of MR materials include the read-heads in hard disk drives [6,7] and components in ABS sensors within the automotive market. Recently, biochips exploiting MR to detect single molecule recognition events have emerged as a new application of these materials [8]. NdFeB type magnets and rE-TMs (Rare Earth-Transition Metals) based alloys display a pronounced anisotropic MR effect. The majority of published works on rE-TM films [9] deal with thin films with thickness in the range of 100 nm ~ 1 mm. It has been shown that amorphous NdFeB multi-structured, multi-layered, thin films exhibit enhanced MR values when compared with other amorphous ferromagnets [10].

4.2 SAMPLES AND EXPERIMENTAL SETUP

4.2.1 Sample Preparation

The compositions of the virgin and recycled magnets used in this study are shown in Table 4.2. The recycled magnets were produced using the m2m^{TM} processing technique in a batch size of 100 kg. The end-of-life feedstock material for m2m^{TM} recycling was derived from two different types of obsolete MRI machines. The manufacturing process to produce the recycled magnets required the feedstock magnets to be thermally demagnetized and the surface, anti-corrosion layer mechanically removed to ensure a clean, uncoated, NdFeB starting material. An additive based on the composition $Nd_6Dy_{21}Co_{19}Cu_{2.5}Fe$ alloy (GBP1) was prepared by induction melting. The GBP1 alloy was then added to waste magnets at 3 at% to achieve Grain Boundary Engineering^{TM}. The m2m^{TM} powder metallurgical processing technique and characterization were then as described in [3,4].

Cylindrical magnets (10 mm in diameter and 10 mm in height) were cut from a recycled and virgin NdFeB sintered blocks using a wire-cutting machine. The magnetic properties were then measured using a close looped permeameter (Magnet Physics EP-5) after pulse magnetizing in a field of 4T. Chemical compositions were determined by inductively coupled plasma (ICP) analyses (Agilent 5110 ICP-OES). Carbon and oxygen abundances were determined by elemental analysis. Sintered density was determined using the Archimedes principle.

4.2.2 Point-Contact Spectroscopy

Point-Contact Spectroscopy has a long history [11-13] and it is often used in characterization of surface and local transport properties, injection of electrons and probing multilayer structures [14, 15]. When contact size a is much smaller than electron mean free path l ($a \ll l$), point contacts can realize so-called ballistic transport with resistivity only dependent on contact size and independent of material and impurity; this resistance is named Sharvin resistance [11, 14]. Sharvin resistance Rs follows

$$R_s = (4\pi/3)\rho l/a^2$$

, with ρ being the material resistance. For most metals, $\rho l \sim 1$ f Ωm^2 is a similar constant, thus makes R_s depends only on contact size a. When contact size increases, a diffuse term called Maxwell Resistance, R_m, emerges. R_m follows

$$R_m = (\rho/2a)\Gamma(a/l)$$

, with the function Γ(a/l) varying from Γ (0) =1 to Γ (∞) =0.694 and it is usually taken as constant 1. As shown above, both Sharvin and Maxwell resistance can be approximated to be only dependent on contact size a. When contact size further increases and approaches the region that it is comparable to mean free path, more complicated case emerges. In this region, point contact resistance deviates from Ohm's law; the injected electrons may interact with phonons in underneath material and further leads to non-linear current-voltage characteristics [11, 13]. In this case R_s and R_m can be viewed as first and second order approximation of total resistance [14]. Point contact transport phenomena can be further enriched when magnetism is involved [14, 15]. Here, in order to characterize recycled and virgin NdFeB samples, point contacts are used in hope to detect any difference in surface transport of two type of NdFeBs. The point contacts made in this experiment are diffuse contact where Maxwell resistance dominates. It turns out that recycled and virgin NdFeB

samples do not distinguish from each other in those measurements, under various current and magnetic fields. Fig. 5.1 illustrates point contact geometry.

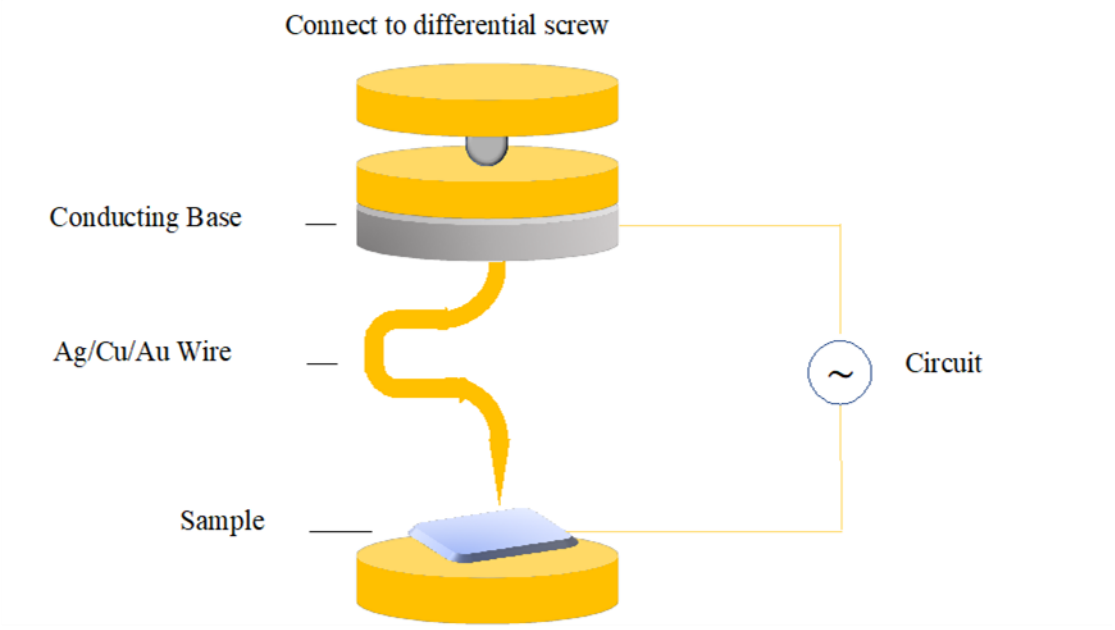

Fig. 5.1 Illustration of Point Contact configuration.

Preparation for a point contact include several steps. The wire can be made from Au, Ag, or Cu (in this case Cu). Two approaches have been proven to be able to sharpen the tip of wire to desired extent: one is through electrical-chemistry etching which gives nice, regular and sharp tips but is complicated; the other is through mechanically cut of the wire, which gives relatively nice tips and is easy to conduct. The latter approach is applied in this experiment. Specifically, a Cu wire is cut by a scissor, in a very quick manner and from a very sharp angle. Sharpness of the tip can be checked under the microscope. Next step is to solder the wire onto a metallic conducting base. Care needs to be taken since the wire is made of good thermal conducting material, over-heating can induce unpredictable deformation which blunts the tip. The tip is strengthened by bending and twisting into the shape indicated in Fig. 5.1. Then the tip along with the base is assembled on top of a

differential-screw mechanism. This mechanism consists of two parts: one is the differential screw which adjusts the total length to high accuracy level; the other is a chamber with a non-magnetic metallic ball at the center. The ball sits on the end of the differential screw. When the screw is tuned towards the chamber direction, only the metallic ball is pushed forward and passes the force forward, letting the conducting base moving forward in very little distance and bringing the conduct tip closer to the sample. For crystals and many layered samples dealt with, the surface is quite clear and under microscopy, a mirror image of the tip can be seen on the surface. This facilitates the last step of tip adjustment: tilt the tip so that it is perpendicular to sample surface; once perpendicular, the mirror image and tip itself can should form a straight line. Bring the tip further close but stop when the tip is about to hit the sample.

Now the sourcing circuit should be un-grounded and turned on. Since the tip is not hitting the sample, the circuit is still open; even with zero current sourcing, the voltage reading in voltmeter indicates open circuit (due to unavoidable fluctuation in sourcing current around zero). Turn off current source. Turn the differential screw by quarter circle or even smaller amount; turn on current source again, check if circuit is still open. If the circuit is still open, turn off current source again and turn the differential screw by a little more. Repeat the process until the circuit is closed, which indicates the tip hits the sample. This adjustment cannot be done with visual judgement because eyes are not accurate enough even under microscope and once the tip hits the sample too quickly, contact size will go beyond desired region and become a normal metal contact. More importantly, under ideal situation, a tunneling contact will be built before the tip hits sample surface, when air is tunneled through by electrons.

In this experiment, dozens of point contacts are made and tested. They are diffuse-type (Maxwell resistance) contacts.

4.3 RESULT

4.3.1. Magnetic properties and chemical composition

The results of the magnetic characterization and ICP analysis are shown in Tables 4.1 and 4.2, respectively. Four samples were then prepared: V1 and V2 from the commercial virgin magnet, and R1 and R2 from the recycled magnet produced using m2m^{TM}. The starting material was cut into rectangular blocks (1 mm * 2mm * 5 mm) along and orthogonal to the c-axis, as shown in Fig. 5.2.

Material	Grade	Br (T)	iHc (kA/m)	BH_{max} (kJ/m^3)
Virgin	N42SH	1.215	1943	285.0
Recycled	N42SH	1.289	1876	323.4
% Difference	-	6%	-3%	13%

Table 4.1: Magnetic properties at room temperature.

Sample	Virgin	Recycled
Pr (wt%)	5.26	5.85
Nd (wt%)	17.78	21.63
Dy (wt%)	4.89	4.0
Fe (wt%)	65.01	64.75
Ga (wt%)	0.09	0.10
Zr (wt%)	0.09	0.11
Al (wt%)	3.29	0.28
Co (wt%)	2.33	1.74
Cu (wt%)	0.14	0.32
B (wt%)	0.95	0.97
C (wt%)	0.08	0.12
O% (wt%)	0.09	0.13
Density (g/cm3)	7.62	7.55

Table 4.2: ICP results (+/- 0.01 wt%) of virgin magnet and recycled magnets (3 at% of GBP1 addition).

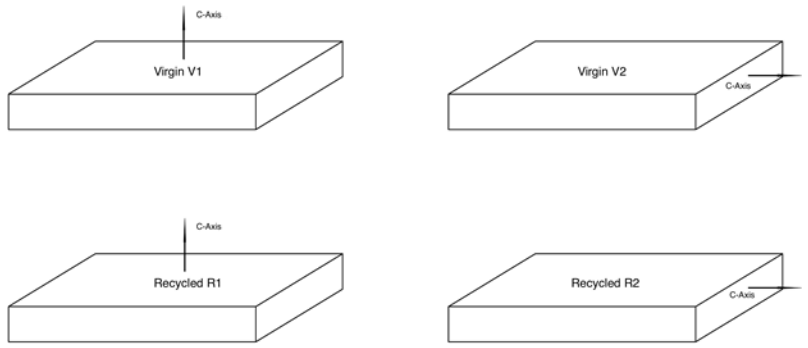

Fig. 5.2. Samples were analyzed in the configurations shown above.

4.3.2. Atomic and Magnetic Force Microscopy Characterization

Microstructural analysis of recycled magnets fabricated using the m2m^{TM} process suggest that their high coercivity may be linked to the formation of a novel grain boundary phase combined with the formation of Dy-rich shell(s) in the $Nd_2Fe_{14}B$ grains [5]. Atomic and magnetic force microscopy analyses were undertaken at room temperature with the aim to assess if microstructural changes in the bulk magnet had an effect on the magnetic structure of the sample surface. A comparison between the virgin and recycled magnets is shown in Fig 5.3. Panels (a) and (b) are atomic-force-microscopy images of the virgin and recycled magnets, respectively. Panels (c) and (d) show the corresponding magnetic-force-microscopy images for the two magnets. The atomic-force-microscopy and magnetic-force-microscopy analyses reveal very similar surface morphology and magnetic structure for the virgin and recycled samples. The images were taken on 2 mm * 5 mm faces of sample blocks and did not show any significant differences between two different sample orientations (along and orthogonal to the c-axis).

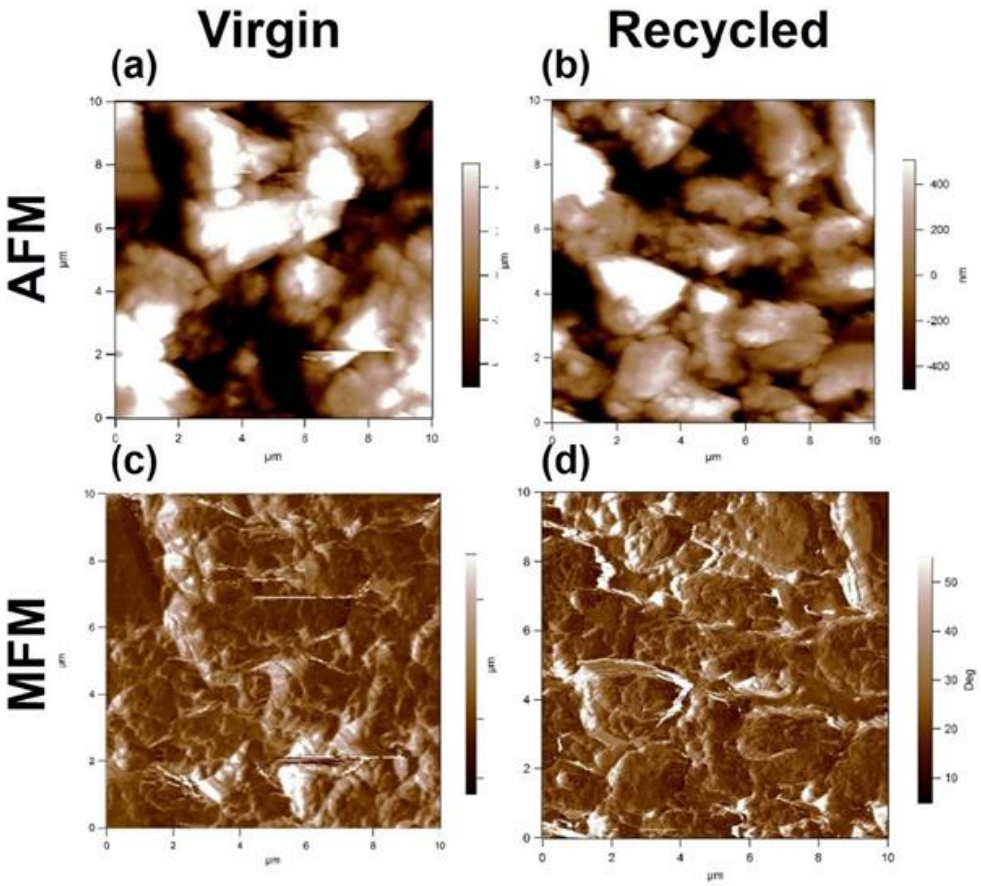

Fig. 5.3. Atomic-force-microscopy (a-b) and magnetic-force-microscopy (c-d) characterization of native (a, c) and recycled (b, d) samples.

4.3.3. Resistivity and Magnetoresistance Characterization

The resistance of the four samples (V1, V2, R1, R2) was measured at room temperature using various applied magnetic fields. Resistivity measurements were obtained using a standard 4-probe geometry with an electrical current flowing along (V2, R2) or perpendicular (V1, R1) to the c-axis of the magnets. The current (I up to 1 A) was driven along the longer side of a sample block (see Fig. 5.2) between two silver-paste contacts made on opposite (smaller) sides of the block. Two additional silver-paste contacts (2 mm apart) on the top of the sample were used as voltage (V) probes. The magnetic field (B up to 200mT) was applied along or perpendicular to the current direction. The sample resistance R = V/I was found to be independent of the current direction, orientation of magnetic field and the field magnitude in all samples. Assuming a uniform current flow between the voltage probes, the sample resistivity can be deduced from the measured sample resistance R. The only difference between the two types of magnets was a higher (by 27%) resistivity of the recycled magnets (183 μΩ*cm) compared with that of the virgin samples (144 μΩ*cm). Figs. 5.4 (a) and (b) show representative magnetoresistance R(B) traces for the native and recycled magnets, respectively. The traces are essentially horizontal (i.e., no magnetoresistance) and show a noise of the order of about 0.001%, which indicates the resolution of our measurements. Note that these measurements were performed at a relatively small current level (100 mA) to exclude any effects of Joule heating on the sample resistivity. Such a heating effect was indeed observed at higher currents (above 0.5 A) that lead to an increase of the resistivity at elevated temperatures (not shown).

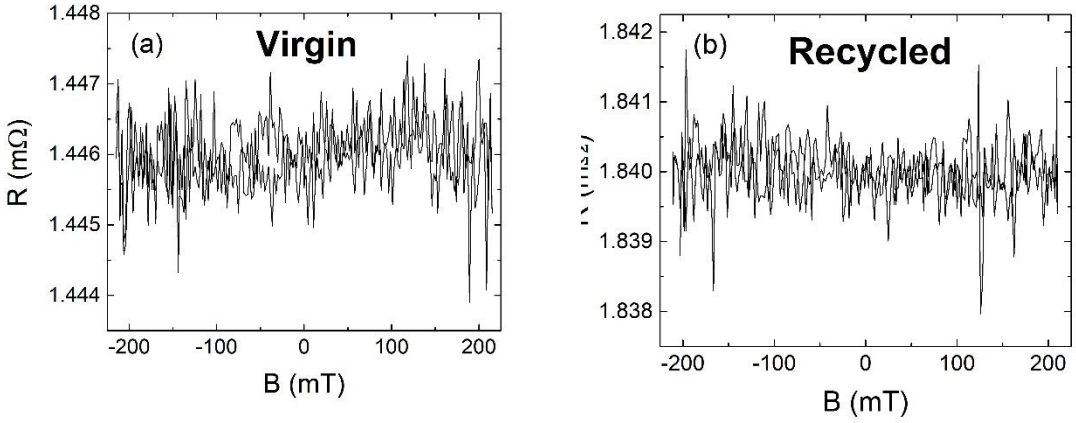

Fig. 5.4. Magnetoresistance R(B) traces for virgin (a) and recycled (b) samples.

4.3.4 Point-Contact Measurements

Point-contact measurements on both types of magnets were also performed, to assess if their magnetoresistive properties are different at microscopic scales. Point contacts between a sharpened Cu tip and the sample magnets were made with a mechanically controlled differential-screw system described previously. The contact size a can be estimated from the measured contact resistance R with a simple model for diffusive point contacts that gives R = r/2a, where r is the sample resistivity: 144 and 183 μΩ*cm for virgin and recycled magnets, respectively. When an electrical current is driven from the Cu tip into the sample, the so-called constriction resistance emanating from a small area near the contact dominates the measured resistance over other resistive contributions, including those from the bulk of the sample and the Cu tip. The measured R is, thus, defined by transport properties in the contact area and highlights the point-contact sensitivity to local transport properties on the scale of the contact size.

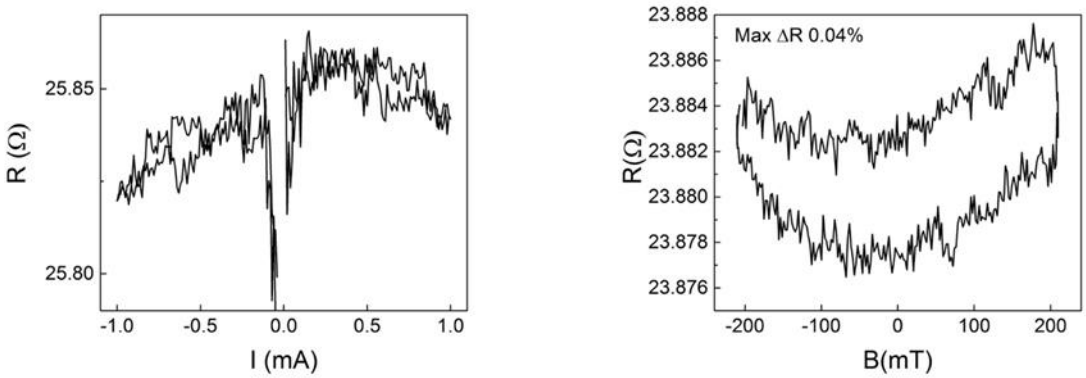

Fig. 5.5 (a) Contact size a ~ 50 nm, IV Characteristic (right) and Magnetoresistance(left)

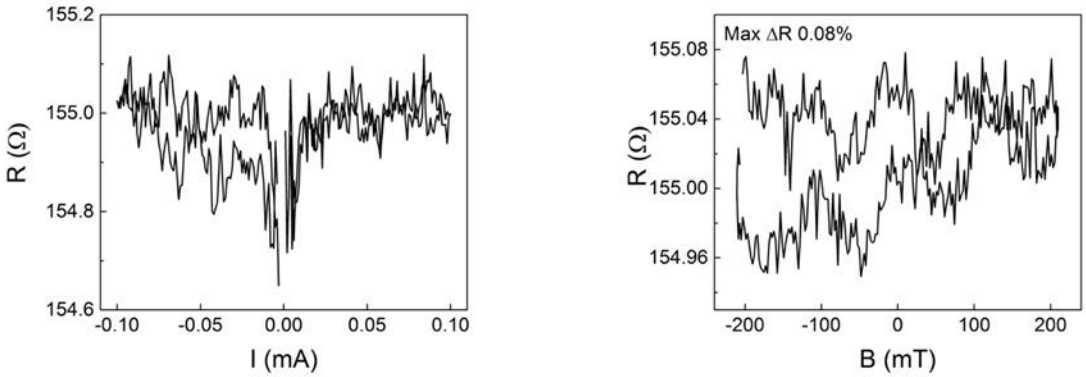

Fig. 5.5 (b) Contact size a ~ 8 nm, IV Characteristic (right) and Magnetoresistance(left)

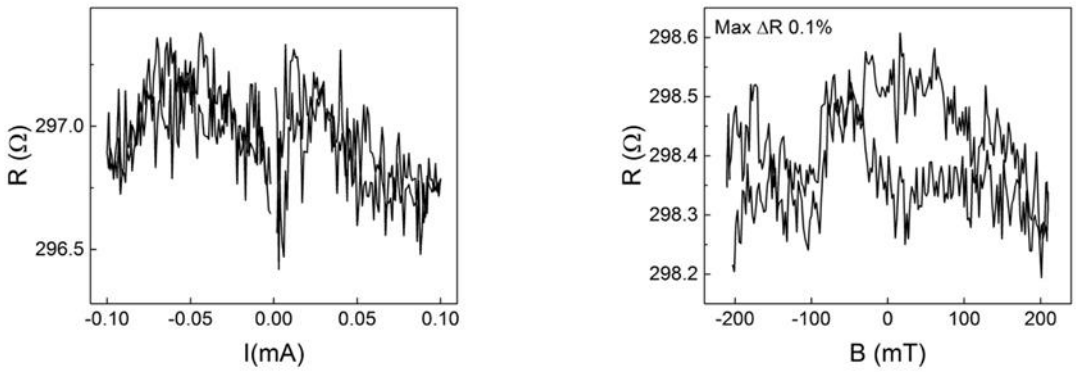

Fig. 5.5 (c) Contact size a ~ 4 nm, IV Characteristic (right) and Magnetoresistance(left)

We have tested dozens of point contacts, with sizes ranging from 4 to 500 nm, and found no magnetoresistive response. Fig. 5.5 (a), (b), (c) shows I-V characteristics and magnetoresistance of 3 contacts with size 50 nm, 8nm and 4nm. These point-contact results are similar to those of the bulk measurements (Fig. 5.4). We thus conclude that the magnetotransport properties of both types of magnets (virgin and recycled) are similar at both macro- and microscopic scales.

4.4 DISCUSSION

Atomic and magnetic force microscopy analyses and both bulk and point-contact resistivity measurements were performed on samples of recycled and virgin magnets. This work was designed to determine if the microstructural changes induced by the m2m^{TM} process would influence the magneto and electric transport properties of recycled magnets. A virgin magnet produced via conventional manufacturing was used as a reference during this study. However, no significant differences were found in magnetotransport between recycled and virgin magnets by magnetic-force-microscopy analysis (Fig. 5.3). Atomic-force-microscopy analysis did not detect any significant differences in magnetic structure either. (Fig. 5.3). Given the above, how can the almost 30% increase in the resistivity of the recycled magnets (see Fig. 5.4) be explained? Generally, resistivity values for different grades of sintered NdFeB materials are remarkably similar across a wide range of manufacturers; usually quoted between 130 and 160 μΩ*cm, with the vast majority lying at around ~150 μΩ*cm [16,17]. Indeed, this is close to the value we obtained (144 μΩ *cm) for the virgin magnet used in our study. At first sight, this lack of variation in resistivity over a wide range of compositions is surprising given that commercial NdFeBs are often doped with substantial and varying amounts of elements, such as Co, Cu, Al as well as Dy and Tb. It does however suggest that changing the bulk composition of NdFeBs alone produces only minor changes in resistivity. Indeed in the study reported herein, there was only one substantial compositional difference between the virgin and recycled magnets examined; aluminum was at 3.28% in virgin compared to 0.29% in the recycled magnets. All other elements were substantially similar. It is unlikely that this relatively small compositional change is responsible for the observed increase in resistivity, because manufacturers omitting aluminum from their NdFeBs do not report increases in resistivity. Indeed, the only time that addition of small amounts of elements have been reported to

affect resistivity is when they were selectively diffused into the grain boundaries of preformed magnets via Hitachi's Grain Boundary Diffusion process. In that case, addition of dysprosium fluoride increased resistivity of NdFeBs by up to ten-fold to 1440 μΩ*cm) [18]. Note that this process does not substantially affect the composition of the magnetic phase. What then is impeding the flow of current through magnets made via m2m™? As mentioned above, the partitioning of elements into different phases can affect resistivity [18]. We have ruled out inhomogeneity of the recycled magnet batch described herein as a cause; the intra-sample variance of Br, Hcj, BH_{max} were found to be 3.7mT, 4.5 kA/m and 4.8 kJ/m^3 respectively. Statistical analysis of the standard deviations of these parameters for 20 separate blocks demonstrates that variation in remanence and coercivity across the entire 100 kg batch is around ~3% at the 95% confidence interval; indicating a homogenous magnet. Microstructural studies also support this conclusion [5]. It is therefore likely that partitioning of elements into different phases may be responsible for the observed increase in resistivity in recycled magnets. m2m™ has previously been shown to selectively influence the composition of the grain boundaries of recycled magnets [5], as also happens in the Hitachi process [18]. Additionally, m2m™ also produces unique microstructures not found in the Hitachi process [5]. Thus, although the overall composition of elements in the virgin and recycled magnets reported herein is very similar, it is likely that their partitioning into the magnetic and grain boundary phases is very different. This may account for the observed current impedance in the present work.

References

[1] Y. Kaneko et al., Proven technologies on high-performance Nd–Fe–B sintered magnets, J. Alloy. Compd. 408–412 (2006) 1344–1349.

[2] M. Sagawa et al., New material for permanent magnets on a base of Nd and Fe, J. Appl. Phys. 55 (6) (1984).

[3] M. Zakotnik et al., Commercial-scale recycling of NdFeB-type magnets with grain boundary modification yields products with 'designer properties' that exceed those of starting materials, Waste Manage. 44 (2015) 48–54.

[4] D. Prosperi et al., Thermal stability of recycled NdFeB sintered magnets produced by Grain Boundary Modification, in: 24th International Workshop on REPM, 2016.

[5] A. Sepehri et al., Microstructure and magnetic properties of grain boundary modified recycled Nd-Fe-B sintered magnets, J. Alloy. Compd. 694 (2017) 175–184.

[6] J.M. Daughton, G.M.R. applications, J. Magn. Magn. Mater. 192 (1999) 334–342.

[7] T. McGuire et al., Anisotropic magnetoresistance in ferromagnetic 3d alloys, IEEE Trans. Magn. MAG11 (4) (1975) 1018–1038.

[8] P.P. Freitas et al., Magnetoresistive sensors, J. Phys. Condens. Matter 19 (2007) 165221.

[9] A. Walther et al., Structural, magnetic, and mechanical properties of 5 lm thick SmCo films suitable for use in microelectromechanical systems, J. Appl. Phys. 103 (2008).

[10] G. Peral et al., Magnetoresistance in amorphous NdFeB/FeB compositionally modulated multilayers, J. Appl. Phys. 69 (1991).

[11] Yu. V. Sharvin, A Possible Method for Studying Fermi Surfaces, JETP, Vol. 21, No. 3, p. 655 (September 1965)

[12] I. K. Yanson, Nonlinear effects in the electric conductivity of point junctions and electron-phonon interaction in normal metals, JETP, Vol. 39, No. 3, p. 506 (September 1974)

[13] A G M Jansen et al., Point-contact spectroscopy in metals, J. Phys. C: Solid State Phys. 13 6073 (1980)

[14] M. Tsoi et al., Search for point-contact giant magnetoresistance in Co/Cu multilayers, J. Appl. Phys. 81, 5530 (1997)

[15] M. Tsoi et al., Excitation of a magnetic multilayer by an electric current, Phys. Rev. Lett. 80 (1998) 4281.

[16] W. Wu et al., Modelling of eddy current losses in a surface mounted NdFeB permanent magnet generator, in: Proceedings of the Seventeenth International Workshop on Rare-earth Magnets and Applications, Newark, Delaware, USA, 18-22 August 2002, p323.

[17] M. Popescu et al., Study of the Thermal Aspects in Brushless Permanent Magnet Machines Performance, in: IEEE Workshop on Electrical Machines Design Control and Diagnosis (WEMDCD), 2013, pp. 60.

[18] M. Komuro et al., High electrical resistance hot pressed NdFeB magnets for low loss motors, Appl. Phys. Lett. 91 (2007) 102503

CONCLUSIONS

A series of transition-metal-oxide (TMO) antiferromagnets, including both TMO single crystals and heterostructures, have been studied in the context of searching for potential applications in antiferromagnetic spintronics and for non-volatile memory applications. The presented studies describe experimental investigations of transport properties of 3d (La_2NiO_4), 4d (Ca_2RuO_4) and 5d (Sr_2IrO_4) TMOs. In chapter 1, magnetoresistance and microwave response of Pt/Sr_2IrO_4 double-layer heterostructures was examined. Here the Pt layer was used to mediate the spin injection from Pt into Sr_2IrO_4 via the spin Hall effect in Pt. We have found that the spin injection changes the magnetoresistance of Sr_2IrO_4. In chapter 2, Cr doped Ca_2RuO_4 crystals were found to exhibit a non-destructive reversible resistive switching at room temperature. An applied electrical bias was shown to reduce the dc resistance of Ca_2RuO_4 crystals by as much as 75%; the original resistance of the sample could be restored by applying an electrical bias of opposite polarity. Results of transport measurements in 2-, 3-, and 4-probe geometries suggested that the resistive switching is mostly an interfacial effect. Temperature-dependent resistivity measurements with Ca_2RuO_4 crystals showed that the activation energy of this material can be tuned by an applied dc electrical bias. In Chapter 3, a similar non-destructive and bipolar resistive switching was also observed at room-temperature in La_2NiO_4 single crystals. It was also identified by 2-, 3- and 4-porbe measurements as essentially an interfacial resistance effect which occurs at the sample/contact probe interfaces. The wide range of observed contact-resistance values from 10 to 80 kΩ confirmed the tunneling nature of the contacts to La_2NiO_4. The resistive switching in our TMOs was tentatively associated with electric-field induced distortions of TMO lattice. We have made an attempt to probe such distortions directly in experiments with a

capacitive displacement meter. The displacement measurements done on La_2NiO_4 samples provided information about crystal distortions, although further studies are still needed to separate thermal expansion caused by Joule heating from lattice distortion caused by electrical fields. Future resistive-switching memory applications may potentially make use of the switching observed in Ca_2RuO_4 and La_2NiO_4. Finally, chapter 4 presents a comparative study between virgin and recycled NdFeB magnets. Recycled NdFeB magnets show enhancement in resistivity. With combined application of atomic force microscopy, magnetic force microscopy and point-contact spectroscopy, virgin and recycled NdFeB magnets were shown to be very similar in surface morphology, magnetic structure and magnetotransport properties. Our results support the usage of the recycled materials in place of the virgin ones.

There are similarities as well as differences in properties of the TMO antiferromagnets studied. Resistive switching has been observed in Sr_2IrO_4, Cr doped Ca_2RuO_4 and La_2NiO_4. However, for Cr doped Ca_2RuO_4 and La_2NiO_4, resistive switching happens at room temperature and is bipolar. It requires both positive and negative biases to finish a full switching cycle, e.g. switching from high resistance state to low state and back. The switching has a large resistance ratio (high resistance value over low resistance value) and only requires an electrical bias of <1V (with sample dimension ~1mm). In both TMOs, resistive switching has been identified to originate essentially from the interfaces between contacts and bulk sample. While for Sr_2IrO_4, as well as for its sister compound $Sr_3Ir_2O_7$, the resistive switching is unipolar and was observed only at liquid nitrogen temperature. The resistive switching in Sr_2IrO_4 only requires biases of the same polarity to switch from high resistance state to low state and back. In contrast, the resistive switching observed in Cr doped Ca_2RuO_4, La_2NiO_4 and Pt/Sr_2IrO_4 double-layer heterostructures is reversible and non-destructive and was observed at different temperatures up to room

temperature. Another similarity comes from the tunable activation energy observed in both Ca_2RuO_4 and Sr_2IrO_4 (as well as $Sr_3Ir_2O_7$). Unlike traditional semiconductors that have fixed band-gaps, the activation energy of Sr_2IrO_4 and Cr doped Ca_2RuO_4 both show a dependence on the applied electrical bias. This electrically tunable transport property is attributed to electric-field-induced lattice dynamics and offers a new method for controlling semiconductors' properties.

Different experimental techniques have been applied and tested in these studies. The displacement measurement set-up based on capacitance meter has been shown to provide measurements of crystal dimensions on the nanometer scale. It has also been calibrated in thermal-expansion experiments with a bulk copper sample. It has been shown that tunneling-junction-type contacts can be made to La_2NiO_4 single crystals, as opposed to conventional methods, which typically involve a thin film deposition.

The studied TMOs can be candidates for future resistive-switching-based and magnetism-based non-volatile memory applications. The non-destructive feature and large high/low resistance ratio of Ca_2RuO_4 and La_2NiO_4 can be very helpful for building robust, multi-level switching schemes. Bias-dependent activation energy observed in Ca_2RuO_4 indicates a possible way for building electrically-tunable semiconductors. In the future, transport properties of TMO antiferromagnets would be essential for interconnecting spintronics and electronics. Hopefully the presented studies have provided useful information for next generation memory applications and beyond.

Appendix

LIST OF PUBLICATIONS

Shida Shen, Morgan Williamson, Gang Cao, Jianshi Zhou, and Maxim Tsoi. Resistive switching in tunnel junctions with a single-crystal La2NiO4 electrode. **Under review**.

Morgan Williamson, Shida Shen, Gang Cao, Jianshi Zhou, John B. Goodenough, and Maxim Tsoi. Exploring the energy landscape of resistive switching in antiferromagnetic Sr3Ir2O7. **Phys. Rev. B 97, 134431, 2018**.

Kristy J. Kormondy, Lingyuan Gao, Xiang Li, Sirong Lu, Agham B. Posadas, Shida Shen, Maxim Tsoi, Martha R. McCartney, David J. Smith, Jianshi Zhou, Leonid L. Lev, Marius-Adrian Husanu, Vladimir N. Strocov, and Alexander A. Demkov. Giant magnetoresistance in the two-dimensional electron system at the ferromagnet/perovskite interface. **Scientific Report, 8:7721, 2018.**

Shida Shen, Morgan Williamson, Gang Cao, Jianshi Zhou, John Goodenough, and Maxim Tsoi. Non-destructive reversible resistive switching in Cr doped mott insulator Ca2RuO4: Interface vs bulk effects. **Journal of Applied Physics, 122(24):245108, 2017.**

Shida Shen, Morgan C. Williamson, Gang Cao, Jianshi Zhou, John Goodenough, and Maxim Tsoi. Electrically tunable transport and resistive switching in Cr doped Ca2RuO4. **SRC TECHCON 2017, (P091323), 2017.**

Shida Shen, Maxim Tsoi, Davide Prosperi, Catalina O Tudor, Stephen K Dove, Alex I. Bevan, Gojmir Furlan, and Miha Zakotnik. A comparative study of magnetoresistance and magnetic structure in recycled vs. virgin ndfeb-type sintered magnets. **Journal of Magnetism and Magnetic Materials, 442:158 – 162, 2017.**

Heidi Seinige, Morgan Williamson, Shida Shen, Cheng Wang, Gang Cao, Jianshi Zhou, John B. Goodenough, and Maxim Tsoi. Electrically tunable transport and high-frequency dynamics in antiferromagnetic Sr3Ir2O7. **Phys. Rev. B, 94:214434, 2016.**

LIST OF PRESENTATIONS

03/2019 Talk: Resistive switching in tunnel junctions with a single-crystal La2NiO4 electrode, **APS March Meeting 2019**, Boston, MA.

03/2018 Talk: Probing Lattice Distortions Associated with Resistive Switching in La2NiO4, **APS March Meeting 2018**, Los Angeles, CA.

09/2017 Poster Session: Electrically Tunable Transport and Resistive Switching in Antiferromagnetic Ca2RuO4 and La2NiO4, **C-SPIN Annual Review**.

09/2017 Talk and Poster: Electrically Tunable Transport and Resistive Switching in Cr Doped Ca2RuO4, **TECHCON 2017**, Austin, TX.

03/2017 Talk: Electrically tunable transport and resistive switching in doped Ca2RuO4, **APS March Meeting 2017**, New Orleans, LA.

References

INTRODUCTION

[1] Sawa, A. Resistive switching in transisiton metal oxides. Mater. Today 11, 28–36 (2008).

[2] Lee, P. A., Nagaosa, N. & Wen, X.-G. Doping a Mott insulator: Physics of high-temperature superconductivity. Rev. Mod. Phys. 78, 17–85 (2006).

[3] Baltz, V. et al. Antiferromagnetic spintronics. Rev. Mod. Phys. 90, 15005 (2018).

[4] Jungwirth, T., Marti, X., Wadley, P. & Wunderlich, J. Antiferromagnetic spintronics. Nat. Nanotechnol. 11, 231 (2016).

[5] Meijer, G. I. Who Wins the Nonvolatile Memory Race? Science (80-.). 319, 1625 LP-1626 (2008).

[6] Wang, C. et al. Anisotropic magnetoresistance in antiferromagnetic Sr2IrO4. Phys. Rev. X 4, (2014).

[7] Wang, C. et al. Electrically tunable transport in the antiferromagnetic Mott insulator Sr2IrO4. Phys. Rev. B 92, 115136 (2015).

[8] Seinige, H. et al. Electrically tunable transport and high-frequency dynamics in antiferromagnetic Sr3Ir2O7. Phys. Rev. B 94, 214434 (2016).

CHAPTER 1

[1] Gang Cao and Pedro Schlottmann, The challenge of spin–orbit-tuned ground states in iridates: a key issues review, Rep. Prog. Phys. 81 042502 (2018)

[2] Zhao L, Torchinsky D H, Chu H, Ivanov V, Lifshitz R, Flint R, Qi T, Cao G and Hsieh D, Evidence of an odd-parity hidden order in a spin–orbit coupled correlated iridate Nat. Phys. 12 32 (2016)

[3] C. Wang, H. Seinige, G. Cao, J.-S. Zhou, J. B. Goodenough, and M. Tsoi, Temperature dependence of anisotropic magnetoresistance in antiferromagnetic Sr2IrO4, J. Appl. Phys. 117, 17A310 (2015).

[4] Kim B J et al, Novel Jeff = 1/2 Mott state induced by relativistic spin–orbit coupling in Sr2IrO4 Phys. Rev. Lett. 101 076402 (2008)

[5] Boseggia S, Walker H C, Vale J, Springell R, Feng Z, Perry R S, Moretti Sala M, Rønnow H M, Collins S P and McMorrow D F, Locking of iridium magnetic moments to the correlated rotation of oxygen octahedra in Sr2IrO4 revealed by x-ray resonant scattering, J. Phys.: Condens. Matter 25 422202 IOPscience (2013)

[6] Torchinsky D H, Chu H, Zhao L, Perkins N B, Sizyuk Y, Qi T, Cao G and Hsieh D, Structural distortion-induced magnetoelastic locking in Sr2IrO4 revealed through nonlinear optical harmonic generation Phys. Rev. Lett. 114 096404 (2015)

[7] Haskel D, Fabbris G, Zhernenkov M, Kong P P, Jin C Q, Cao G and van Veenendaal M, Pressure tuning of the spin–orbit coupled ground state in Sr2IrO4 Phys. Rev. Lett. 109 027204 (2012)

[8] Serrao C R et al, Epitaxy-distorted spin–orbit Mott insulator in Sr2IrO4 thin films Phys. Rev. B 87 085121 (2013)

[9] Ge M, Qi T F, Korneta O B, De Long D E, Schlottmann P, Crummett W P and Cao G, Lattice-driven magnetoresistivity and metal-insulator transition in single-layered iridates Phys. Rev. B 84 100402 (2011)

[10] C. Wang, H. Seinige, G. Cao, J.-S. Zhou, J. B. Goodenough, and M. Tsoi, Electrically Tunable Band Gap in Antiferromagnetic Mott Insulator Sr2IrO4, Phys. Rev. B 92, 115136 (2015).

[11] C. Wang, H. Seinige, G. Cao, J.-S. Zhou, J. B. Goodenough, and M. Tsoi, Anisotropic magnetoresistance in antiferromagnetic Sr2IrO4, Phys. Rev. X 4, 041034 (2014).

[12] Liu, L., Moriyama, T., Ralph, D. C. & Buhrman, R. A. Spin-torque ferromagnetic resonance induced by the spin Hall effect. Phys. Rev. Lett. 106, (2011).

[13] Liu, L. et al. Spin-torque switching with the giant spin hall effect of tantalum. Science (80-.). 336, 555–558 (2012).

[14] Hirsch, J. E. Spin Hall Effect. Phys. Rev. Lett. 83, 1834–1837 (1999).

[15] D'Yakonov, M. I. & Perel, V. I. Possibility of Orienting Electron Spins with Current. J. Exp. Theor. Phys. Lett. 13, 467 (1971).

[16] Sinova, J. et al. Universal intrinsic spin Hall effect. Phys. Rev. Lett. 92, (2004).

[17] Liu, L., Buhrman, R. A., Ralph, D. C., Review and Analysis of Measurements of the Spin Hall Effect in Platinum, arXiv:1111.3702 (2011)

[18] Hao, Q., Chen, W. & Xiao, G. Beta (β) tungsten thin films: Structure, electron transport, and giant spin Hall effect. Appl. Phys. Lett. 106, (2015).

[19] Bahr, S. et al. Low-energy magnetic excitations in the spin-orbital Mott insulator Sr2IrO4. Phys. Rev. B - Condens. Matter Mater. Phys. 89, (2014).

[20] G. Cao, S. McCall, J. E. Crow, and R. P. Guertin, Observation of a Metallic Antiferromagnetic Phase and Metal to Nonmetal Transition in Ca3Ru2O7, Phys. Rev. Lett. 78, 1751 (1997).

[21] H. Seinige, M. Williamson, S. Shen, C. Wang, G. Cao, J. Zhou, J. B. Goodenough, and M. Tsoi, Electrically tunable transport and high-frequency dynamics in antiferromagnetic Sr3Ir2O7, Phys. Rev. B 94, 214434 (2016).

CHAPTER 2

[1] J. B. Oostinga, H. B. Heersche, X. Liu, A. F. Morpurgo, and L. M. K. Vandersypen, Gate-induced insulating state in bilayer graphene devices, Nat. Mater. 7, 151 (2008).

[2] Y. Zhang, T.-T. Tang, C. Girit, Z. Hao, M. C. Martin, A. Zettl, M. F. Crommie, Y. R. Shen, and F. Wang, Direct observation of a widely tunable bandgap in bilayer graphene, Nature 459, 820 (2009).

[3] E. V. Castro, K. S. Novoselov, S. V. Morozov, N. M. R. Peres, J. M. B. L. Dos Santos, J. Nilsson, F. Guinea, A. K. Geim, and A. H. C. Neto, Biased Bilayer Graphene: Semiconductor with a Gap Tunable by the Electric Field Effect, Phys. Rev. Lett. 99, 216802 (2007).

[4] C. Wang, H. Seinige, G. Cao, J.-S. Zhou, J. B. Goodenough, and M. Tsoi, Electrically tunable transport in the antiferromagnetic Mott insulator Sr2IrO4, Phys. Rev. B 92, 115136 (2015).

[5] H. Seinige, M. Williamson, S. Shen, C. Wang, G. Cao, J. Zhou, J. B. Goodenough, and M. Tsoi, Electrically tunable transport and high-frequency dynamics in antiferromagnetic Sr3Ir2O7, Phys. Rev. B 94, 214434 (2016).

[6] G. I. Meijer, Who wins the nonvolatile memory race? Science, 319, 1625 (2008).

[7] R. Waser, M. Aono, Nanoionics-based resistive switching memories, Nat. Mater 6, 833 (2007).

[8] H. Akinaga and H. Shima, Resistive Random Access Memory (ReRAM) Based on Metal Oxides, Proc. IEEE 98, 2237 (2010).

[9] G. Bersuker, D. C. Gilmer, D. Veksler, P. Kirsch, L. Vandelli, A. Padovani, L. Larcher, K. McKenna, A. Shluger, V. Iglesias, M. Porti, and M. Nafria, Metal oxide resistive memory switching mechanism based on conductive filament properties, J. Appl. Phys. 110, 124518 (2011).

[10] H. S. P. Wong, H. Y. Lee, S. Yu, Y. S. Chen, Y. Wu, P. S. Chen, B. Lee, F. T. Chen, and M. J. Tsai, Metal–Oxide RRAM, Proc. IEEE 100, 1951 (2012).

[11] F. Nakamura, M. Sakaki, Y. Yamanaka, S. Tamaru, T Suzuki and Y. Maeno, Electric-field-induced metal maintained by current of the Mott insulator Ca2RuO4, Sci. Rep 3, 2536 (2013).

[12] T. F. Qi, O. B. Korneta, S. Parkin, L. E. DeLong, P. Schlottmann and G. Cao, Single-Crystal Ca2Ru1-xCrxO4, Phys. Rev. Lett. 105, 177203 (2010).

[13] M. Braden, G. André, S. Nakatsuji, and Y. Maeno, Crystal and magnetic structure of Ca2RuO4: Magnetoelastic coupling and the metal-insulator transition, Phys. Rev. B 58, 847 (1998).

[14] G. Cao, S. McCall, M. Shepard, J.E. Crow and R.P. Guertin, Magnetic and Transport Properties of Single Crystal Ca2RuO4: Relationship to Superconducting Sr2RuO4, Phys. Rev. B 56, R2916 (1997).

[15] C. S. Alexander, G. Cao, V. Dobrosavljevic, E. Lochner, S. McCall, J. E. Crow and P. R. Guertin, Destruction of the Mott Insulating Ground State of Ca2RuO4 by a Structural Transition, Phys. Rev. B 60, R8422 (1999).

[16] O. Friedt, M. Braden, G. André, P. Adelmann, S. Nakatsuji, and Y. Maeno, Structural and magnetic aspects of themetal-insulator transition in Ca2-xSrxRuO4. Phys. Rev. B 63, 174432 (2001).

[17] P. Steffens, O. Friedt, P. Alireza, W. G. Marshall, W. Schmidt, F. Nakamura, S. Nakatsuji, Y. Maeno, R. Lengsdorf, M. M. Abd-Elmeguid, and M. Braden, High-pressure diffraction studies on Ca2RuO4. Phys. Rev. B 72, 094104 (2005).

[18] H.-T. Kim, B.-G. Chae, D.-H. Youn, S.-L. Maeng, G. Kim, K.-Y. Kang, and Y.-S. Lim, Mechanism and observation of Mott transition in VO2-based two- and three-terminal devices. New J. Phys. 6, 52 (2004).

[19] H.-T. Kim, M. Kim, A. Sohn, T. Slusar, G. Seo, H. Cheong, and D.-W. Kim, Photoheat-induced Schottky nanojunction and indirect Mott transition in VO2: photocurrent analysis. J. Phys.:Condens. Matter 28, 085602 (2016).

CHAPTER 3

[1] A. Sawa, Resistive switching in transition metal oxides, Mater. Today, 11 (2008), pp. 28-36

[2] H. Seinige, M. Williamson, S. Shen, C. Wang, G. Cao, J. Zhou, J. B. Goodenough, and M. Tsoi, Electrically tunable transport and high-frequency dynamics in antiferromagnetic Sr3Ir2O7, Phys. Rev. B 94, 214434 (2016).

[3] S. Shen, M. Williamson, G. Cao, J. Zhou, J. Goodenough, M. Tsoi, Non-destructive reversible resistive switching in Cr doped Mott insulator Ca2RuO4: Interface vs bulk effects, J. Appl. Phys. 122, 245108 (2017).

[4] Rodriguez-Carvajal, J., Fernandez-Diaz, M. T. & Martinez, J. L. Neutron diffraction study on structural and magnetic properties of La 2NiO4. J. Phys. Condens. Matter 3, 3215–3234 (1991).

[5] Nakajima, K. et al. Spin dynamics and spin correlations in the spin S=1 two-dimensional square-lattice Heisenberg antiferromagnet La2NiO4. Zeitschrift für Phys. B Condens. Matter 96, 479–489 (1995).

[6] Szabó, P., Samuely, P., Jansen, A., Marcus, J. & Wyder, P. Magnetic pair breaking in superconducting investigated by magnetotunneling. Phys. Rev. B - Condens. Matter Mater. Phys. 62, 3502–3507 (2000).

[7] Cao, G. et al. Electrical Control of Structural and Physical Properties via Strong Spin-Orbit Interactions in Sr2IrO4. Phys. Rev. Lett. 120, (2018).

[8] F. Nakamura, M. Sakaki, Y. Yamanaka, S. Tamaru, T Suzuki and Y. Maeno, Electric-field-induced metal maintained by current of the Mott insulator Ca2RuO4, Sci. Rep 3, 2536 (2013).

CHAPTER 4

[1] Y. Kaneko et al., Proven technologies on high-performance Nd–Fe–B sintered magnets, J. Alloy. Compd. 408–412 (2006) 1344–1349.

[2] M. Sagawa et al., New material for permanent magnets on a base of Nd and Fe, J. Appl. Phys. 55 (6) (1984).

[3] M. Zakotnik et al., Commercial-scale recycling of NdFeB-type magnets with grain boundary modification yields products with 'designer properties' that exceed those of starting materials, Waste Manage. 44 (2015) 48–54.

[4] D. Prosperi et al., Thermal stability of recycled NdFeB sintered magnets produced by Grain Boundary Modification, in: 24th International Workshop on REPM, 2016.

[5] A. Sepehri et al., Microstructure and magnetic properties of grain boundary modified recycled Nd-Fe-B sintered magnets, J. Alloy. Compd. 694 (2017) 175–184.

[6] J.M. Daughton, G.M.R. applications, J. Magn. Magn. Mater. 192 (1999) 334–342.

[7] T. McGuire et al., Anisotropic magnetoresistance in ferromagnetic 3d alloys, IEEE Trans. Magn. MAG11 (4) (1975) 1018–1038.

[8] P.P. Freitas et al., Magnetoresistive sensors, J. Phys. Condens. Matter 19 (2007) 165221.

[9] A. Walther et al., Structural, magnetic, and mechanical properties of 5 lm thick SmCo films suitable for use in microelectromechanical systems, J. Appl. Phys. 103 (2008).

[10] G. Peral et al., Magnetoresistance in amorphous NdFeB/FeB compositionally modulated multilayers, J. Appl. Phys. 69 (1991).

[11] Yu. V. Sharvin, A Possible Method for Studying Fermi Surfaces, JETP, Vol. 21, No. 3, p. 655 (September 1965)

[12] I. K. Yanson, Nonlinear effects in the electric conductivity of point junctions and electron-phonon interaction in normal metals, JETP, Vol. 39, No. 3, p. 506 (September 1974)

[13] A G M Jansen et al., Point-contact spectroscopy in metals, J. Phys. C: Solid State Phys. 13 6073 (1980)

[14] M. Tsoi et al., Search for point-contact giant magnetoresistance in Co/Cu multilayers, J. Appl. Phys. 81, 5530 (1997)

[15] M. Tsoi et al., Excitation of a magnetic multilayer by an electric current, Phys. Rev. Lett. 80 (1998) 4281.

[16] W. Wu et al., Modelling of eddy current losses in a surface mounted NdFeB permanent magnet generator, in: Proceedings of the Seventeenth International Workshop on Rare-earth Magnets and Applications, Newark, Delaware, USA, 18-22 August 2002, p323.

[17] M. Popescu et al., Study of the Thermal Aspects in Brushless Permanent Magnet Machines Performance, in: IEEE Workshop on Electrical Machines Design Control and Diagnosis (WEMDCD), 2013, pp. 60.

[18] M. Komuro et al., High electrical resistance hot pressed NdFeB magnets for low loss motors, Appl. Phys. Lett. 91 (2007) 102503

Vita

Contact Information

Email: shida.shen@utexas.edu

Education

2014-2019 Ph.D. in Physics, The University of Texas at Austin, Austin TX

2010-2014 B.S. in Physics, Nanjing University, Nanjing China

Experience

2015.09-2019.05	Research Assistant, Spintronics Group, UT Austin, Austin TX
2018.06-2018.08	Quantitative Research Summer Associate, J.P. Morgan Chief Investment Office, New York City, NY
2014.08-2015.12	Teaching Assistant, Department of Physics, UT Austin, Austin TX

Awards

2013	Meritorious Winner in Mathematical Contest in Modelling
2012	People's Award and Scholarship, second-level, Nanjing University
2011	People's Award and Scholarship, second-level, Nanjing University
2009	First Prize in Chinese Math Olympiad (Jiangsu Province, high school)
2009	First Prize in Chinese Physics Olympiad (Jiangsu Province, high school)